The scientific potential and technological challenges of the High-Luminosity Large Hadron Collider program

Oliver Brüning[1], Heather Gray[2], Katja Klein[3], Mike Lamont[1], Meenakshi Narain[4], Richard Polifka[5], Lucio Rossi[6]

[1] CERN, Geneva, Switzerland
[2] UC Berkeley/LBNL, CA, 94720, USA
[3] RWTH Aachen University, 52074 Aachen, Germany
[4] Brown University, Providence, RI, 02906, USA
[5] CTU in Prague, Faculty of Nuclear Sciences and Physical Engineering, Brehova 7, 115 19 Praha 1, Czech Republic
[6] Physics Department of the University of Milano and INFN-Sezione di Milano, Laboratorio LASA, viale fratelli Cervi 201, 20056 Segrate (MI), Italy

Abstract. We present an overview of the high-luminosity (HL-LHC) program at the Large Hadron Collider (LHC), its scientific potential and technological challenges for both the accelerator and detectors. The HL-LHC program is expected to start circa 2027 and aims to increase the integrated luminosity delivered by the LHC by an order of magnitude at the collision energy of 14 TeV. This requires upgrades to the injector system, accelerator complex and luminosity levelling. The two experiments, ATLAS and CMS, require substantial upgrades to most of their systems in order to cope with the increased interaction rate, and much higher radiation levels than at the current LHC. We present selected examples based on novel ideas and technologies for applications at a hadron collider. Both experiments will replace their tracking systems. We describe the ATLAS pixel detector upgrade featuring novel tilted modules, and the CMS Outer Tracker upgrade with a new module design enabling use of tracks in the Level-1 trigger system. CMS will also install state-of-the-art highly segmented calorimeter endcaps. Finally, we describe new picosecond precision timing detectors of both experiments. In addition, we discuss how the upgrades will enhance the physics performance of the experiments, and solve the computing challenges posed by the expected large data sets. The physics program of the HL-LHC is focused on precision measurements probing the limits of the Standard Model of particle physics and discovering new physics. We present a selection of studies that have been carried out to motivate the HL-LHC program. A central topic of exploration will be the characterization of the Higgs boson. The large HL-LHC data samples will extend the sensitivity of searches for new particles or new interactions whose existence has been hypothesized in order to explain shortcomings of the Standard Model. Finally, we comment on the nature of large scientific collaborations.

Keywords: High-Luminosity LHC, Upgrade, ATLAS, CMS, particle physics, Higgs boson, Physics beyond Standard Model

Submitted to: *Rep. Prog. Phys.*

1. Introduction

The world's largest and highest energy particle accelerator, the Large Hadron Collider (LHC) located at the European Organization for Nuclear Research (CERN), is exploring the fundamental building blocks of matter and their interactions through collisions between pairs of high energy protons. These high energy collisions recreate the energy densities achieved in the early universe just after the Big Bang. Dedicated runs with heavy ions instead of protons are used to provide new insights into the quark-gluon plasma.

The LHC [1] is located about 100 m underground and straddles the border between France and Switzerland close to the city of Geneva. Figure 1 shows the overall layout of the LHC and its relation to Geneva and the surrounding region. It has a nearly-circular shape with a circumference of 26.7 km. Four large detectors are installed at different positions along the ring, two of which are general purpose detectors, ATLAS [2](A Toroidal LHC Apparatus) and CMS [3](Compact Muon Solenoid), and two are more specialized ones – LHCb [4], focusing on extremely precise measurements of the quark flavor sector, and ALICE [5](A Large Ion Collider Experiment), which is optimized for heavy ion physics and investigations into the quark-gluon plasma.

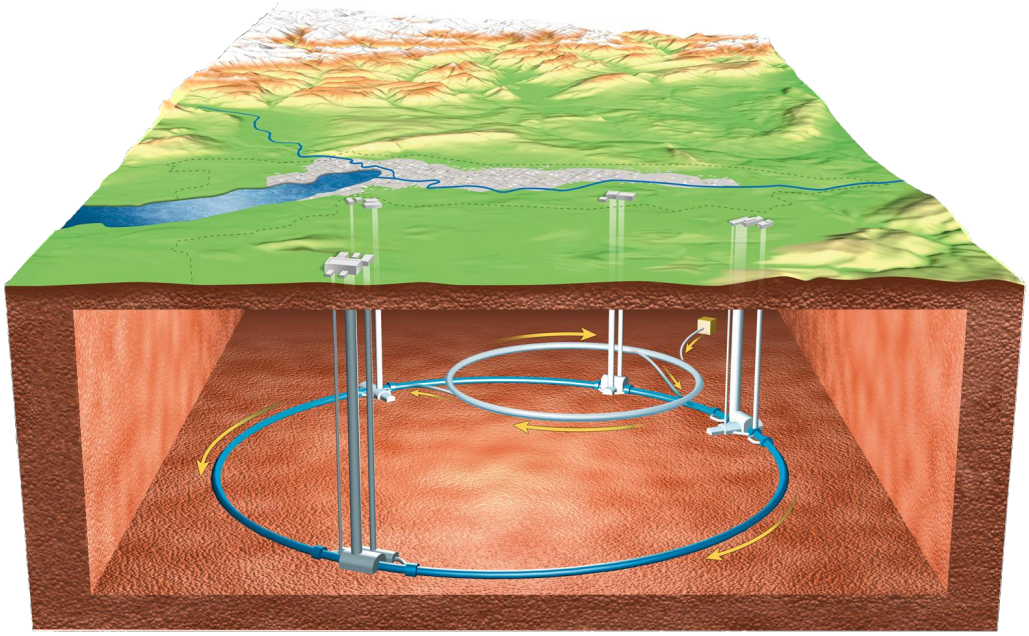

Figure 1. Schematic showing the overall layout of the LHC and its relation to the city of Geneva (grey) and the surrounding region. Also shown is the smaller Super Proton Synchrotron (SPS) accelerator, which sends beam to the LHC. Image credit – CERN.

The LHC was successfully commissioned in 2010 for collisions of protons at a center-of-mass energy of 7 TeV (1 TeV = 10^{12} eV = 0.16 μJ.). So far, two major data collection runs have taken place, Run 1 (2010–2013) and Run 2 (2015–2018). Between the LHC runs there are periods of typically a couple of years called Long Shutdowns (LS), devoted to maintenance and upgrade work of the accelerators and detectors. During Run 1 the center-of-mass energy increased from 7 to 8 TeV. Run 2 saw the LHC operating at 13 TeV, with a potential increase to the full design energy of 14 TeV foreseen for Run 3 (2022–2024).

Each counter-rotating proton beam consists of up to 2800 bunches (with nominally about 10^{11} protons per bunch) spaced around the LHC circumference. The beams circulate 11,245 times per second, with each beam travelling in a separate beam pipe for most of its journey around the ring. The high revolution frequency and large number of bunches result in approximately 40 million bunch crossings per second at the center of each experiment. This, combined with a high number of protons per bunch and small beam sizes at the interaction points, results in impressively high proton-proton collision rates. Typically, the two beams are kept circulating at full energy for between 10 and 20 hours, during which time proton-proton collisions are provided to the experiments at a gently diminishing rate. CERN's injector complex delivers the requisite high intensity bunches with exacting demands from the LHC on transverse beam size and longitudinal characteristics.

A key parameter of a collider is the luminosity – the number of collisions per unit area per second at a given interaction point; it is usually expressed in units of $\mathrm{cm}^{-2}\mathrm{s}^{-1}$. The luminosity at an interaction point is directly related to the collision rate seen by the experiment, and the luminosity tends to be used as a stand-in term for the collision rate. The integrated luminosity, in turn, is the total number of potential collisions per unit area for a given period of time, and when multiplied by the cross section yields the total number of collisions seen by a given experiment in that time. Cross sections encode the physics describing interactions between particles by expressing the probability for a particular interaction to occur. To avoid excessively large numbers, the LHC experimental community uses units of area appropriate for the sub-atomic domain, and the integrated luminosity is usually expressed in sub-multiples of an inverse barn (b) (1 barn = $10^{-28}\,\mathrm{m}^2$, such that $1\,\mathrm{fb}^{-1} = 10^{15}\,\mathrm{b}^{-1} = 10^{39}\,\mathrm{cm}^{-2}$.).

The LHC has exceeded its design specifications for the luminosity and for the total number of proton-proton collisions delivered in its first two runs. In Run 2, it regularly achieved an instantaneous luminosity of 2×10^{34} $\mathrm{cm}^{-2}\mathrm{s}^{-1}$, twice its design value. By the end of Run 2 an integrated luminosity of 190 fb^{-1} had been delivered to both ATLAS and CMS, about 50% more than expected and almost 20 times the combined integrated luminosity delivered by all the world's hadron accelerators prior to the LHC. The expected integrated luminosity at the end of Run 3 is expected to be of the order 350 fb^{-1}, increasing the probability of observing the rarest physics events.

Given the parameters of the LHC beams and the number of protons in each bunch, many more than one proton-proton interaction occurs during each bunch

crossing (see Section 2.1). This effect is called pileup. The ATLAS and CMS experiments received on average almost 20 collisions during each bunch crossing during Run 1. This number increased to over 30 during Run 2, with tails beyond 60. Complex analysis techniques are required to mitigate all unwanted effects of the pileup interactions.

The Standard Model (SM) of particle physics is a theoretical model that describes all known elementary particles [6–17]. It describes the electromagnetic, the weak, and the strong interactions in the same theoretical framework. The electromagnetic and the weak interactions appear as a single electroweak interaction at energies above a few hundred GeV. This so-called electroweak symmetry is broken at lower energies at which they appear as different forces with very different interaction strengths. The SM does not describe the gravitational interaction.

It took more than a century and numerous international collaborations to identify and discover all of the components of the SM. The most recent particle discoveries before the LHC were the W and Z bosons (1983 at the SPS [18–21]), the top quark (1995 at the Tevatron [22,23]) and the τ neutrino (2000 at the DONUT experiment [24]). The last missing piece was the Higgs boson – a neutral scalar boson which is the quantum of a field that is required to be able to describe massive particles in the SM. One of the main objectives of the LHC was to discover or to exclude the existence of the Higgs boson, with strong consequences for the SM, in which it plays a central role. Indeed, on July 4$^{\text{th}}$, 2012, the ATLAS and CMS Collaborations jointly announced the discovery of a new particle with a mass of 125 GeV [25, 26], which would become known as the Higgs boson. More details about the SM can be found in Sect. 5.1.

Although the SM provides an excellent description of most observed phenomena and has proven to be very robust in predicting experimental results, there are certain phenomena it does not explain. Currently, the SM does not contain any particles that are consistent with being the constituents of dark matter [27,28]. The existence of dark matter has been inferred by astronomical observations from its gravitational effects [28] but cannot be observed directly by telescopes looking for electromagnetic emissions because it does not emit light. Nor can the SM explain why our universe is built solely from matter although the Big Bang should have generated the same amount of matter and anti-matter.

Another important question is whether a unifying theory exists which provides a common description of all forces (strong, electromagnetic, weak, and gravitational). In such a theory, the SM would have to be incorporated together with all its incredibly precise tests which have been performed during the last sixty years. One theoretical challenge is known as the hierarchy problem which has its origin in the apparent weakness of the gravitational force relative to all other forces (by 17 orders of magnitude). As will be explained in Section 5, this motivates the existence of new physics around the TeV scale that is not contained in the SM, usually called BSM physics for "beyond the Standard Model". Discovering this new physics is a key objective of the LHC.

The High-Luminosity LHC (HL-LHC) will operate after the conclusion of

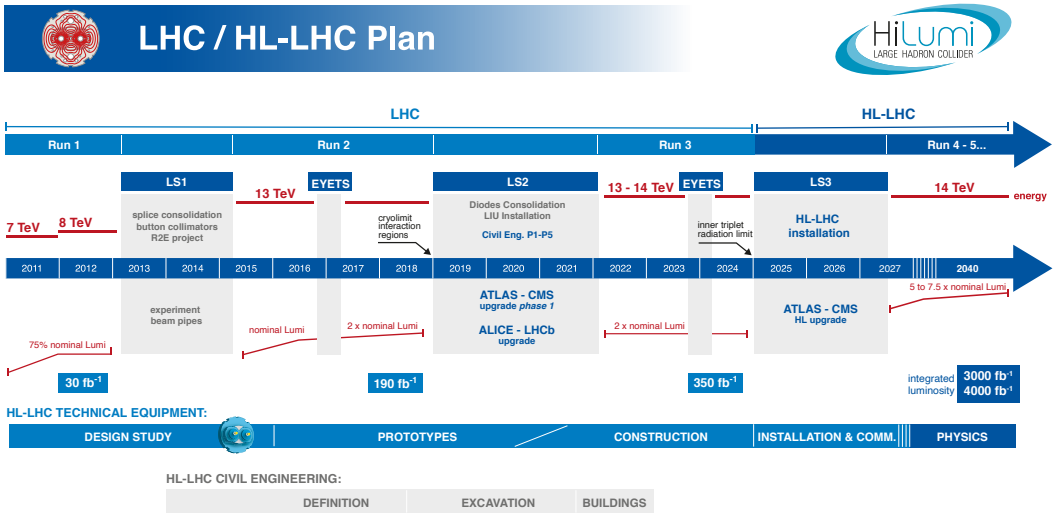

Figure 2. Timeline for the LHC and HL-LHC upgrades [29].

the current LHC program after Run 3 with the goal of increasing the integrated luminosity delivered to the experiments by an order of magnitude. Significant upgrades to the LHC itself and to the detectors will be installed. Data taking with the HL-LHC configuration is planned to start in 2027 and to continue until about 2040. The current LHC and HL-LHC timeline is presented in Figure 2.

The HL-LHC physics program will obtain a deeper understanding of the interactions and self-interactions of the Higgs boson, crucial for direct tests of the SM, and searches for dark matter and other BSM physics. Many of these processes have very low cross sections, so that data with a large integrated luminosity needs to be collected before conclusive statements can be made. Therefore, the upgrades that are underway for the HL-LHC focus on delivering ten times more integrated luminosity than the current LHC program. The projected lifetime of the HL-LHC is approximately 12 years with an expected integrated luminosity of $3000\,\mathrm{fb}^{-1}$. In order to achieve this, the instantaneous luminosity will need to be ten times larger, resulting in an average number of up to 140–200 interactions per bunch crossing.

This review will mainly focus on the upgrade of the LHC and the ATLAS and CMS detectors. The planned upgrade for the ALICE detector for the HL-LHC era will enable study of rare phenomena, perform high-precision measurements, and lead to unprecedented insight into the properties of the Quark-Gluon Plasma phase (QGP). The ALICE upgrade will enhance its tracking capabilities, the time projection chambers, and the forward muon tracker, to handle the higher collision rates. The collaboration plans to add a new fast interaction trigger detector to detect particles which scatter at a small angles, and also add a new forward high granularity calorimeter to improve particle identification. The LHCb detector upgrade will fully exploit the flavor-physics opportunities from their high production rate at the HL-LHC. It will also enable precision searches for physics beyond the Standard Model by

investigating processes which arise only in high orders in perturbation theory. LHCb plans to upgrade all the subdetector systems and add precision timing information, a new capability, which will help to resolve particles from different collisions in the same bunch crossing. In addition, the upgrade will have augmented ability to record data at much higher rates, providing the opportunities for a broad and competitive physics program. For more details on the ALICE and LHCb upgrades, see Refs. [30] and [31].

The main upgrades of the LHC machine will be discussed in Section 2. The overall concept of the detector upgrades, with special attention to significantly improved subsystems (tracker and additional detectors exploiting new technologies), is described in Section 3, while Section 4 summarizes the expected detector performance improvements. More details about the expected physics performance are given in Section 5. We conclude the review with an outline of the organizational structures of CERN and the experimental collaborations in Section 6.

2. HL-LHC Machine

2.1. Introduction to the LHC

The LHC was designed to use the existing 27 km tunnel that was built in the early 1980s to house the Large Electron Positron collider (LEP) [32] which operated from 1989 to 2000. The LHC's energy reach is essentially given by the maximum operational magnet field in the main dipole magnets and the size of the ring. This led naturally to the extensive use of high field superconducting magnets in the original design, and a lengthy R&D and prototyping phase eventually led to industrial production of the magnets with the final main dipole being delivered to CERN at the end of 2006.

The overall layout of the LHC is shown in Figure 3. The main dipole magnets are 15 m long and weigh 35 ton each and constitute the largest part of the LHC machine. The 1232 dipoles in the tunnel account for some 18.5 of the ring's 27 kilometers. An image of some of the dipoles as installed in the LHC tunnel is shown in Figure 4. The purpose of these magnets is to generate a magnetic field in excess of 8 T, which generates the centripetal force required to bend the trajectory of the particles circulating in the ring. The magnets are a two beam-pipe design, one for each of the two beams of circulating particles, and are cooled with superfluid helium provided by an industrial scale cryogenics system. When fully operational, the cryogenics system has around 88 t of superfluid helium at 1.9 K out of the total inventory of around 150 t.

The other substantial key elements of the LHC are the quadrupole magnets. These are four pole magnets that are designed to produce a magnetic field that increases linearly in magnitude when moving out from the center of the magnet where the field is nominally zero. Particles in the beam travelling off-axis through a quadrupole will therefore be deflected either towards (focusing) or away (defocusing) from the beam axis depending on the direction of the magnetic field that

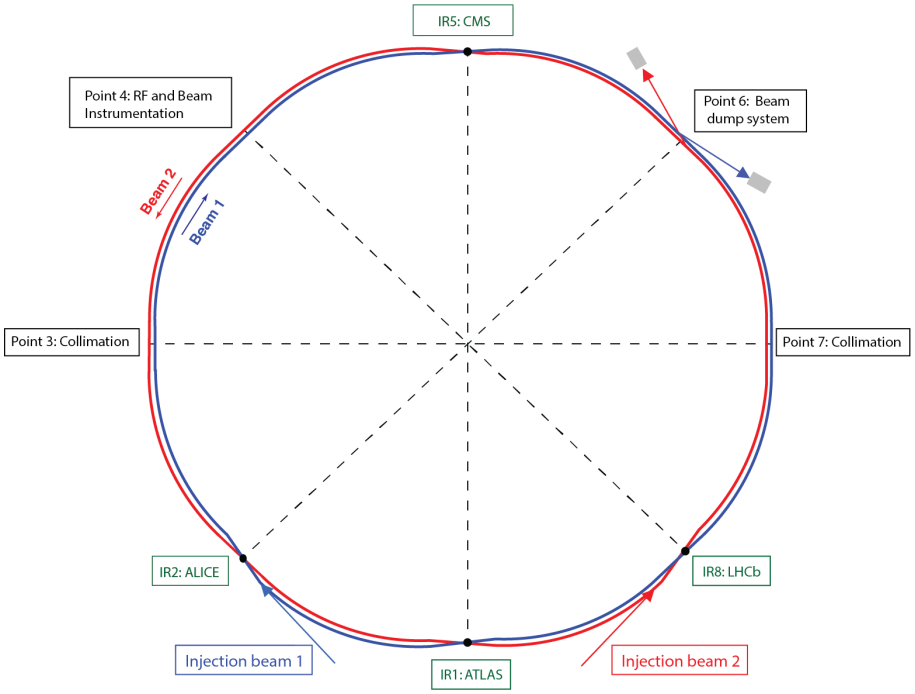

Figure 3. Overall layout of the LHC. The LHC has eight access points. Four house the LHC experiments, while the other four house the key accelerator hardware systems shown. The two countering rotating beams are shown in red and blue – for the majority of the ring the two beams are in separate beam pipes crossing each other in the four interactions regions (IR) shown [33].

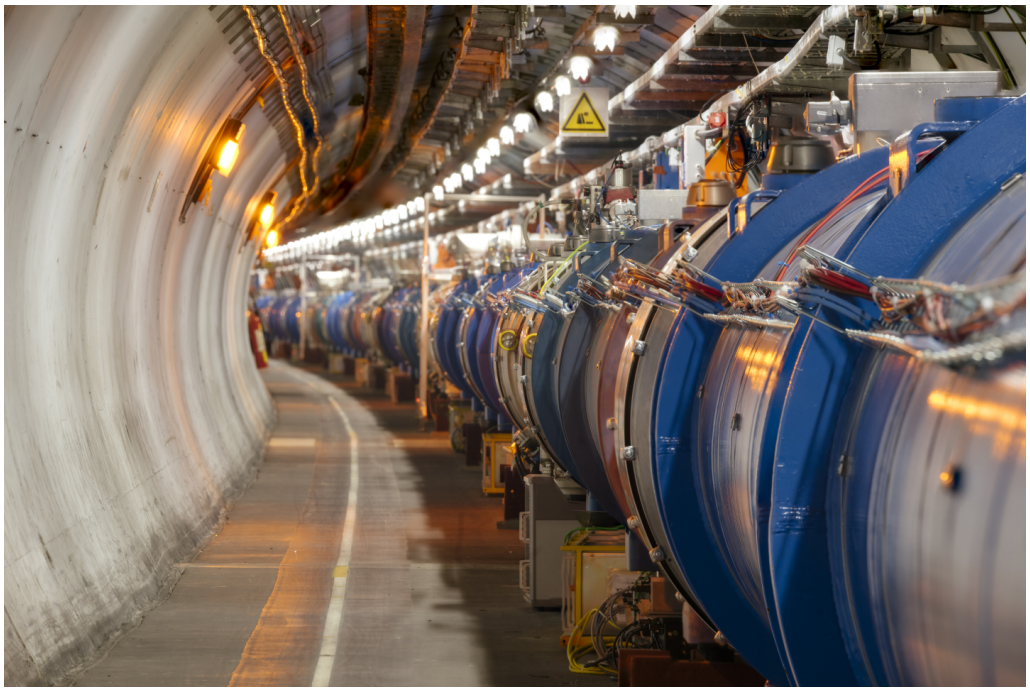

Figure 4. Image showing dipole magnets in the LHC tunnel. Image credit – CERN.

they encounter. The gradient of a quadrupole magnet describes the rate of change of magnitude of the magnetic field with the distance from the center; the higher

the gradient, the stronger the (de)focusing. The quadrupole magnets are installed to focus in the horizontal plane and de-focus in the vertical plane or vice versa. By alternating the polarity of the quadrupole magnets around the ring net overall stability is achieved; an arrangement known as alternating-gradient focusing.

There are four experiment insertions, the interaction regions (IRs) of Figure 3, spaced around the LHC ring. Each experiment is positioned in a 280 m long straight tunnel section (LSS). One of the key purposes of the LSS is to house the magnetic elements designed to ensure that the beams cross each other with very small beam sizes at the interaction points (IP) at the center of each experiment to maximize the luminosity. The beam size at a given IP is controlled by adjusting the focusing properties of quadrupole magnets installed in the associated LSS. Of particular note are the so-called inner triplets, a set of closely spaced, high gradient quadrupole magnets placed on each side of all of the four experiments (Fig. 5). These are key elements in providing transverse beams sizes of the order of 40 microns at each IP.

In addition to the inner triplet quadrupole magnets, the main dipoles, main quadrupoles, and the insertion region quadrupoles, there are hundreds of other magnets in the ring ranging through closed orbit dipole correctors, trim quadrupoles, sextupoles, octupoles, decapoles and even dodecapole corrector magnets. These magnets are used, for example, to correct the effects of magnet misalignments and higher order superconducting magnet field errors [34].

The overall focusing properties of the full ring are parameterized by what is known as the beta function. The beta function has a value at every point around the ring, and the beam size at a given point is directly related to the value of the beta function at that point. The value of the beta function at the IP, where the bunches pass through each other at the center of an experiment, is referred to as the beta star (β^*). Via the beam size, it is one of the key parameters that influence the collision rate seen by the experiments.

As introduced above, the LHC's performance can be characterized by its instantaneous luminosity – the number of potential collisions per unit area per

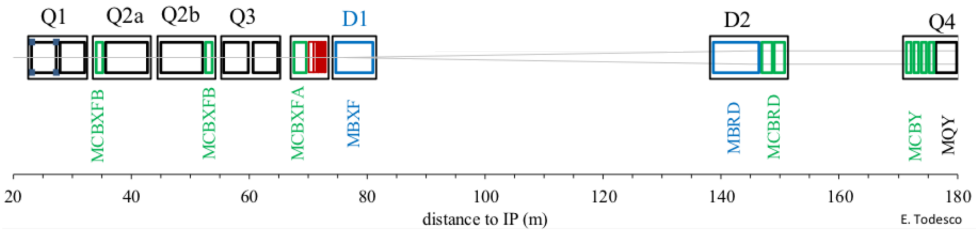

Figure 5. Schematic layout of the magnets immediately to the right of the ATLAS and CMS experiments in the HL-LHC. Q1, Q2a, Q2b, Q3 are the inner triplet quadrupole magnets. The beam axes are shown in grey. The D1, D2 separation/recombination dipoles bring the two beams together as they pass through the inner triplet and the experiment. The corrector magnets are indicated in green.

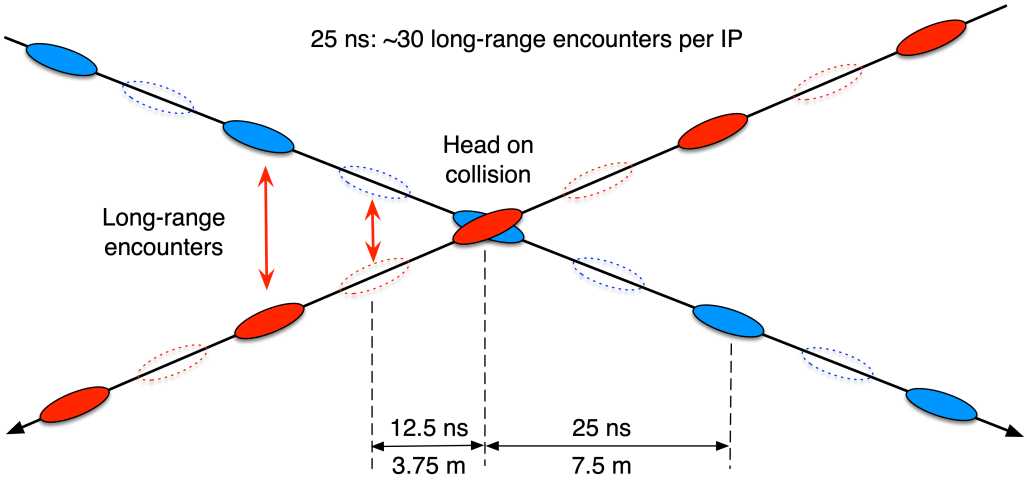

Figure 6. Schematic showing the effect of a crossing angle at an IP with bunches separated by 25 ns. The crossing angle serves to avoid unwanted collisions on either side of an IP. The bunches still see the electromagnetic effects of the bunches in the counter rotating beam as they pass each other at the so-called long-range encounters.

second at a given experiment's IP. The main parameters relevant for maximizing the luminosity are the number of bunches, the number of protons per bunch, and the transverse beam size at an IP. To avoid unwanted collisions on either side of an experiment, a crossing angle is introduced locally across each experiment (Fig. 6). This crossing angle has to be carefully adjusted to ensure that the bunches are well enough separated at the potential collision points on either side of the IP while respecting the available aperture of the magnets. The crossing angle can cause a significant reduction in the luminosity.

The minimum bunch spacing in the LHC is 25 ns (7.5 m) giving a maximum number of bunches of approximately 2800. Each bunch nominally contains approximately 1.2×10^{11} protons. The bunch population is constrained by a number of factors, e.g. the impact of one bunch on another as they pass through each other at the IP (the beam-beam effect); beam instabilities; and the robustness of protection devices. The transverse beam size at an IP can be optimized either by receiving smaller beams from the injectors or by varying the optics of the ring to reduce β^* and hence deliver smaller beam sizes at the IP.

Each beam circulating in one of the two LHC rings has a stored energy of up to 360 MJ when the LHC operates at 7 TeV beam energy with its nominal intensity. The local loss of only a very small fraction of this beam is sufficient to induce a quench in one of the superconducting magnets and the loss of the whole beam in an uncontrolled way could cause very serious damage to the equipment. The damage potential of the LHC beams makes the LHC beam dump system (LBDS) the most critical subsystem in the machine. There is, by design, tight coupling of the LBDS with the Beam Interlock System (BIS). The BIS takes inputs from a multitude of systems and will trigger a beam dump if any of those systems signal a problem by breaking the interlock loop.

A sophisticated collimation system is designed to stop high amplitude particles in the halo of the beam impacting the cold mass of the magnets. A collimator typically consists of two meter long jaws made of carbon fibre-reinforced carbon. The jaws are carefully manufactured to present a flat surface to the beam and are set up to an accuracy at the micron level. Over 100 individual collimators are set up at different distances from the beam. Closest to the beam are the so-called primary collimators, while the secondary and tertiary collimators are positioned further away from the beam. The cleaning process occurs over multiple turns of the beam. The protons that impact the primary collimators are scattered to larger amplitudes and impact the secondary collimators on subsequent turns. The showers produced in the secondary collimators are captured by tungsten based absorbers [35].

The collimation system also needs to withstand the potential impact of a beam dump misfire (an asynchronous beam dump). It therefore provides an important passive protection role by safely catching any beam misdirected by the beam dump system and preventing the impact of primary protons on the cold mass. Additional protection devices are positioned downstream of the beam dump system to fully protect against risks. There are also a series of protection devices at the injection regions to protect the downstream elements in case of injection kicker misfires.

An excellent vacuum in the cold part of the ring is required to avoid the loss of protons due to collisions with the nuclei of gas molecules. Maintaining good beam lifetime is very challenging in a cryogenic system where heat input into the 1.9 K helium circuit must be minimized and where significant quantities of gas can be condensed on the vacuum chamber. In cold sectors, a good vacuum is given by the absorption of gas molecules onto the cold surfaces for all gases except helium. To avoid subsequent desorption of the gas, low initial pressures are required before cool-down, and this is ensured, for example, by turbo molecular vacuum pumps. In the warm parts of the ring, non-evaporable getter (NEG) – sometimes described as molecular flypaper – on the inside of the beam pipes provides most of the pumping capacity, with additional ion pumps for the noble gases which are not absorbed by the NEG.

2.2. Key Objectives of the HL-LHC Upgrade

By 2018, the LHC was operating with an instantaneous luminosity twice that of the original design (2×10^{34} cm^{-2}s^{-1}). This excellent performance has come largely from the production of beams with small transverse size in the injectors and the reduction of β^* in ATLAS and CMS to well below the nominal value.

The HL-LHC plans to push the limits of the LHC even further and to deliver five times the nominal luminosity by improving a number of the factors outlined above. The design of the HL-LHC targets the following key points.

- A significantly lower β^* at the CMS and ATLAS IPs. This requires new wide aperture inner triplet magnets based on the novel use of niobium-tin (Nb_3Sn) superconductor.

- A significant upgrade to the injectors to increase the bunch population while maintaining low beam size.
- The high bunch population will require a large crossing angle. The loss of luminosity due to the crossing angle will be countered by the use of novel Crab radio frequency (RF) cavities.
- A number of measures to deal with the high level of collision debris and high radiation levels foreseen on either side of the high luminosity experiments.

The key deliverables of the HL-LHC upgrade project are:

- Increase the luminosity of the LHC to be able to deliver an integrated total luminosity of order 3000 fb^{-1}, and to allow for the potential accumulation of an integrated luminosity of up to 4000 fb^{-1} when using all engineering margins of the new HL-LHC configuration.
- To extend the LHC machine lifetime by another decade beyond the LHC Run 3 operation period.

The luminosity goals imply an annual integrated luminosity of 250 fb^{-1}. At the same time, the experiments have asked for the number of events per bunch crossing, the event pileup, to be limited to around 140. This event pileup corresponds to a peak luminosity of 5×10^{34} $\text{cm}^{-2}\text{s}^{-1}$. The annual integrated luminosity target and the limited peak luminosity require operation with leveled luminosity whereby the luminosity is deliberately limited to a certain value despite the potential to go to higher values. Ideally, this can be combined with the longest possible fill times in order to minimize the performance loss due to the time spent in recycling and refilling the machine.

The time spent operating with leveled luminosity is directly proportional to the total number of protons that can be stored in each beam [36], with the initial beam sizes coming from the injectors also playing an important role. Both these factors have been addressed through the LHC Injector Upgrade project (LIU) [37], which has executed a concerted program of improvements across the injector complex. As a result, the injector will be able to deliver almost twice the nominal bunch intensity with a very respectable beam size in the HL-LHC era.

The increased proton beam intensities require stored beam energies larger than 700 MJ per beam (over 1 A beam current at 7 TeV). This increased stored beam energy implies in turn an increased risk of damage for components in the LHC in some failure scenarios and during dips in the beam lifetime. These considerations require upgrades of the LHC collimation system and the absorber materials for machine protection devices, e.g. new robust collimator jaws, additional collimators in the cold sections at the end of the arcs through the use of new 11 T dipole magnets, and upgrades of the absorbers downstream of the interaction points.

Another key factor in maximizing the luminosity performance will be the reduction of the β^* values below 30 cm (the nominal value of the LHC is 55 cm). This requires a new approach for the machine optics and the corrections of chromatic aberration due to the large beta functions, and thus large beam sizes inside the

triplet quadrupole magnets. These aspects are addressed by the novel Achromatic-Telescopic-Squeezing (ATS) scheme [38] which uses not only the quadrupoles in the insertion regions for the β^* reduction, but extends the optics changes over the whole neighboring arcs, and hence allows for operation with β^* values well below 30 cm. The nominal HL-LHC parameters foresees β^* values of 15 cm, but values as low as 10 cm might be possible with the ATS scheme, given the achievable mechanical aperture of the triplets in the tunnel.

Extending the lifetime of the machine implies removing a considerable amount of active equipment from the LHC tunnel to reduce the effect of radiation on the electronics and the resulting disruption to machine operation due to single event effects in electronic components. Therefore new underground tunnel areas that are protected from beam induced radiation and allow access to the LHC equipment when the machine is operating have been constructed. The new underground installations require the implementation of a new powering scheme, which allows the equipment in the machine to be powered efficiently despite the power converters being located at a distance of 100 m from the LHC tunnel. The HL-LHC upgrade projects has tackled this challenge through the development of novel, high temperature, magnesium diboride superconducting cables that can be cooled via gaseous helium and can be implemented within a flexible cryostat.

2.3. The Key Technology Challenges of the HL-LHC

2.3.1. Triplet Magnet Technology Aiming for the accumulation of 3000 to 4000 fb^{-1} total integrated luminosity implies that the new triplet magnets of the HL-LHC upgrade must be an order of magnitude more radiation resistant than the currently installed triplet magnets. The higher radiation resistance of the new triplet magnet coils requires the introduction of additional absorber materials, e.g. tungsten blocks, between the LHC beams and the magnet coils. This design change implies an additional increase in the magnet coil aperture beyond what is necessary for the reduced β^* values of the HL-LHC parameters. Such large coil apertures are no longer possible with niobium-titanium (NbTi) magnet technology because the larger the aperture, the larger the magnetic field at the coils of the quadrupoles. NbTi is unable to sustain the required magnetic fields. The HL-LHC upgrade has, therefore, driven the development of new, high field niobium-tin (Nb_3Sn) magnets.

The new HL-LHC triplet magnets are based on a design with a coil aperture of 150 mm and a maximum gradient of 140 T/m (the peak field at the coil is near to 12 T) compared to the nominal LHC triplet magnets with a coil aperture of 70 mm and a peak gradient of 210 T/m (peak field at the coils of 8 T). The NbTi technology used for the LHC magnets reaches its performance limit at approximately 9 to 10 T. The Nb_3Sn technology allows an increase of the peak field at the conductor above 10 T and opens the door for magnetic fields up to 16 T. However, the development of the new Nb_3Sn technology is time consuming and has required 15 to 25 years of intensive magnet R&D to deliver the HL-LHC magnets. The first model magnets and prototypes have shown good results and the HL-LHC magnet program is on

track for producing the new HL-LHC magnets in time for the installation during Long Shutdown 3 (2025 to 2027).

The required lower gradient of the new triplet magnets, which is needed to keep the peak field at the coils below 12 T, implies, in turn, an increase to the triplet length because the triplet focusing strength is defined by the integrated gradient over the whole triplet assembly. Therefore, the HL-LHC triplets are approximately 30% longer when compared to the existing LHC triplets. However, the overall distance to the first active matching section quadrupole magnets, Q4 left and right of the IP, remains approximately unchanged thanks to the implementation of new, superconducting separation-recombination dipole magnets for the HL-LHC, which are considerably shorter than the present warm magnets that they replace. The separation-recombination dipoles (D1 and D2 in Figure 5) serve to bring the two beams together at the IP and then re-separate them. Figure 5 shows the new HL-LHC IR layout.

2.3.2. RF Technology As described above, the conventional approach for pushing the performance of a collider to higher luminosities is to reduce β^*. However, the LHC requires the operation with a large number of bunches per beam each spaced by a minimum of 25 ns (7.5 m). Therefore, the interaction region needs to be more than 200 m in length wherein the two counter-rotating LHC beams share the same vacuum chamber implies that there are up to 128 potential and unwanted collisions in the interaction regions. In order to avoid these bunch encounters, the LHC and the HL-LHC introduce orbit bumps across the IPs that keep the two beams separated at all these potential crossing points and produces a crossing angle at the IP (Fig. 6). The bunches need to be separated by a carefully controlled pre-specified distance so as to minimize the effects of the now long-range encounters. However, an unwanted consequence of the crossing angle is a reduction in the peak luminosity due to the imperfect overlap of the relatively long bunches induced at the IP.

While the luminosity reduction due to the crossing angle is only of the order of 10% for the nominal LHC design configuration, the luminosity reduction is between 70% and 60% for the HL-LHC β^* design values, which essentially negates a large part of the luminosity gain from the β^* reduction. The loss in luminosity due to the crossing angle can be recuperated through the use of so-called crab cavities, which are transversely deflecting RF devices that tilt the bunches during their passages along the crossing angle bump so that they more effectively overlap at the IP [39].

Figure 7 (left) shows the luminosity reduction factor as a function of β^* for a constant, normalized separation of the long-range beam-beam encounters by $10\,\sigma$. Figure 7 (right) illustrates the crab cavity mechanism schematically. The crab cavities effectively eliminate the luminosity reduction due to the crossing angle. However, the crab cavities have never been installed in a hadron storage ring before and the use of crab cavities in the HL-LHC has raised concerns about potential beam degradation due to noise from the cavities and equipment damage due to fast failure modes of the cavities. The adaptation of crab cavities for the HL-LHC upgrade was therefore coupled to an intensive R&D effort that aimed at testing crab cavity

prototypes in the SPS prior to their use in the LHC.

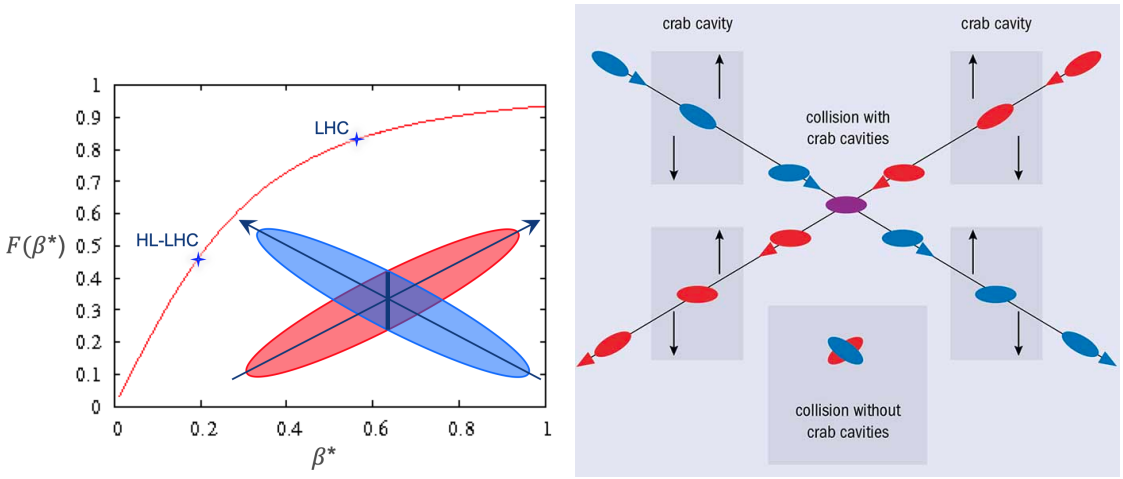

Figure 7. Left: the luminosity reduction factor F as a function of β^* assuming a typical separation of the bunches at the long-range encounters. Right: in the current configuration of the LHC, the counter-propagating (red and blue) proton bunches meet with a crossing angle (bottom). To cope with the larger crossing angles at the HL-LHC, crab cavities will administer a transverse RF kick that tilts the bunches causing a higher degree of overlap (purple) at the collision point. Image credit: CERN.

2.3.3. Superconducting Links for Powering In the LHC the electric current is transported from the power converters to the superconducting magnets in the tunnel with the help of normal conducting, water cooled cables. With the move to the newly constructed underground galleries, the power converters will be up to 100 m away from the magnets and this approach would generate too much resistive heat for efficient current transport. The HL-LHC upgrade project tackles this problem through the development of novel, high temperature, magnesium diboride (MgB_2) superconducting cables that can be cooled via gaseous helium and can thus be implemented within a flexible cryostat [40]. Figure 8 shows the cross section of the novel MgB_2 cable and a prototype of the superconducting link.

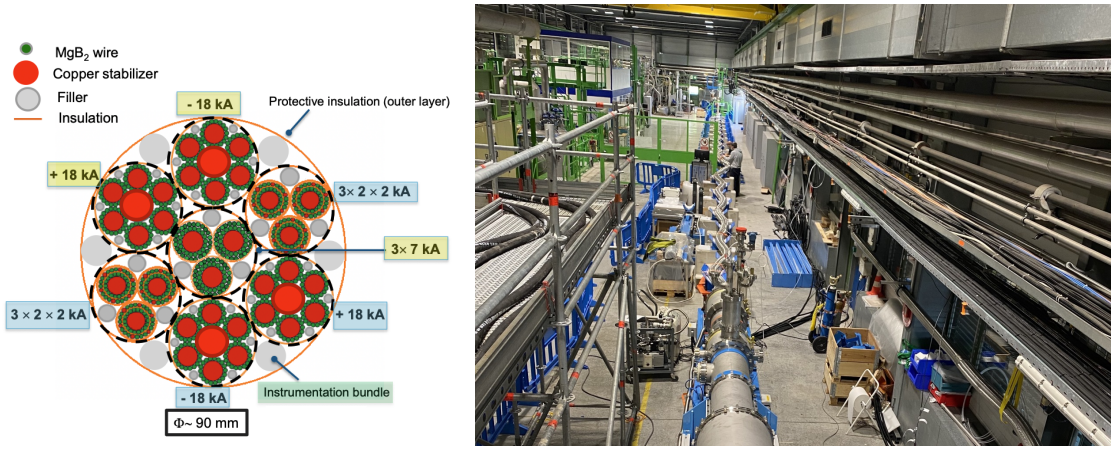

Figure 8. Left: cross-section of the MgB_2 superconducting cable. Right: prototype for the flexible cryostat for the superconducting link. Image credit: Amalia Ballarino.

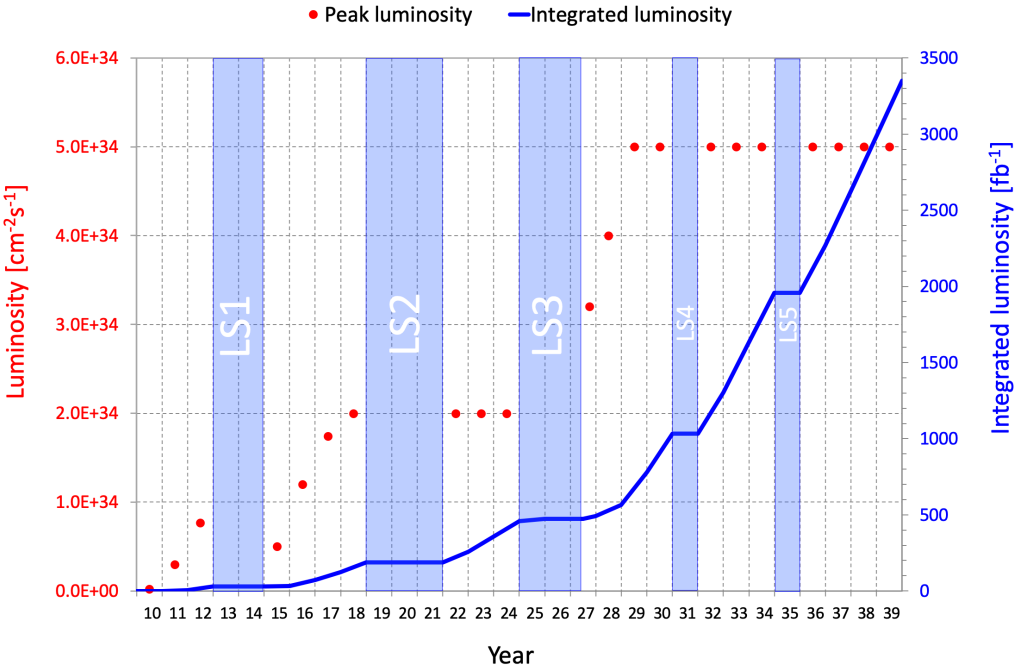

Figure 9. Foreseen nominal performance evolution of the HL-LHC. In red is the instantaneous luminosity performance showing a staged approach to the leveled luminosity of 5×10^{34} cm^{-2}s^{-1}. In blue is the total integrated luminosity over the lifetime of the LHC assuming already achieved machine availability. Given these assumptions, the target total of 3000 fb^{-1} will be achieved in 2038.

2.4. Projected Schedule and Performance

The entire LIU project and parts of the HL-LHC upgrade (e.g. collimators) has been installed during LS2 (2019–2021). However, the bulk of the HL-LHC upgrade will take place during Long Shutdown 3 (2025–2027). The need for regular maintenance of the major LHC infrastructure (e.g the cryogenic plants) requires a regular extended ($\approx$1 year) shutdown of the machine every 3 to 4 years. Following

the completion of the HL-LHC installation in 2027, it is assumed that the Operations team will be able to bring the machine to its nominal performance level by the end of 2028, closely followed by two full years of operation with near nominal design performance before entering Long Shutdown 4 (LS4). Figure 9 summarizes the foreseen evolution of the HL-LHC performance [41].

3. Detector Upgrades for HL-LHC

Four large particle detectors, named ALICE, ATLAS, CMS, and LHCb, are installed at the LHC. Their purpose is to identify the particles emerging from the collisions, and to measure as precisely as possible those particles' properties, in order to perform physics measurements and to discover new physics. In this paper we will focus on the two multi-purpose detectors, ATLAS and CMS (Fig. 10), which are – in contrast to LHCb and ALICE – not optimized for specific physics channels or topics. We provide a short summary of the status of the present detectors (Sect. 3.1), and will then turn to the Phase-2 upgrades of the ATLAS and CMS experiments (Sect. 3.2). After a short overview, several examples will be presented in more depth: the tracker upgrades (Sect. 3.3), the CMS endcap calorimeter upgrade (Sect. 3.4), and the new timing detectors (Sect. 3.5).

ATLAS and CMS use a right-handed coordinate system, with the origin at the nominal interaction point, the x-axis pointing to the centre of the LHC ring, the y-axis pointing up, and the z-axis along the anticlockwise-beam direction. Cylindrical coordinates (r, ϕ) are used in the transverse plane, ϕ being the azimuthal angle around the z-axis. The polar angle θ is measured from the positive z-axis. The pseudorapidity η is defined as $-\ln[\tan(\theta/2)]$.

3.1. Present status of the ATLAS and CMS detectors

The ATLAS [2] and CMS [3] detectors consist of many different detector systems, called subdetectors, with millions of individual channels in total. Each channel performs an independent measurement of a certain quantity. The subdetectors are arranged in concentric layers around the beam pipe. Most subdetectors have a central part (referred to as barrel), and disk-like structures (named endcaps) at both ends of the detector, as can be seen in Fig. 10. Each subdetector consists of the sensitive detection elements, which measure physics observables such as energy, transverse momentum (The transverse momentum is the component of the momentum vector perpendicular to the direction of the beam of protons. Many signatures of new physics are characterized by particles with large transverse momenta.), or the trajectories of the particles created in the collisions, plus the electronics required to read out the information collected by the detector, mechanical support structures to maintain the positions of the detector elements, and services. Services include the distribution of electrical power to the detector and the data links that configure the detector and ship the data out to the off-detector electronics (referred to as back-end), where they are processed further, as well as cooling and

gas supply lines for some of the subdetectors. One of the challenges is that the detectors, in particular the inner parts, are difficult to access once built, since reaching a certain component would require the deinstallation of other components, which is not feasible on a reasonable time scale due to the complexity of the detector, and bears the risk of damaging functional parts. This is similar in many ways to designing a detector that would need to operate in space.

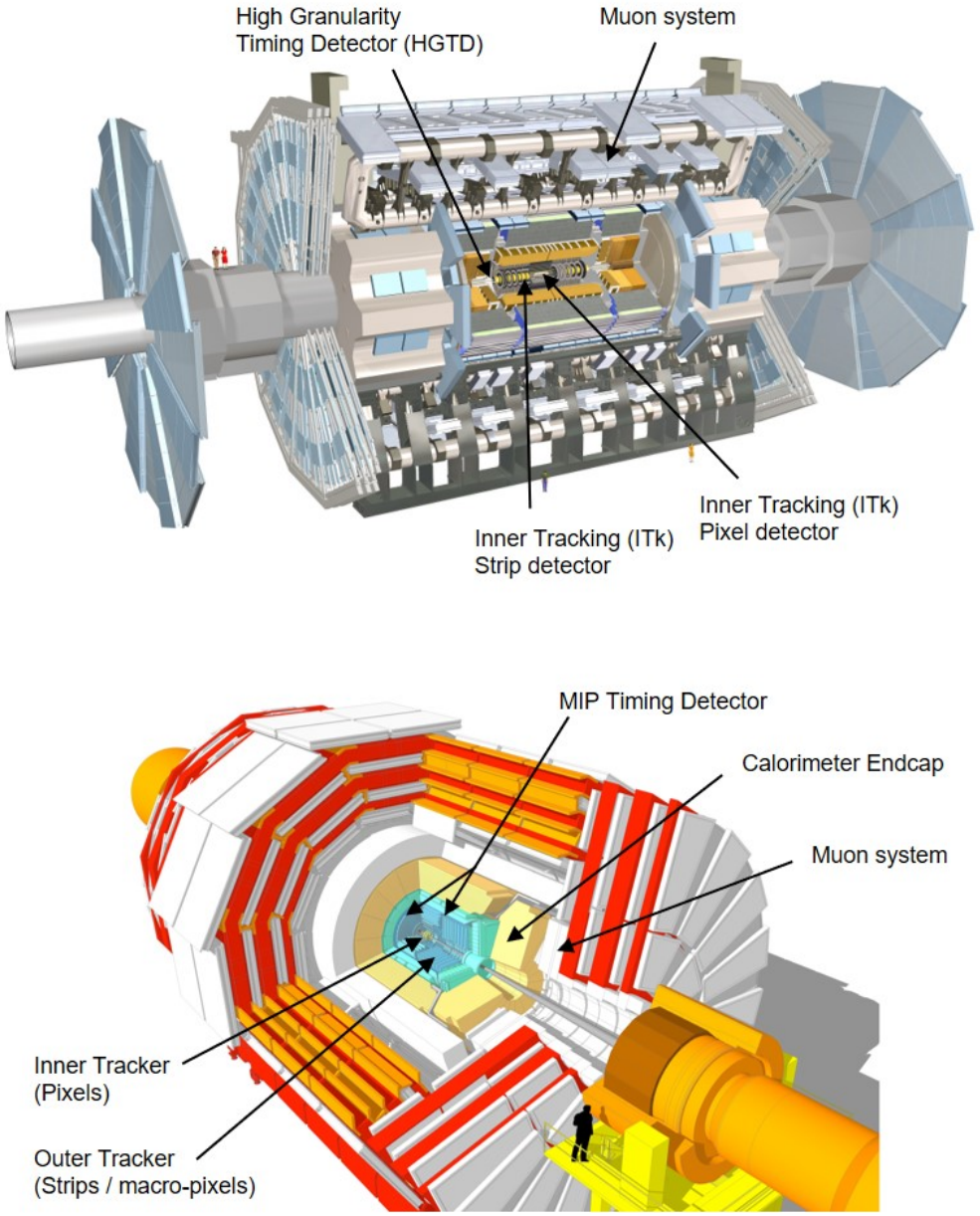

Figure 10. The major planned upgrades to the ATLAS (top) and CMS (bottom) detectors for the HL-LHC. The location where each upgrade will be installed is illustrated on sketches of the current detectors [42, 43]. The two detectors are not drawn to the same scale.

The ATLAS and CMS detectors are huge devices, with sizes comparable to buildings: the ATLAS detector is 44 m long and 25 m high, while the CMS detector is about 29 m long and has a diameter of 15 m. Also their weights are impressive, with

masses of 7,000 t for ATLAS and 14,000 t for CMS (as a comparison, the Eiffel tower in Paris has a mass of "only" 10,000 t). The differences in size and mass stem mostly from the different designs of the magnet systems. CMS features a superconducting solenoid that delivers a magnetic field of 3.8 T, and a heavy iron return yoke. The ATLAS magnet system consists of a smaller central superconducting solenoid with a 2 T field, and air-core toroidal coils further outside. These differences are also reflected in the names of the detectors: ATLAS stands for "A Toroidal LHC ApparatuS", and CMS for "Compact Muon Solenoid".

While the ATLAS and CMS detectors differ in many details, the basic composition is similar, and consists, when moving from the center outwards, of the following components. The tracking detectors, located closest to the interaction point, measure the trajectories of charged particles with high precision. These tracking detectors contain pixel- and strip-like electrodes, producing 3D and 2D spatial measurements, respectively. In addition, the tracking detectors allow the determination of the transverse momenta of those particles, which are deflected due to the Lorentz force in the magnetic field created by the magnets, and the reconstruction of the points where the particles were produced. Electromagnetic and hadronic calorimeters are located further outside.

Calorimeters absorb most of the particles that impinge on them and are used to measure their energies. The locations of the energy deposits by neutral particles, which do not leave tracks in the tracking detector, serve to measure the direction in which these particles emanate from the interaction region. Electromagnetic calorimeters are designed to measure the energy of electrons, positrons and photons, which lose their energy dominantly via bremsstrahlung (when photons are radiated off electrons or positrons) and pair production (when photons convert into an electron-positron pair).

Hadronic calorimeters are designed to measure the energy of hadrons, which penetrate much deeper into material and often traverse the electromagnetic calorimeter without leaving a detectable signal.

The hadronic calorimeter is located outside the electromagnetic calorimeter to intercept all particles that penetrate through the electromagnetic calorimeter and it is much deeper in terms of nuclear interaction lengths than the electromagnetic calorimeter in order to absorb all the energy deposited by hadrons. Finally, the muon chamber tracking systems in the outermost detector layer identify muons, which traverse all other detector systems basically undisturbed, and measure their trajectories and transverse momenta.

Both the ATLAS and CMS experiments feature complex selection or “trigger” systems, which select the most interesting events. ATLAS and CMS cannot record all the collisions that are taking place. With bunches of about 10^{11} protons colliding every 25 ns, and each individual bunch crossing consisting currently of about 40 individual proton-proton collisions on average (and up to 200 at the HL-LHC), the amount of data that would have to be sent out of the detector exceeds the bandwidth that can realistically be provided by electrical or optical data links, used to transfer the detector information to the back-end data processing system. In addition the

amount of data to be stored would be outrageous, with of the order of 40 terabytes of data to be stored per second, as the typical event size is of the order of 1 MB. On the other hand, not all collisions are interesting for science and need to be recorded. The cross sections, which quantify the rates at which the physics processes take place, differ by many orders of magnitude between the various processes. For example, the cross section of Higgs production, which is of great interest, is about seven orders of magnitude lower than that of the production of pairs of bottom quarks. The experiments have thus implemented trigger systems, which provide a quick decision whether an event is interesting or not, based on coarse detector information which can be read out quickly. The full event information, from all subdetectors and with full granularity, i.e. not grouped into more coarse entities, is only read out for events selected by the trigger. Since the full event data must be stored in buffers in the readout chips in the detector until this decision is made, with a new event arriving every 25 ns, the available time for a trigger decision, often referred to as trigger latency, is very short, on the order of a few microseconds.

In practice, the trigger "menu" consists of hundreds of different trigger categories that are designed for different physics channels, ranging from very simple (e.g. a calorimeter deposit with an energy above a certain threshold present in the event) to involved (e.g. requiring the presence of several muons and jets, all with certain minimal transverse momenta and within specified distances to each other).

The designs of the original ATLAS and CMS detectors started in the 1990s [44, 45] and the first collision data were recorded in 2009. The detectors were designed for the nominal LHC performance parameters, in particular an instantaneous luminosity of $1 \times 10^{34}\,\mathrm{cm}^{-2}\mathrm{s}^{-1}$, a pileup of about 30, and an integrated luminosity of about $500\,\mathrm{fb}^{-1}$. Both detectors have taken data very successfully and with high efficiency during Run 1 and Run 2.

From 2016 onwards, the LHC exceeded the design instantaneous luminosity, with peak luminosities of about $1.5\times10^{34}\,\mathrm{cm}^{-2}\mathrm{s}^{-1}$, and even up to $2.1\times10^{34}\,\mathrm{cm}^{-2}\mathrm{s}^{-1}$ in 2018, and the detectors have operated successfully well beyond their design specifications. Nevertheless, to cope with this challenge, parts of the detectors have already been upgraded, or are being upgraded during Long Shutdown 2 (2019-2021). These upgrades are referred to as Phase-1 upgrades, and we will mention them only briefly and for completeness, because the focus of this article is on the Phase-2 upgrades for the HL-LHC. Important Phase-1 upgrades have been performed on both pixel detectors, with an additional inner layer installed in ATLAS [46] and a completely new pixel detector installed in CMS [47]. In the CMS hadronic calorimeter the detection elements have been exchanged [48], while an upgrade to the muon detector is being installed in ATLAS [49] as part of the ATLAS Phase-1 upgrade.

3.2. Overview of Planned Phase-2 Detector Upgrades

The HL-LHC will bring the detectors into a new realm of operation in terms of instantaneous and integrated luminosity.

The performance improvements imply a larger number of particles incident on each detector component (hit rate), a larger number of simultaneous interactions happening at each collision (about 140-200), and higher integrated radiation levels, which rise linearly with integrated luminosity. To fully profit from the HL-LHC performance improvements the detectors must undergo significant upgrades, mainly related to three reasons:

(i) degradation of the sensing elements and electronics due to accumulated radiation;

(ii) performance limitations of the currently installed electronics at the expected high hit, data and trigger rates;

(iii) performance degradation due to the high number of pileup events, which leads for example to high track densities, i.e. number of tracks per unit area.

The radiation levels depend strongly on the location in the detector volume, in particular on the radial distance from the beam pipe. This can be seen in Fig. 11, which shows the simulated fluence map of the ATLAS detector. Fluence quantifies the radiation level in terms of the number of particles per unit area. Given that radiation effects depend on the material, particle type and particle energy, the fluence is given in terms of 1-MeV neutron equivalent in silicon (Si), i.e. normalized to the effect of neutrons with an energy of 1 MeV in silicon, and this unit is often named $n_{\mathrm{eq}}/\mathrm{cm}^2$. In the forward and backward regions, i.e. in regions with a small angular distance to the beam pipe on either side of the detector (While "forward" and "backward" refer to the positive z and negative z sides of the detector, respectively, the term "forward" is often used for both sides when no distinction is needed.), the radiation levels are high. While the fluence is typically the relevant quantity for sensing elements such as silicon sensors, for the electronics the relevant quantity is instead the total ionizing dose (TID). Dose maps can be found e.g. in Ref. [50]. Radiation effects include displacement of atoms (displacement damage), and ionization damage, where charge carriers are liberated. Both effects are relevant for particle detectors.

Both ATLAS and CMS are keeping those parts of the detector that will continue to function well under HL-LHC conditions, e.g. the magnets, but need to exchange or upgrade a number of systems. New subdetectors are also planned, which improve the physics capabilities under high pileup conditions. The new detector parts will mostly be installed in Long Shutdown 3 (2025-2027), with some subdetector upgrades starting already earlier (e.g. during LS2). The construction and integration of the new detector parts will take several years. Figure 10 summarizes the planned upgrades to each detector.

In the following we will provide a short overview of the Phase-2 upgrades, while selected examples will follow in Sections 3.3 to 3.5.

Trigger systems Both experiments have two-stage trigger systems [52–54]. The first trigger level, or L1, consists of custom electronics that presently receives information from the muon and calorimeter systems. The maximum L1 trigger

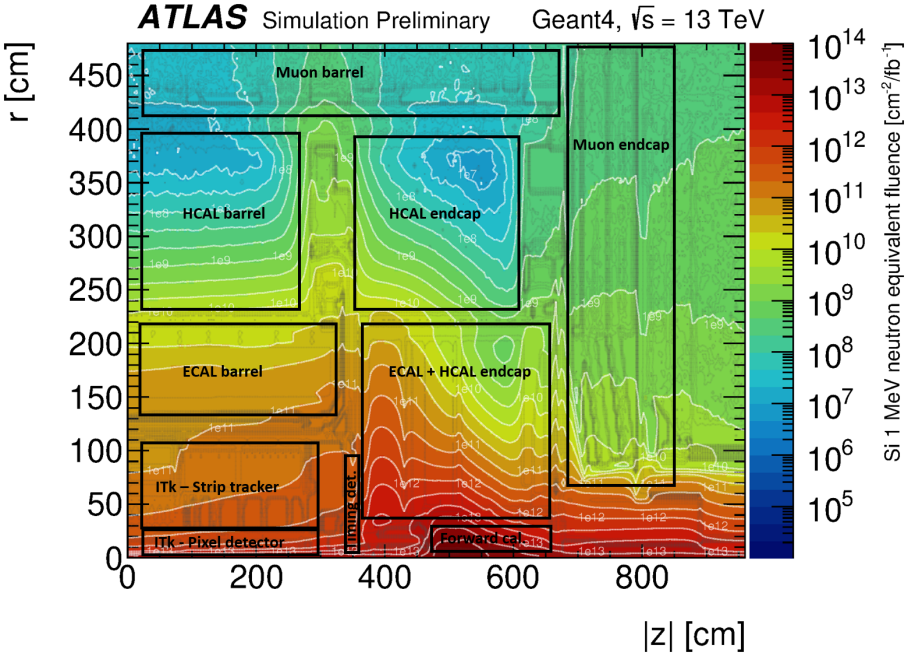

Figure 11. Expected fluence levels per received fb^{-1} of integrated luminosity in the ATLAS detector as simulated by the Geant4 program [51] as a function of the distance along the beam direction, z, and the radius, r [50]. The interaction point is at the left lower corner. The rough positions of the various subdetectors are indicated by the black frames, and the subdetectors are labeled.

frequency, corresponding to the frequency at which the full detector information is read out to the back-end, is presently at a rate of 100 kHz for both experiments, and the decision is made and propagated to the front-end within 2.5 μs (ATLAS) and 4 μs (CMS). This time delay is known as the latency. The second stage is called High Level Trigger (HLT) and consists of computer farms. At this stage the full event information is available and complex algorithms can be run. The output rate of events to be stored for offline analysis is presently limited to 1 kHz for both experiments. In the Phase-2 upgrade the maximum trigger frequencies will be increased to 750 kHz (1 MHz) and 7.5 kHz (10 kHz) for L1 and the HLT, respectively, for CMS (ATLAS), while the latency will be increased to 12.5 μs (10 μs). These changes pose considerable challenges for those subdetectors that are not exchanged, and which have been designed based on the original specifications. Many subdetector upgrades are driven by changes in the trigger system.

Tracking The innermost component of the detectors are the trackers, comprising a pixel detector, installed closest to the beam pipe, and a strip tracker surrounding it. The current tracking detectors are based on silicon sensor technology, while ATLAS, in addition, has a gas-filled tracking and transition radiation detector around the silicon tracker. Both ATLAS and CMS will completely exchange their tracking systems to increase the acceptance in the forward region and to improve radiation hardness, granularity (i.e. the size of a single detection element), readout speed and bandwidth (i.e. the amount of data that can be read out per second to the

back-end) [55–57]. The new trackers will be based on silicon technology, which has proven to work very well during Runs 1 and 2. Details will be presented in Sect. 3.3.

Calorimetry The calorimeters are located outside the tracking detectors. There are two basic types of calorimeters, homogeneous calorimeters and sampling calorimeters. Homogeneous calorimeters consist of a single active material which measures the entire energy deposited by a particle in its volume. Sampling calorimeters consist of a passive absorber material in which the particle interacts and creates a shower of secondary particles. The energy deposited in this absorber is not measured. Layers of the absorber material are interspersed with layers of active material which measure the energy deposited by the charged secondary particles that traverse the active layer. Every charged particle deposits the same typical amount of energy so that the energy in all active layers is proportional to the number of secondaries created in the shower which in turn is proportional to the energy of the primary particle that is to be measured. Homogeneous electromagnetic calorimeters typically have superior energy resolution but sampling calorimeters are more cost effective, especially when the calorimeter is large and moderate resolution is sufficient.

In CMS, the homogeneous electromagnetic calorimeter (ECAL) sits directly outside the tracker. It uses lead-tungstate crystals, in which scintillation light is produced and measured with avalanche photo diodes in the barrel region, and vacuum photo triodes in the endcaps. The ECAL is surrounded by the hadronic sampling calorimeter (HCAL). The HCAL consists of brass absorber plates interspersed with active plastic scintillator tiles, which were originally read out by hybrid photodiodes. These have been replaced with silicon photomultipliers as part of the Phase-1 upgrade [48]. The crystals and plastic scintillators suffer from irradiation, leading to light loss, and this effect is much more pronounced in the forward region due to the high radiation levels in that region. For the barrel ECAL, the 61,200 crystals along with their avalanche photo diodes will continue to function well throughout HL-LHC operation. The detector will be operated at a lower temperature, to reduce noise, and the electronics will be upgraded to be compatible with the new trigger (bandwidth and latency) requirements, and to allow the usage of information from single crystals in the L1 trigger. Presently, groups of 5×5 crystals are read out together [58]. No significant upgrade is planned for the barrel HCAL. In the endcaps, however, a completely new and innovative device will be used, which combines the functions of the ECAL and HCAL, using silicon sensors and scintillators as active calorimeter materials [59]. This will be covered in Sect. 3.4.

The ATLAS calorimeter system [60] uses liquid argon technology for the electromagnetic calorimeter, the endcaps of the hadronic calorimeter, and the forward calorimeters. Absorber plates made from lead, copper or tungsten are interspersed with gaps filled with liquid argon as active material, where the ionization is measured. The HCAL barrel calorimeter instead is constructed of steel absorber plates and plastic scintillator tiles as the active material. The ATLAS

calorimeter is, in general, expected to maintain its performance under HL-LHC conditions, so no significant detector upgrades are foreseen, but new electronics need to be installed for compatibility with the expected higher particle and trigger rates [61].

Muon systems The muon systems consist of many gas-filled chambers, installed as the outermost detector layer, because muons lose very little energy when they travel through the detector. The muon systems aim to identify the muons and to measure their transverse momenta. A variety of muon detector technologies are used in both ATLAS and CMS, and it is beyond the scope of this article to explain the working principles of all these detector types.

The original muon system of CMS consists of roughly 1800 muon chambers using three different technologies: drift tubes in the barrel, cathode strip chambers in the endcaps, and resistive plate chambers in both regions. Tests have shown that the chambers can cope with the higher expected particle rates and replacements are not needed. The electronics will be upgraded, though, to be compatible with the higher trigger frequency and longer latency [62]. The muon system will be enhanced with additional chambers in the forward region, to increase acceptance (i.e. the geometrical coverage, so basically the detector volume in which muons can be identified) and to add redundancy, and to improve the trigger and reconstruction performance. This includes the addition of new types of chambers based on the gas electron multiplier (GEM) technique in the first two layers [63], and the addition of improved resistive plate chambers in the last two layers. The station named GE1/1, comprising 144 GEM chambers in the pseudorapidity, η, range of 1.6-2.15, has already been installed during Long Shutdown 2.

The original ATLAS muon spectrometer comprises about 4000 chambers in four different technologies: monitored drift tubes in the barrel and cathode strip chambers in the endcaps, assisted (in particular for triggering) by thin gap chambers and resistive plate chambers in the barrel and endcaps, respectively. The innermost endcap layer, named "Small Wheel", is being replaced as part of the ATLAS Phase-1 upgrade during the Long Shutdown 2 with the New Small Wheel [49], featuring small strip thin gap chambers and chambers based on a micro-mesh gaseous structure (so-called MicroMegas). The Phase-2 upgrade will include new readout and trigger electronics for the existing chambers. The system will be enhanced with additional, improved chambers both in the barrel and endcap regions, to improve the trigger performance as well as the acceptance, and to increase redundancy and longevity [64]. In particular, additional resistive plate chambers will be installed in the inner barrel layer.

Timing detectors Both ATLAS and CMS plan to install completely new subdetectors for the HL-LHC, referred to as timing detectors [65, 66], which will measure the arrival times of individual particles from the collisions with an unprecedented precision of 30-50 ps per track. This will enhance the experiments' capability to distinguish particles from different collisions, by adding the timing

information to the spatial information that is used now. Given that up to 200 simultaneous collisions are expected to occur in one bunch crossing at the HL-LHC, to distinguish between them is considered one of the biggest future challenges. These timing detectors will be described in Sect. 3.5.

3.3. Tracking Detectors

Tracking detectors measure the paths ("tracks") of charged particles through the detector by detecting the intersection points ("hits") of the trajectories in many detector layers, with high spatial precision. This allows the particles' transverse momenta to be reconstructed, by exploiting the momentum-dependent bending of the tracks in the magnetic field, and to identify where the particles were produced. The production points are called vertices, and the primary vertex, where the proton-proton collision occurred, is distinguished from the secondary vertices, created by the decays of long-lived particles, such as hadrons that contain b or c quarks, into other particles inside the detector. One challenge at the HL-LHC is the large number of primary vertices per event due to pileup, with an expected mean vertex density (also known as "pileup density") of 1.4 vertices per millimeter along the beam axis [65], of which the one belonging to the interaction of interest must be identified.

The tracking detectors of ATLAS and CMS will deploy solid-state sensor planes, made from silicon. A plane or "sensor" typically has an area between 10 and 100 cm^2 and consists of thousands or even hundreds of thousands of individual sensing elements, depending on if these are strips or pixels. Pixels have dimensions of a few tens of microns in both directions, while strips have a similar width but are typically several centimeters in length. Pixel detectors are specifically designed to provide three-dimensional measurement points instead of the two-dimensional measurement points provided by the silicon strip detectors. Pixel detectors provide very precise spatial measurements, with a typical precision of a few microns, which is important for vertex reconstruction. Each individual sensing element, i.e. a pixel or a strip, represents a pn-diode which is reverse-biased by applying a voltage, referred to as "bias voltage" or "high voltage" [67]. This creates a layer that is depleted from free charge carriers, covering the full sensor thickness of typically 150-300 μm. When charged particles from the collisions traverse the depleted volume they create electron-hole pairs, and these charge carriers drift to the respective electrodes, where they induce a signal. Readout ASICs (Application Specific Integrated Circuits) then process these signals.

The general concept and the challenges for tracking detectors are illustrated in Fig. 12, which shows a simulated top quark pair production event in the Phase-2 ATLAS tracker. A pileup of 200 interactions per bunch crossing was included in this simulation. The particles leave hits in the (grey) sensing elements, and hundreds of tracks are reconstructed. These tracks can originate either from primary or secondary vertices. A zoom onto the interaction region is shown in the inset figure, with many primary vertices along the beam line. Almost all are pileup interactions, and the challenge is to identify the one that corresponds to the hard scattering (cyan

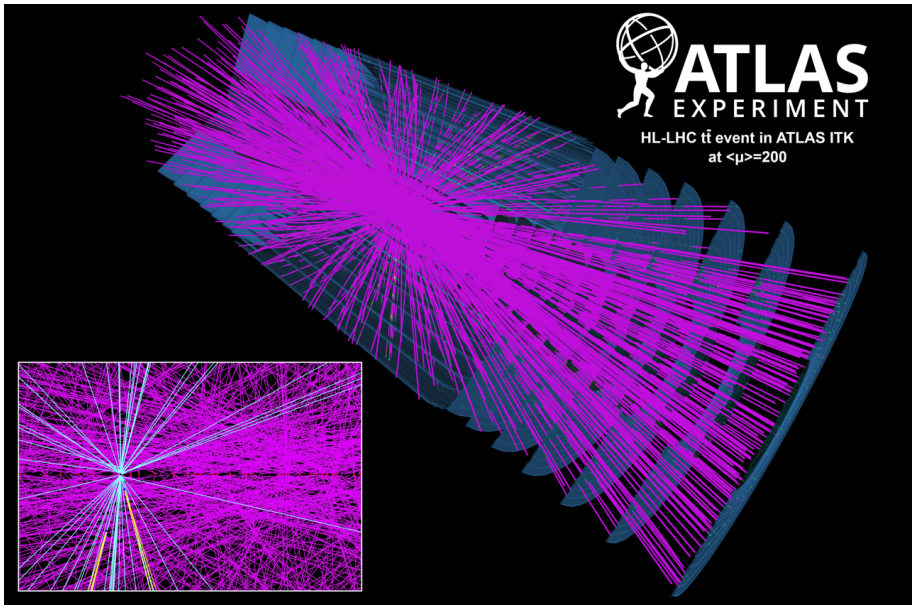

Figure 12. Simulation of a top quark pair production event with a pileup of 200 events in the ATLAS tracker, including tracks with a transverse momentum of at least 1 GeV [68]. The silicon modules are symbolized by the grey structures. Reconstructed tracks are shown in violet. The inset shows a zoom onto the interaction region and has a vertical scale of 2.5 mm and a horizontal scale of 12 cm. The tracks from the primary vertex, where the top quarks are produced, are highlighted in cyan. Two secondary vertices are reconstructed and the tracks coming from them are shown in yellow.

tracks), as well as potential secondary vertices (yellow tracks).

The tracking detectors face many challenges at the HL-LHC. Radiation induces damage in the silicon crystal lattice, which leads to three effects: increased voltage needed to deplete the sensor, increased leakage current (the current present when no particles traverse the detector), and – most importantly – reduction in the amount of collected charge, due to the charge trapping. While the first effect can be mitigated by a detector design that allows for the necessary high bias voltages, the increase of leakage current can potentially induce overheating, as the sensor currents depend exponentially on the sensor temperature. This can induce a positive feedback loop, known as thermal runaway, if the cooling capacity is insufficient. Such overheating can render the detector inoperable, and can even damage or destroy it. The detectors thus need to be cooled to lower temperatures than the present trackers, to maintain the leakage currents at an acceptable level. Reduction in the amount of charge can lead to the loss of hits, and thus lower tracking efficiency, as well as confusion of real hits with detector noise, resulting in a higher tracking "fake rate" due to wrongly reconstructed tracks, and thus worsened spatial and transverse momentum resolution.

Another challenge for tracking at the HL-LHC is the high particle density, which reduces the performance of the tracking algorithms. This is tackled by increasing the granularity of the detector, i.e. by making the individual sensor elements smaller. A higher granularity, however, results in an increase of the channel count and thus the

data volume to be sent to the off-detector electronics. The readout bandwidth has to be adapted accordingly. Another consequence is a higher power consumption.

The tracker front-end electronics have to be compatible with the increases in the L1 trigger rate and latency, e.g. in terms of readout speed, data bandwidth, and depth of data buffers in the front-end electronics, while being sufficiently radiation-tolerant to cope with the expected radiation levels at the HL-LHC.

Finally the acceptance of the tracking detectors in the forward regions will be increased, which improves the sensitivity for certain physics processes, for example vector boson scattering (treated in Sect. 5.2.4).

The tracker upgrades must be realized within an affordable power budget, and need to respect the available space in cable ducts for cooling pipes, readout fibers, and power cables.

Another important aspect is the material budget. When tracking particles, the goal is to disturb the particle trajectory as little as possible. Any material in the active, i.e. instrumented, volume deteriorates the measurement resolution and efficiency and increases the fake rate, due to multiple scattering, nuclear interactions, photo-conversions, and bremsstrahlung. All elements must therefore be as lightweight as possible, and the materials used should have large radiation lengths and nuclear interaction lengths (quantities that characterize the interaction of particles with the material). However, minimising the material can impact the performance, because, for example, the charge collection efficiency increases with the thickness of silicon in a module. In addition, the position of the detector must remain as constant as possible over time and this becomes more challenging the lighter the support structure is. For example, the material budget of the ATLAS tracker (ITk) is required to be below 2% of a radiation length per layer.

The ATLAS and CMS trackers will be completely replaced for HL-LHC operation. In the following sections we will discuss two examples: the upgrade of the ATLAS pixel detector, and the upgrade of the CMS Outer Tracker. Each experiment will also replace the component not discussed here.

3.3.1. The Upgrade of the ATLAS Pixel Detector Pixel detectors are typically located at the center of high-energy physics experiments, often mounted directly on the beam pipe, and provide three dimensional measurement points with a resolution of typically a few microns. Pixel detectors were first used in experiments located at CERN in the 1980s [69, 70] and are now commonly used in high-energy physics experiments. This section focuses on the design of the ATLAS pixel detector [57] as an example, although the future CMS pixel detector will be similar in many respects. The design is well-advanced, but not yet fully-finalized, so we report here the current status.

A key challenge for pixel detectors is the large dose of ionising radiation that they are subjected to because they are located so close to the proton-proton interaction point. This means that both the silicon sensors and the electronics circuits need to be designed to operate in such a high-radiation environment to tolerate a total radiation dose up to 7.3 MGy and a fluence up to 9×10^{15} n_{eq}/cm^2 (see

Fig. 11 for a map of the expected fluence). This requirement to tolerate an extremely high radiation environment has stimulated the development of radiation-hard electronics, which can also be used for other applications with similar requirements such as nuclear reactors or outer space.

Pixel detectors play a critical role in track and vertex reconstruction due to the precision of their measurements. This precision is driven by a number of key design factors including the size of the individual pixels, the amount of material in the detector and the distance of the first layer from the interaction point.

For track reconstruction, a key component in the precision of the track momentum measurement is the radial distance over which measurements are made determined by the distance between the first and last layers of the tracking detector. Minimising the inner radius of the pixel detector is even more important for vertex reconstruction, but the closer the layer is to the interaction point, the higher the radiation dose. The ATLAS pixel detector is planned to have an inner radius of 34 mm in the barrel and 33 mm in the endcaps, which is close to the radius of the beam pipe of 25 mm.

The size of the pixels is one of the most important factors in determining the resolution of track impact parameters, which are important for secondary vertex reconstruction and flavor tagging. Two different sizes are used in the ATLAS pixel detector. Most pixels are square with a side length of 50 μm, except the pixels in the barrel layer closest to the beampipe, which are 25 μm by 100 μm. The rectangular pixels ensure that the transverse impact parameter resolution is as precise as possible. The layout of the ATLAS pixel detector for the HL-LHC is shown in Figure 13. The individual pixel modules are shown in red and the black lines indicate the trajectories of particles produced at different angles with respect to the beam direction from the interaction point. The detector will consist of two regions: a barrel region at low z-values where the modules are arranged along cylinders, and an endcap region at higher z-values where the modules are arranged vertically and mounted on disks. There will be five layers of modules in the barrel and up to seventeen disks in each side of the endcap. In total, the ATLAS pixel detector will comprise 9400 pixel modules, with ∼5 billion channels, and it will cover an area of 12.4 m^2 of silicon.

A new feature in the ATLAS pixel detector for the HL-LHC will be the inclusion of tilted modules in the outer three layers of the endcap at moderate z-values. This tilt means that the modules will be closer to perpendicular to the particles produced at the interaction point, which will minimize the amount of material that they traverse and improves the measurement precision. It also means that the hit reconstruction efficiency of the detector in this moderate z-region will be significantly improved. In addition, the η coverage of the pixel detector has been extended up to $\eta = 4$. This increased acceptance will lead to improved physics performance, for example, on the measurement of vector boson scattering (Section 5.2.4) and on pileup rejection (Section 4.1.1).

Another new feature of the ATLAS pixel detector will be the use of 3D sensors in the innermost layer. These sensors exploit novel technology with electrodes

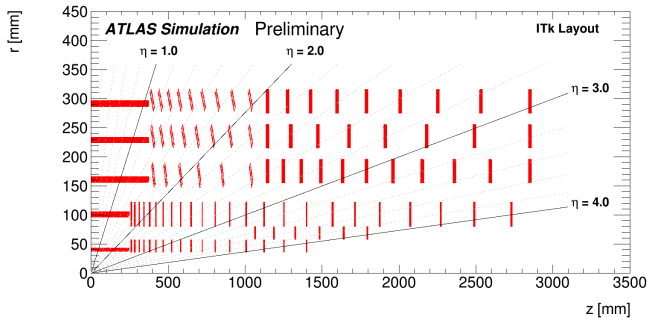

Figure 13. The planned layout of the ATLAS pixel detector for the HL-LHC [71]. A quarter of the full detector is shown along a vertical slice through the detector made parallel to the beam, which passes through the detector in the z-direction. The individual pixel modules are indicated in red. The black lines indicate the trajectories of particles produced at different angles with respect to the beam direction from the interaction point. The full pixel detector layout can be obtained by reflecting this quarter about the z and r axes.

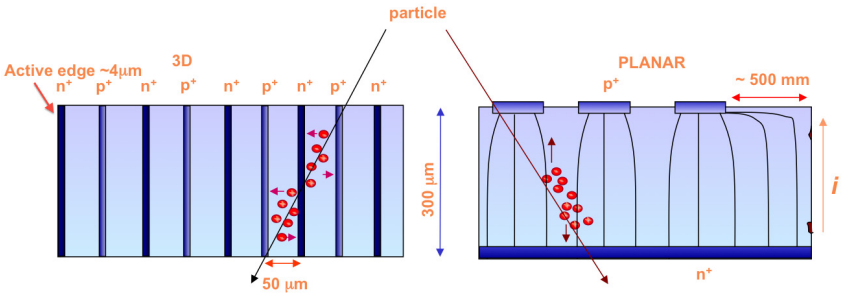

Figure 14. Left: a sketch of a 3D sensor with the electrodes extending through the sensor. Right: a sketch of a planar sensor with electrodes placed on the surface of the sensor. The arrows indicate the direction in which particles propagate through the sensors. The red circles indicate the electrons moving through the silicon to the anode and the holes (or missing electrons) moving towards the cathode. From Ref. [57].

implanted within the silicon of the modules. A sketch of such a 3D module with the electrodes indicated as the blue rectangles is shown in Fig. 14 (left) as well as a planar sensor in Fig. 14 (right). In contrast, planar silicon sensors have electrodes implanted on the surface of the sensor. An important advantage of 3D sensors is that the distance between electrodes can be made very short, while in planar sensors it is constrained to be the thickness of the wafer. This means that the distance that the charge needs to travel before being collected can be very short, so there is no significant loss of signal amplitude due to charge trapping after irradiation. This improves the response time of the detector, improves the radiation hardness, and reduces the required depletion voltage.

For the HL-LHC, ATLAS and CMS are pursuing a common development of the readout chip design for their pixel detectors within the RD53 Collaboration [72]. RD53 is using a CMOS process with a 65 nm feature size because it balances affordability with the radiation tolerance requirements for the detectors. Common

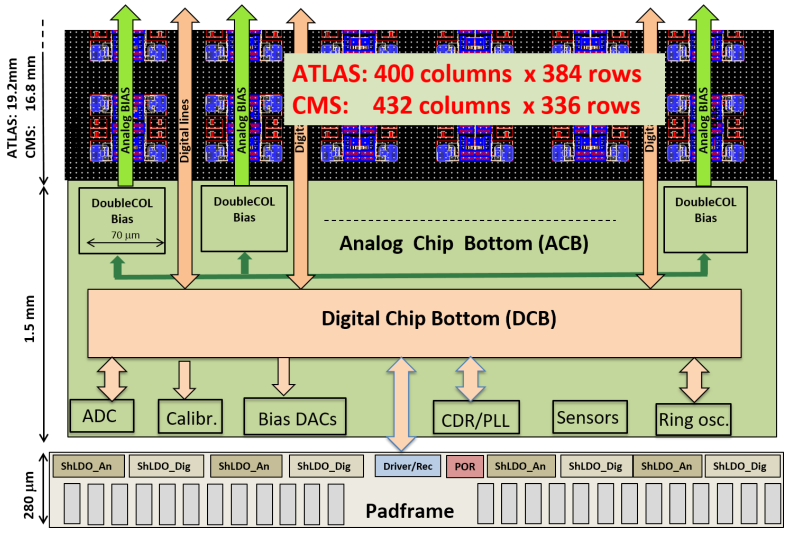

Figure 15. The layout of the RD53B chip, a prototype of the readout chips for the ATLAS and CMS pixel detectors showing the digital (peach) and analog (green) components. The arrows indicate the flow of signals in the chip. The final ATLAS and CMS chips will differ in the number of rows and columns and in the analog components. From Ref. [73].

prototypes, as shown in Figure 15, have been produced and tested before the final chips are submitted for production. This is an excellent example of how the experiments are collaborating to meet the stringent requirements of the HL-LHC and saving resources through common projects. The electronic readout for the ATLAS pixel detector has been designed for a trigger rate of 1-4 MHz, depending on the layer, with an output bandwidth of up to 2.4 Gb/s per readout chip [71].

The ATLAS pixel detector has stringent requirements in terms of the performance. It is designed to obtain (together with the strip detector) a track reconstruction efficiency of better than 99% for muons and better than 85% for electrons, while limiting the rate of wrongly reconstructed tracks (or fakes) below 10^{-5} [71]. Additional requirements include a pixel occupancy below 1% and for the detector performance to be robust even if 15% of the channels have been lost.

3.3.2. The CMS Outer Tracker Phase-2 Upgrade The design goals for the new CMS tracker [55] include improved radiation hardness, maintaining or improving the current tracking performance despite of increased pileup, and to provide tracking information to the L1 trigger decision. The detector is split radially into an Inner Tracker (the pixel detector) and an Outer Tracker (OT). The latter is the focus of this section.

The requirement for the OT to inform the L1 trigger decision drives the OT silicon module design and consequently the whole OT design.

The L1 trigger receives information at the bunch crossing frequency of the LHC, i.e. at 40 MHz. As it is impossible to read out the complete OT at 40 MHz, due to bandwidth limitations, a different approach was found which aims to select events with high momentum tracks most relevant for physics analyses. The principle is

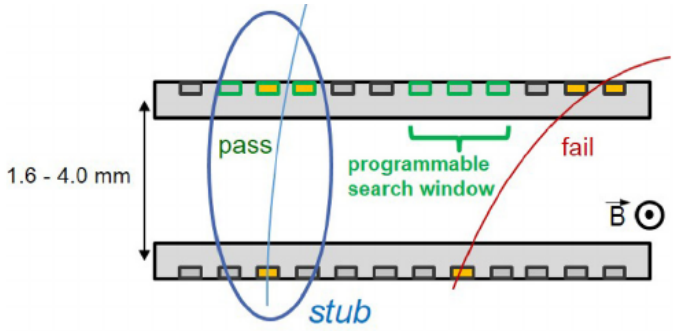

Figure 16. Illustration of the CMS Outer Tracker module concept [74]. A cross section through the two sensors (grey) of one module is shown. In each sensor the strips are indicated by the small rectangles. Strips with a hit are colored in yellow. The hit acceptance windows in the top sensor, seeded by the bottom sensor hits, are indicated in green. The track shown in red has a low transverse momentum and small radius of curvature (large bend), and crosses the top sensor outside the acceptance window. The high momentum track colored in blue instead passes through the acceptance window.

illustrated in Fig. 16. The tracks bend in the 3.8 T magnetic field of the CMS solenoid, and the radius of curvature is proportional to the transverse momentum of the particle. Silicon modules are constructed from two sensors, mounted on top of each other separated by a distance of 1.6-4.0 millimeters. The hit patterns in the two sensors depend on the track's transverse momentum, p_{T}. The hit patterns from both sensors are made available to a single readout ASIC, which correlates the hit patterns. Depending on the size of the allowed (programmable) acceptance window in the top sensor, tracks with a p_{T} above a certain threshold can be identified. Only the hits belonging to such high p_{T} two-hit track segments (called "stubs") are passed on to the L1 track finder. Tracks are formed within the trigger latency, using complex data processing cards, located in the counting room. Those tracks are combined in the L1 trigger with the information received from the calorimeter and muon systems. When a L1 trigger accept signal is received by the tracker, the full event information, including hits from low p_{T} tracks, is read out.

Two types of modules, shown in Fig. 17, are used in the OT. The two module types feature different granularity and thus spatial resolution, and are optimized for different regions in the OT, as explained later. The 2S ("two strip sensors") module uses two strip sensors, with two rows of 5 cm long strips per sensor. The PS ("pixel / strip sensors") module instead uses a bottom sensor patterned into large pixels, or macro-pixels, of 1.5 mm length, and a top sensor with two rows of 2.4 cm long strips. The 2S sensors are about 10 cm × 10 cm in size, while the PS sensors have dimensions of 5 cm × 10 cm. Strips are connected by wire-bonds to printed circuit boards (named front-end hybrids) that carry the readout ASICs. The macro-pixel sensor is bump-bonded, i.e. connected with metal ball contacts, to another type of readout ASIC across the whole sensor area. Additional boards, named service hybrids, are arranged on the module side faces. They are responsible for data aggregation and processing, and distribute the required supply voltages to

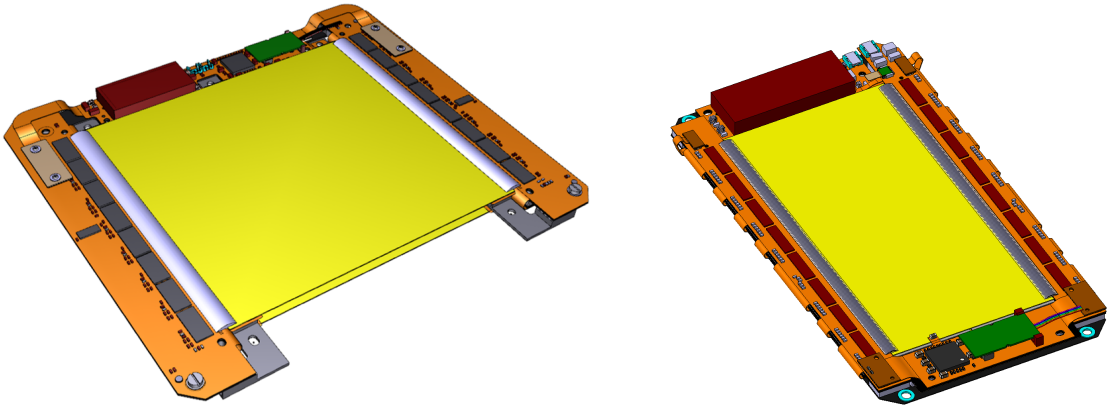

Figure 17. Drawings of a 2S (left) and a PS (right) module of the CMS Outer Tracker. The silicon sensors are depicted in yellow, the wire-bonds in grey, and the various hybrids in orange. Updated from Ref. [55].

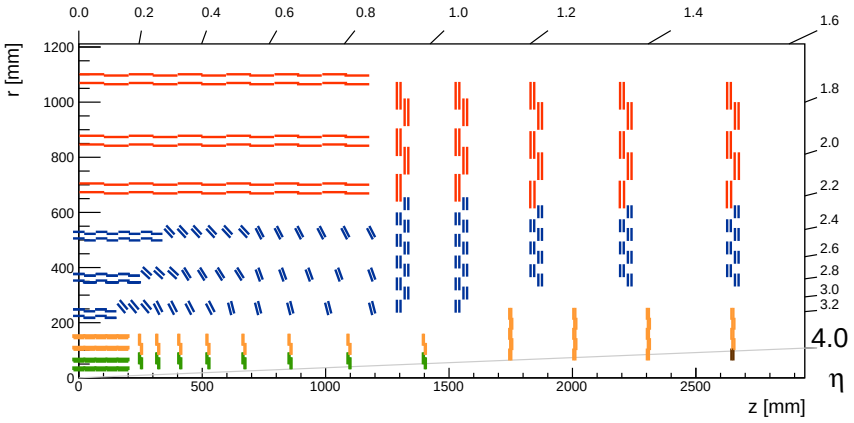

Figure 18. Layout of the CMS Phase-2 tracker [74]. One quarter of the detector is shown in rz view. Pixel modules are indicated with green and yellow lines, respectively. PS modules are shown in blue and 2S modules in red.

the module electronics. All components are glued to support pieces made from an aluminum / carbon fibre composite material with high thermal conductivity. Each module is a self-contained unit, requiring a back-end connection via three wires and two optical fibres only. Some modules have different sensor spacings, in order to equalize the p_{T} threshold and the stub data volume between different tracker regions.

The tracker layout is shown in Fig. 18. PS modules provide better resolution in the beam direction (z), due to their smaller cell size along z, in particular in the macro-pixel sensor. This makes it possible to constrain the origin of the trigger tracks to a region of about 1 mm in z, and thus to distinguish different vertices at the L1 trigger level. The PS modules are thus installed in the inner layers, at radial distances below 60 cm. Further outside the lower-granularity 2S modules are installed, which is acceptable as the hit density is much lower there. Equipping the whole volume with PS modules would be unaffordable, both in technical terms (data volume, power consumption, cooling requirements) and cost. In Fig. 18 it can also

be seen that the OT is featuring a cylindrical barrel equipped with 2S modules, a partly cylindrical, partly tilted arrangement of PS modules, and one endcap with both 2S and PS modules per side. As for the ATLAS pixel detector, the tilting implies that the tracks hit the modules predominantly perpendicularly, which leads to less material being traversed, and thus to better resolution and to a higher trigger efficiency. In the endcaps the modules are arranged in rings on disks. The total area of all silicon sensors together amounts to about 190 m^2.

The modules are mounted on light-weight carbon fiber support structures. Figure 19 shows, as an example, how the modules are arranged in the endcap disks. To achieve hermeticity (i.e. no gaps) both in ϕ and r, four layers of modules are needed, with modules mounted on both sides of two closely-spaced disks. PS modules cover the area close to the beam pipe, while 2S modules are arranged at larger radii. It is worth noting that the same rectangular modules are used in the barrel and endcaps, even though wedge-shaped modules would be slightly more economical in terms of coverage – this disadvantage is compensated for by the advantage of having fewer types of modules to develop and build.

One important improvement of the new tracker is the use of an evaporative two-phase cooling system with CO_2 as coolant, replacing the liquid mono-phase cooling system based on C_6F_{14} that was used before. In a mono-phase cooling system heat is removed by heating up the liquid, while in a two-phase cooling system heat is absorbed as latent heat in the phase change, from liquid to vapour phase, i.e. when the liquid evaporates, which is much more efficient. The new cooling system will use pipes with a smaller diameter and will reach lower temperatures, while also being more environmentally friendly and cheaper. The new cooling system will run at $-35\,^{\circ}\mathrm{C}$, while the present one is running at about $-20\,^{\circ}\mathrm{C}$.

Another important improvement, concerning the power delivery, is the usage of so-called DC-DC converters, placed on the service hybrids of the silicon modules. These devices allow the power to be supplied to the detector modules at a higher voltage, e.g. 10 V, while the front-end electronics require voltages of 1-2 V. As a consequence, the supply currents to be transmitted via the about 60 m long supply cables are lower, leading to lower voltage drops and drastically reduced power losses in these cables, which in turn allows one to use less material in the detector for supplying the power.

A total of 7600 2S modules and about 5600 PS modules are needed, requiring more than 26,000 silicon sensors and 45,000 complex electronics hybrids of various types. The organization of the mass production, including rigorous, yet efficient quality control of the components, is a major challenge. The development of the respective procedures and test systems, both in terms of hard- and software, is a project in its own.

3.4. The CMS Endcap Calorimeter Upgrade

During HL-LHC running, the calorimeters will also be exposed to more challenging running conditions [58], with about five times higher instantaneous luminosity,

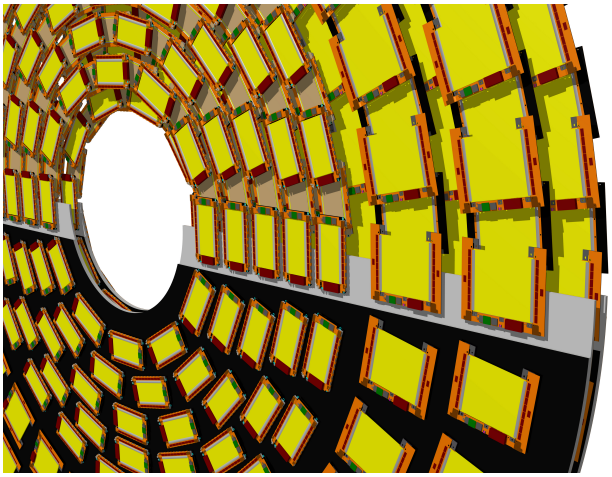

Figure 19. View onto an endcap double-disk of the CMS Outer Tracker, showing the arrangement of the PS and 2S modules [55]. In the upper half the support structure is removed, so that the arrangement of modules in the four layers is visible.

higher event pileup and much harsher radiation levels. This will especially affect calorimeter segments close to the beam line and in the forward directions. When the lead tungstate ($PbWO_4$) crystals used in the current electromagnetic calorimeter are exposed to radiation, they become progressively less transparent to light. Studies have indicated that, for the radiation levels in the endcap region ($\eta > 1.5$), the radiation-induced loss of transparency of the CMS ECAL's $PbWO_4$ crystals will be irreparable and the endcap ECAL detector needs to be replaced.

CMS will replace both the forward ECAL and HCAL calorimeters with a novel high granularity sampling Calorimeter Endcap (CE) [59] in the region $1.5 < \eta < 3.0$. The aim is to maintain or improve the current endcap calorimeter performance, in the much higher interaction rate environment of the HL-LHC. Increasing the readout granularity of the detector is like reducing the pixel size in a camera. As the camera with finer pixels will be able to resolve finer details, the calorimeter with higher granularity will be able to resolve particles very close to each other. It reinforces the upgrade of the tracker detector with coverage in the forward region.

The design of the 3-dimensional imaging CE is based on radiation-tolerant detector technology with unprecedented fine granularity in all three spatial dimensions (initially developed for calorimeters at a linear collider [75]) and the particle flow (PF) concept, to ensure the excellent energy resolution and pileup mitigation required by the physics of the HL-LHC. The particle flow method is based on reconstructing individual particles by associating the measurements in the electromagnetic and hadronic calorimeters with the information from the tracking detector. In this method, the energies of photons and electrons are measured in the ECAL, and the energies of neutral hadrons are measured in both the ECAL and HCAL. The momenta of charged particles are measured by the tracker. For the charged hadrons, the energy is computed by a weighted combination of the track momentum and energy clusters in the calorimeters.

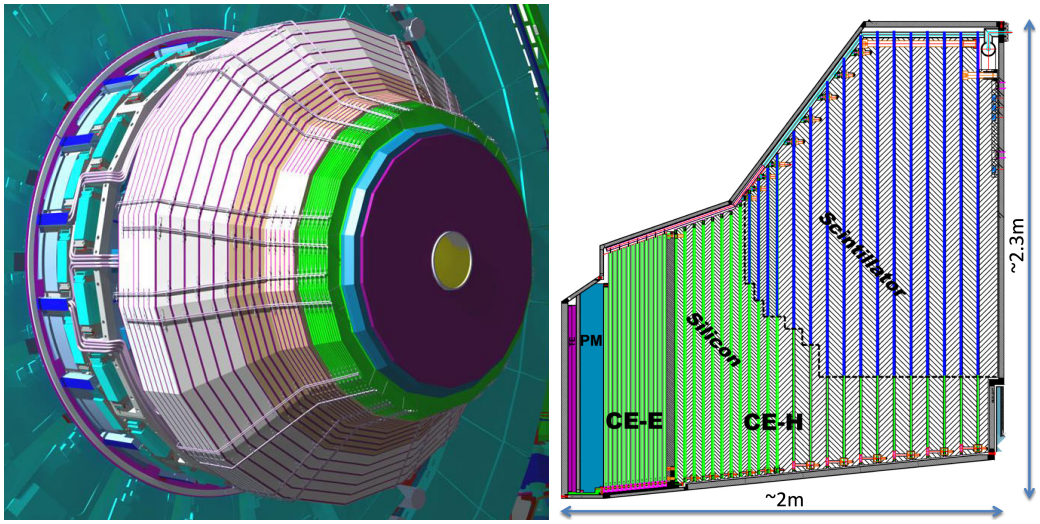

Figure 20. Left: three-dimensional view of an assembled CMS calorimeter endcap, including cooling loops and manifolds. Right: longitudinal cross section of one half of one endcap of the CMS calorimeter endcap design. From Ref. [59].

Hence PF calorimeters are highly-segmented imaging devices which emphasize high granularity and hence superior two-particle resolution over energy resolution, providing a multi-dimensional view of the particle shower. The high granularity enhances the efficiency for particle identification (including within the core of "jets" from extremely collimated sprays of particles), and provides good energy resolution, a precise measurement of the location of particle showers and pileup rejection. Together with the measurement of the time of arrival of the particles, the CE will be able to associate the particles with the collision vertex they originate from, and determine if the particle shower originates from the hard scatter vertex or from a pileup collision vertex.

Figure 20 shows a 3-dimensional view of a CMS calorimeter endcap (left panel) together with a longitudinal cross section of one half of one of the endcaps (right panel). CMS deploys a novel technique that uses silicon sensors as the active material to implement the needed fine lateral and longitudinal segmentation and precision timing measurements of the particle showers and to provide sufficient radiation hardness close to the interaction point and at high pseudorapidities. Lead, copper, copper-tungsten and stainless steel are used for the absorber. This is the first instance of silicon sensors being used as active material at such a large scale in a collider calorimeter. Further from the interaction point and at smaller pseudorapidities, where the radiation exposure is lower, the detector layers are built with highly segmented plastic scintillator tiles with silicon photomultiplier (SiPM) readout instead of silicon sensors, to optimize the trade-off between cost and radiation tolerance.

The CE is composed of 50 layers of silicon or scintillators, with the electromagnetic section (CE-E) with 28 layers in the front, and the hadronic section (CE-H) with 22 layers in the rear. Figure 21 shows two sample layers, a layer in the CE-E that consists entirely of silicon sensor modules on the left and a layer in

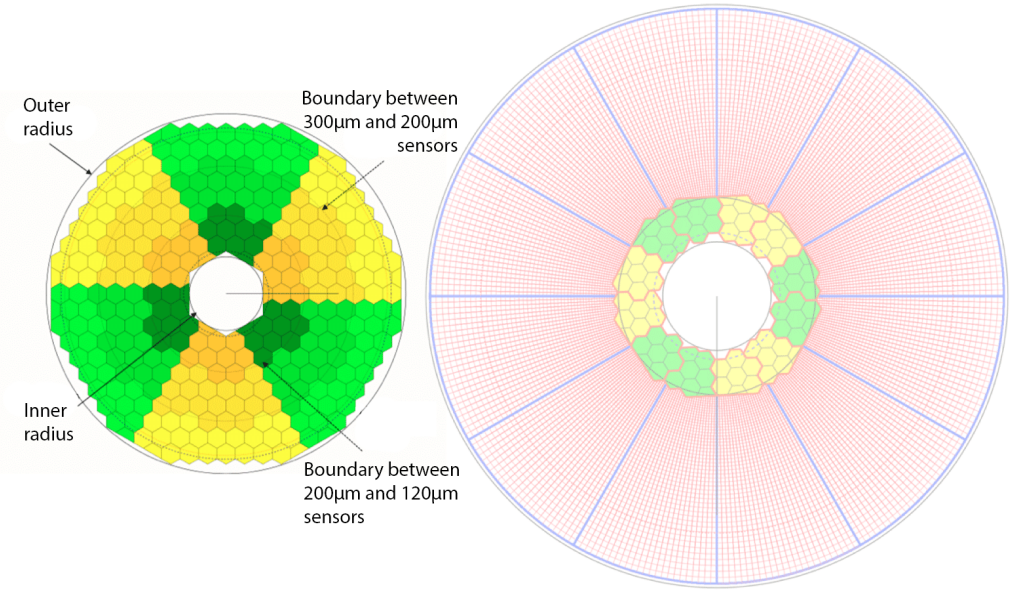

Figure 21. Layer types in the CMS Calorimeter Endcap: a CE-E layer which consists entirely of silicon modules (left), and a CE-H layer which has both silicon and scintillator modules (right).

the CE-H that consists of silicon modules at small radii and scintillator modules at large radii. The yellow and green colored silicon modules show the division into six cassettes, each covering 60° in azimuth. The thickness of the CE-E amounts to 25 electromagnetic radiation lengths (X_0) and 1.3 hadronic interaction lengths (λ_I), while the thickness of CE-H, which is deep enough to contain the hadronic shower, is 8.5 λ_I.

The hexagonal silicon sensors are manufactured from circular 8" silicon wafers and make effective use of the wafers. The thickness of the sensors varies between 300 μm, to maximize the signal in the parts of the detector with the lowest radiation exposure at large radii, 200 μm at intermediate radii, and 120 μm to limit the leakage current in parts of the detector with the highest radiation exposure at small radii. The sensors are further segmented into silicon diodes of hexagonal shape. The thinnest sensors feature 432 segments that cover an area of 0.5 cm^2 each, while for the thicker sensor types, 192 segments with an area of 1 cm^2 each are used. The smaller cell size in the inner regions improves pattern recognition and increases the signal-to-noise ratio for minimum ionizing particles, as the signal is lower for thinner sensors, while the noise increases with capacitance and thus cell size.

Modules are assembled by stacking up a base plate, made of a copper-tungsten composite in CE-E and a flame-resistant composite in CE-H, a Kapton-gold sheet, a silicon sensor, and a printed circuit board with the front-end electronics (hexaboard). There are about 30,000 modules with approximately six million channels which cover an area of 620 m^2 of silicon, corresponding to about 55% of the active area of CE. The remaining 400 m^2 of active area are covered by about 240,000 scintillator tiles with SiPM readout.

Cassettes are assemblies which cover 60° wedges and consist of modules mounted

on both sides of copper cooling plates with electronics motherboards, which cover the on-detector electronics and supply low voltage power to the modules. In the CE-E, the absorber is part of the cassettes and consists of the copper-tungsten base plates, the copper cooling plates and stainless-steel clad lead plates. In CE-H the cassettes are placed between stainless steel absorber plates. The cassettes are assembled into two endcaps (Fig. 20) that weigh about 215 tons each. In order to mitigate the effects of radiation, and ensure operations for the full HL-LHC lifetime, the silicon sensors and SiPMs will be operated at below $-30°$C to reduce the leakage currents. Similar to the CMS tracking system, the calorimeter uses a two-phase CO_2 cooling system.

The new CMS endcap calorimeter represents a change in paradigm for calorimeters at hadron colliders. Its expected performance is described in Section 4.1.2.

3.5. Timing Detectors

As the duration of the collisions within the bunch crossing ranges from 175 to 260 ps, proton-proton interactions can occur close together in space but separated in time by hundreds of picoseconds (Fig. 22, left). Timing detectors provide a completely independent and orthogonal measurement to separate particles emerging from two such overlapping proton-proton interactions: the precise measurement of the arrival time of charged particles emerging from the collisions (Fig. 22, right). Simulations show that technology with a superb resolution for the time measurement of 30-50 ps per track during the whole life time of the HL-LHC would allow both experiments to further reduce the effect of pileup with significant margin during operation with 200 interactions per bunch crossing. The timing information helps to distinguish overlapping vertices, however the definition of the hard scatter (HS) vertex must come from a complementary measurement (such as highest track $\sum p_{\mathrm{T}}^2$).

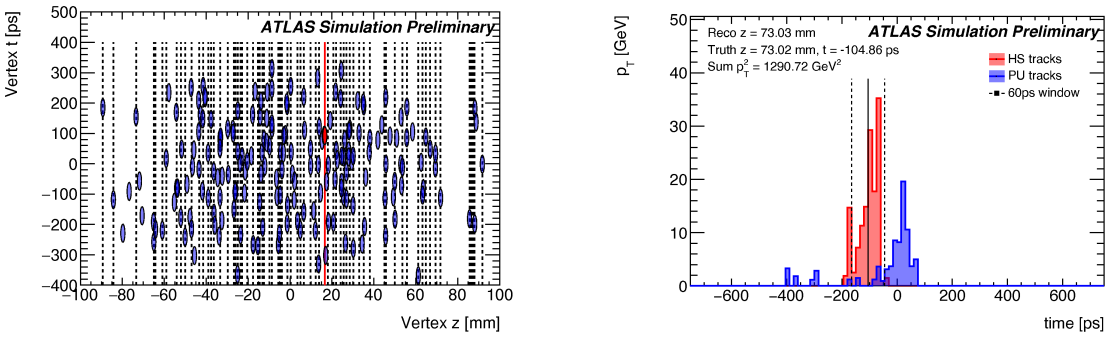

Figure 22. Left: simulation of a collision event, which takes 1000 ps, with 200 simultaneous interactions. The individual interactions occur at certain locations along the beam direction (z) and at a certain time. When two vertices have the same vertical line, i.e. happen at the same place, but have a different collision time, it is possible to clearly distinguish particles emerging from each interaction. This illustrates the motivation for high precision timing. The hard scatter vertex spatial (space and time) position is highlighted as a red line (ellipse) [76]. Right: transverse momentum of tracks reconstructed within the same jet, labeled based on the time measurement as coming from the interaction of interest (red) or from pileup (blue). Once the hard scatter vertex (and hence the t_{HS}, solid line) is defined, only tracks within a 60 ps window (dashed lines) are accepted for event reconstruction [76].

Both collaborations performed complex optimization studies of effects of adding the timing technology to the event reconstruction. Studies of the expected performance of the ATLAS Inner Tracker showed that a significant improvement of the offline event reconstruction in ATLAS can be achieved by adding the High Granularity Timing Detector (HGTD) [66], providing a high timing precision, at a distance of approximately 3.5 m from the interaction point and with an η coverage of $2.4 < |\eta| < 4$ (Fig. 23, top). In combination with the ITk, high quality particle identification and pileup mitigation is ensured. The CMS Collaboration will install the Minimum Ionizing Particle Timing Detector or MTD (Fig. 23, bottom) [65] consisting of the Barrel Timing Layer (BTL) in the central region and the Endcap Timing Layer (ETL) in the forward region. Because CMS will reach almost full spatial coverage of its instrumented solid angle through the MTD, the use of four-dimensional trigger and vertexing algorithms will be enabled.

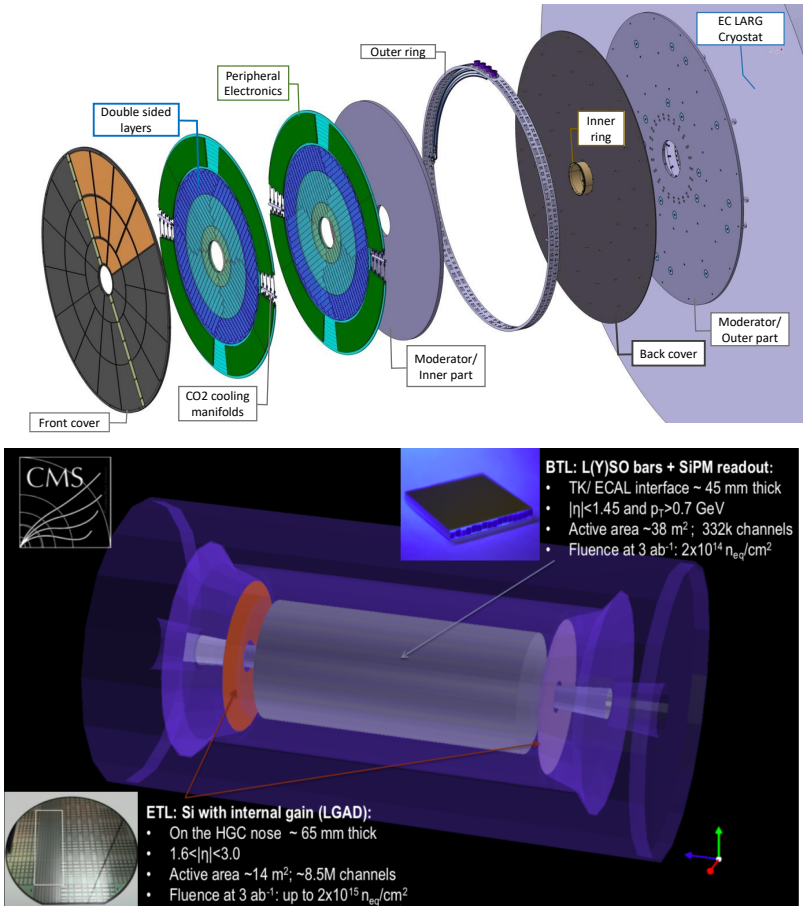

Figure 23. Top: schematic picture of the High Granularity Timing Detector used in ATLAS [66]. Bottom: the Barrel Timing Layer (BTL) and Endcap Timing Layer (ETL) of CMS [65].

3.5.1. ATLAS High Granularity Timing Detector The requirement for high precision of the timing measurement (30-50 ps per track) and a fast response combined with the harsh radiation environment - the detector will need to withstand a fluence of $2.5 \times 10^{15}\, n_{\mathrm{eq}}\,\mathrm{cm}^{-2}$ and a total ionisation dose of 2.5 MGy during its lifetime - puts stringent restrictions on the technologies which can be used. After thorough testing, a special type of silicon sensor was selected for the HGTD: the Low Gain Avalanche Detectors (LGADs) [77], which are 50 μm thick p-n sensors with a layer highly enriched with boron which creates an avalanche of electrons once a charged particle passes through (Fig. 24, left). This avalanche then provides a fast signal above the background noise. The size of an individual sensor is $1.3 \times 1.3\,\mathrm{mm}^2$ which ensures an occupancy below 10%. The total number of channels will be approximately 3.6 millions.

The design of the HGTD consists of two thin disk modules (on each side of ATLAS), which will be installed between the ITk and the endcap calorimeters with a combined width of 7.5 cm at a distance from the center of ATLAS of ± 3.5 m. Each module consists of two layers instrumented with LGAD sensors, readout chips and cooling circuits. The active area of the detector is $6.4\,\mathrm{m}^2$ and stretches from 120 mm to 640 mm in radial distance from the beam axis (corresponding to a pseudorapidity

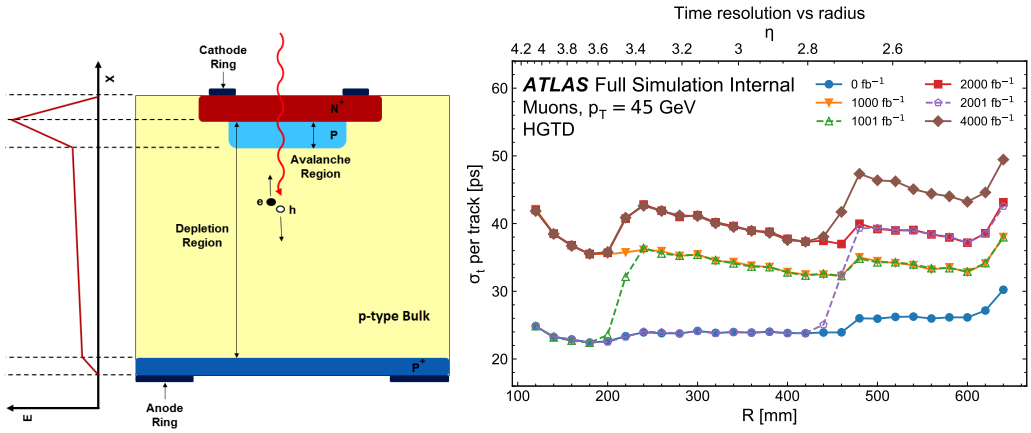

Figure 24. Left: schematic cross section of the Low Gain Avalanche Detector illustrating the p-n diode with the enriched "avalanche" region used to multiply the effect of a charged particle (red arrow) passing through the sensor. The graph on the left illustrates the electric field produced from the applied voltage highlighting the avalanche region [76]. Right: dependence of the timing resolution of the ATLAS High Granularity Timing Detector on the radial distance from the beam pipe for different integrated luminosities. The ultimate data set of 4000 fb^{-1} is considered and corresponds to the brown line. The performance of non-irradiated sensors is shown in blue. The section closest to the beam pipe (120-240 mm) will be replaced 3 times, therefore the lines corresponding to 1000, 2000 and 4000 fb^{-1} coincide. The middle section (230-470 mm) will be replaced at half-time of the experiment, therefore the lines for 2000 and 4000 fb^{-1} coincide. The 1001 and 2001 fb^{-1} lines demonstrate the restoration of resolution after replacement. The outer section will stay for the whole HL-LHC data taking period, therefore a degradation for all steps is visible [66].

range of 2.4-4.0); the support structure and services reach to 1100 mm in total.

As expected from the position of the HGTD within the ATLAS detector (Figure 11, the HGTD position is labeled as "Timing det."), the exposure to radiation will be very high due to the proximity to the beam pipe and the interaction region. The required performance of irradiated LGADs up to the highest expected radiation levels was confirmed using test beam studies. In order to ensure a timing resolution between 25 and ∼45 ps over the lifetime of the HL-LHC project, the HGTD is divided into three concentric rings. This allows individual rings to be replaced; one replacement is planned for the middle section, while the ring closest to the beam pipe will be replaced three times. The time resolution per-track as a function of the radial distance is presented in Fig. 24 (right), indicating the effect of the radiation damage and replacements.

The development of LGAD sensors is another example of a common project of the ATLAS and CMS Collaborations.

3.5.2. CMS MIP Timing Detector The Minimum Ionizing Particle Timing Detector consists of two distinct parts - the Barrel Timing Layer (BTL) and the Endcap Timing Layer (ETL).

The Endcap Timing Layer is located at a similar position to the HGTD and

is therefore designed with the same LGAD technology. The ETL consists of two layers with sensors and is placed in front of the CMS High Granularity Calorimeter Endcap (Fig. 20). The major difference in design with respect to ATLAS is that the closest distance of the MTD to the beamline is 315 mm, so the detector will be exposed to much less radiation than the HGTD. Therefore no exchange is planned for the ETL during the entire data taking period. The surface area of the ETL is $14\,\mathrm{m}^2$, resulting in approximately 8.5 million channels.

The Barrel Timing Layer is relatively far from the beam line (1160 mm at the closest point) and therefore the radiation levels are almost two orders of magnitude lower than for the ETL. In addition, since a much larger area of $38\,\mathrm{m}^2$ needs to be covered without stringent requirements on the thickness of the sensor, a different technology has been adopted, which also meets the requirement of 30 ps timing resolution. The BTL features one layer of scintillating LYSO crystals (cerium doped silicate based heavy crystal scintillators, $Lu_{2(1-x)}Y_{2x}SiO_5$) [78]. These crystals are about 5.7 cm long with a transverse area of about $3 \times 3\,\mathrm{mm}^2$ oriented toward the interaction point. Each one is read out at each end by a SiPM. Both the crystals and the SiPMs have already been proven to be radiation tolerant up to a neutron equivalent fluence of at least $2 \times 10^{14}\,\mathrm{cm}^{-2}$ and a total integrated dose of 25 kGy, when sufficiently well cooled. Figure 25 shows the hierarchical arrangement of the various components and illustrates the location of the BTL modules inside the tracker support tube. In total there are 331,776 channels in the BTL.

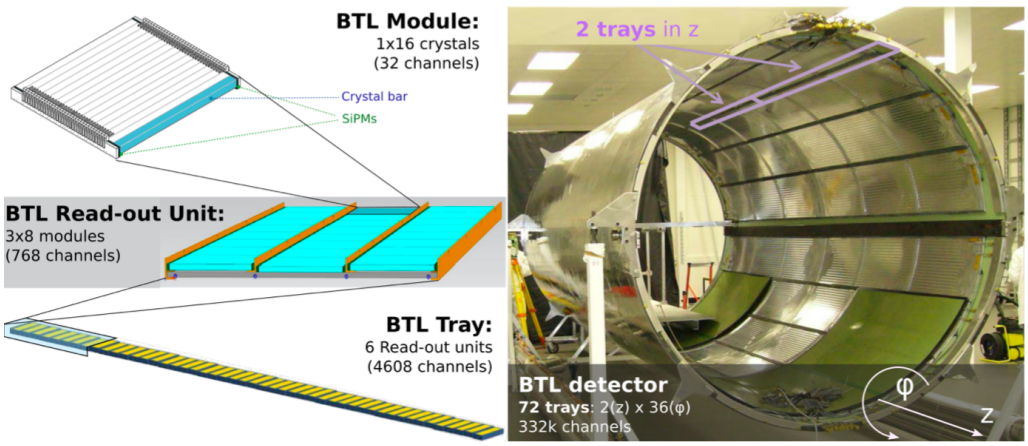

Figure 25. Overview of the BTL showing the hierarchical arrangement of the various components, bars, modules, Readout Units, and trays, inside the tracker support tube [79].

4. Detector, Object and Computing Performance

The ATLAS and CMS detectors are large and complex devices with billions of readout channels each. The readout signals form the basis for the particle and event reconstruction which - except for the trigger systems - is performed outside of the experimental caverns at the main CERN Computing Center [80] and around the world within the LHC Computing Grid [81].

Realistic computer simulation is needed to understand, or at least model, detector effects and correct for their impact on physics results to be able to compare with theoretical predictions. Therefore, large amounts of simulated data have to be produced, using sophisticated computer programs such as Geant4 [51] to simulate the physics of each event and the physics processes the particles undergo when passing through the detectors. The technique is known as Monte Carlo simulation, referencing the world famous casino, because random numbers are used to select between the different physics processes weighted according to the probability of each process occurring. While historically the collaborations have relied on the precise simulation of physics processes using Geant4, the colossal statistics required for the HL-LHC mean that significantly faster and slightly less precise simulation techniques will also be used.

The following sections describe the reconstruction of signals from the detector-level quantities (Sec. 4.1) to physics objects (Sec. 4.2) and the computing infrastructure that enables it (Sec. 4.3).

4.1. Detector and Reconstruction Algorithm Performance

Each component of the detector is designed to measure specific quantities, such as the transverse momentum (through the track curvature of the charged particle trajectory) or the energy (through the total energy deposit in a calorimeter). Tracks and calorimeter deposits are crucial components of event reconstruction and depend on both the detector performance and the sophisticated algorithms used to reconstruct them. In the following, we discuss briefly the tracking performance of the new trackers, and the performance of the new CMS endcap calorimeter. While the performance of the ATLAS calorimeter is not discussed in detail as there are fewer upgrades planned, its performance fully meets the requirements of the HL-LHC.

4.1.1. Tracking Performance Complex pattern recognition algorithms are used to reconstruct the trajectories of particles passing through the tracker. These reconstructed trajectories are called tracks. The challenge in tracking is to identify all the hits that originate from the same particle in a very busy environment with many close-by hits. Tracks form the basis for the reconstruction of charged leptons (electrons, muons, and taus) and charged hadrons, and are used directly in certain specialized analyses such as the disappearing track analysis (Sect. 5.3). Charged particles describe an approximately helical trajectory in the homogeneous solenoidal magnetic field in the tracker volume. The radius of curvature of the reconstructed track is used to measure the transverse momentum of the corresponding particle. The distance of closest approach of the tracks with respect to the interaction point is exploited to discriminate between prompt tracks which originate from the primary vertex and displaced tracks from secondary decay vertices.

The expected performance of the new detectors for HL-LHC are assessed with simulation, in which the simulated paths of the particles are known and can be compared to the reconstructed tracks.

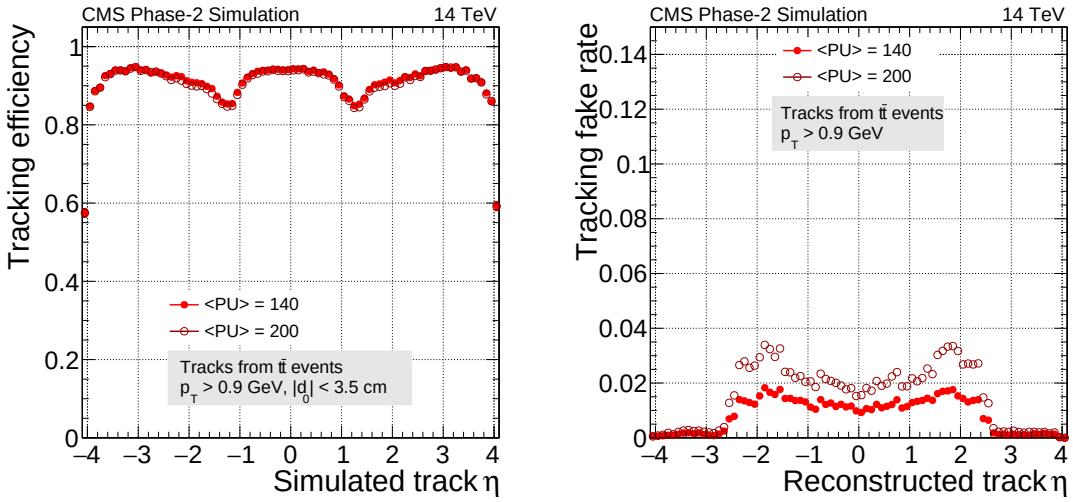

Figure 26. Tracking efficiency (left) and fake rate (right) of the upgraded CMS tracker as a function of the pseudorapidity [55]. Top quark pair production events with 140 (full circles) and 200 (open circles) pileup events have been simulated. The pixel detector is included in this simulation.

Two important figures of merit are the tracking efficiency, i.e. how many of the charged particles that traversed the detector are reconstructed as tracks, and the track fake rate, i.e. the fraction of reconstructed tracks that do not correspond to real particle trajectories but instead to combining hits from multiple trajectories or from detector noise. Figure 26 shows the expected tracking efficiency and fake rate for the upgraded CMS tracker. A simulation of top quark pair production events with either 140 or 200 pileup events shows that, in general, the efficiency of the algorithmic performance of the tracking algorithms is very close to 100% for tracks which produce hits in sufficient number of layers. The main cause of inefficiency is due to the interaction of particles with the detector material and hence the tracking efficiency is determined by the distribution of the material. Close to the center of the detector the amount of material is low and the efficiency becomes as high as 90%. It then drops slightly through the transition region between the barrel and endcap, increases again in the endcap before dropping again in the very far forward region. The fake rate is below 2% for a pileup of 140 events. The performance with pileup of 200 events is similar to the performance of the present detector at a pileup of 70 events. The efficiency for the ATLAS ITk is comparable to that shown here for CMS, however, the fake rate for tracks with $p_{\mathrm{T}} > 1$ GeV is 10^{-3}% and constant as a function of η [71]. The difference is mostly due to extensive optimization of the tracking algorithms for the new detector and also due to the design of the detector in which offline performance was a key consideration.

The tracker performance can also be characterized with the resolutions of the track parameters. Tracks are typically parametrized as a function of five parameters, related to the track angles, the transverse momentum, and the distances of closest approach to the interaction point (also called transverse and longitudinal impact parameters). Figure 27 (left) illustrates the improvement in the transverse impact

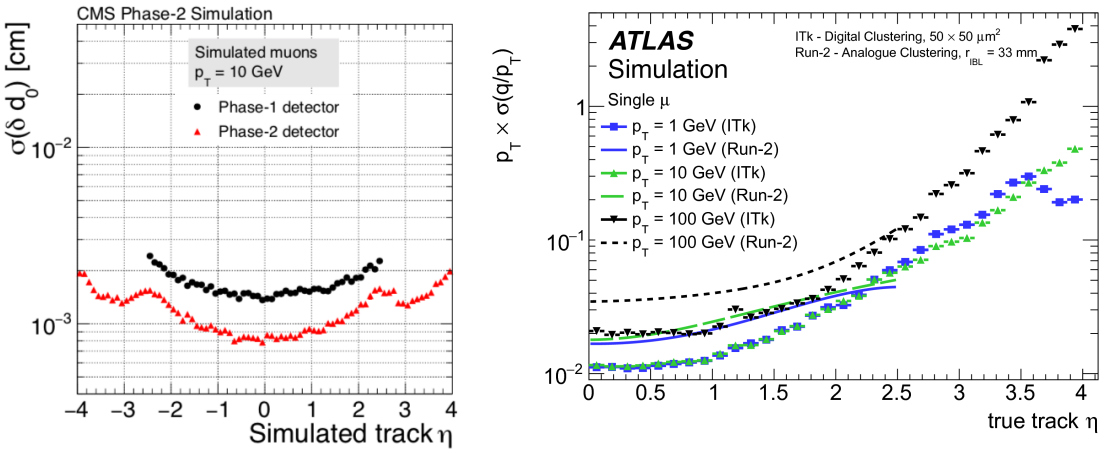

Figure 27. Left: resolution in the transverse impact parameter, d_0, as a function of pseudorapidity for the upgraded CMS tracker, for simulated single muon events with a transverse momentum of 10 GeV [55]. The Phase-2 detector (red) is compared to the present tracker (black). Right: relative transverse momentum resolution of the ATLAS tracker as a function of pseudorapidity, comparing the expected HL-LHC performance (symbols) with the performance measured during Run 2 (lines) for tracks with a transverse momentum of 1 GeV (blue), 10 GeV (green), and 100 GeV (black) [65].

parameter resolution for the upgraded CMS tracker. Using a simulation of single muon tracks, it can be seen that the resolution is below 10 μm in the central part of the detector, much better than for the present tracker, and 20 μm at the edge of the acceptance. Figure 27 (right) shows the expected relative transverse momentum resolution for the new ATLAS tracker as a function of pseudorapidity. For all three depicted momentum ranges, i.e. 1, 10 and 100 GeV, the resolution is expected to be better than for the present detector. In addition, both the upgraded ATLAS and CMS trackers are extended in the forward region up to $|\eta| < 4.0$, whereas coverage of the present trackers is limited to $|\eta| < 2.5$.

The correct association of trajectories of charged particles from all collisions in a bunch crossing is of crucial importance for event reconstruction. Complex vertexing algorithms identify each individual proton-proton collision and, in addition to selecting the primary interaction of interest, they reduce the number of pileup tracks mis-assigned to the collision of interest. While the trackers use only spatial information in the vertexing, the inclusion of the time information from the timing detectors in the reconstruction enables 4-dimensional vertexing. Figure 28 (left) shows for CMS the number of pileup tracks wrongly associated to the primary vertex of interest, as a function of pileup density [65]. Including the measurement of the time-of-flight of each particle by the MIP timing detector considerably reduces the number of incorrectly assigned particles.

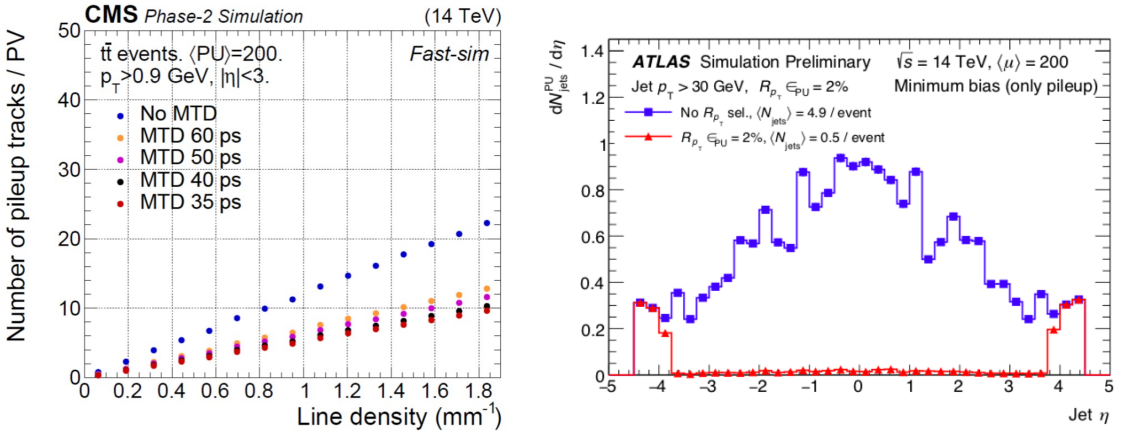

Figure 28. Left: number of pileup tracks incorrectly associated to the vertex of interest in top quark pair production events with 200 pileup events super-imposed, as a function of pileup density, without (blue) and with timing information from the MTD being used [65]. Right: average number of pileup jets associated with the collision of interest in the ATLAS detector. Without mitigation techniques, the blue curve is expected, while the distribution after pileup mitigation is depicted in red [56].

The trackers are also crucial in mitigating the effects of pileup on other physics objects. Figure 28 (right) presents the power of the expected pileup mitigation based on track association to the primary vertex as used by the ATLAS tracking system. If no pileup suppression were applied, each event would contain on average 4.9 jets from pileup with a transverse energy larger than 30 GeV. When applying all combined mitigation techniques, the number of jets from pileup drops to almost zero in the tracking acceptance, and to below 0.5 per event in the whole accessible calorimeter volume. For details on jet and pileup mitigation performance, see Section 4.2.2.

4.1.2. Calorimeter Performance Most particles deposit all their energy when absorbed in the dense material of the calorimeter. The sum of all the signals in the calorimeter segments from a particle allows the total energy of the particle to be measured. In addition, the longitudinal and transverse profiles of the energy provide information about the type of particle. An important figure of merit for the calorimeter performance is the resolution with which particle energies are measured. The performance of the new CMS calorimeter endcaps was simulated using a model of the detector geometry. The CMS particle flow algorithm, that was developed for the current detector which has much coarser granularity, was adapted to the new endcap geometry.

The performance measurements of CE prototype detector slices were carried out in various test beams. Figure 29 (left) displays the profile of energy deposits from a high-energy muon in the silicon modules of the CE prototype slice, together with the energy spectrum from the muon in a silicon sensor (right). This spectrum is used to calibrate the CE and demonstrates a good signal-to-noise ratio.

One performance benchmark is the resolution with which the invariant mass

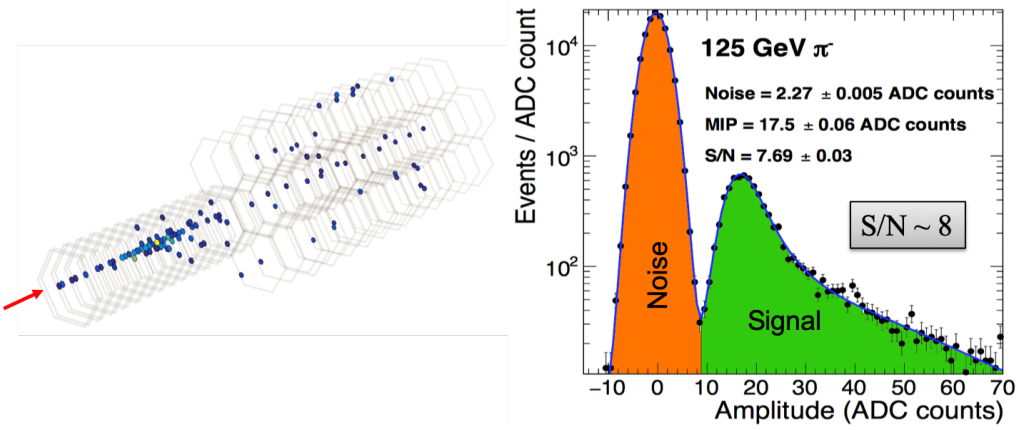

Figure 29. Left: display of a high-energy muon in the CMS CE prototype detector in a beam test [59]. Right: spectrum of energy deposits from the muon in the silicon modules.

of a photon pair can be reconstructed. This is relevant for identifying events with $H \to \gamma\gamma$ decays. The better the resolution, the more efficiently the Higgs boson mass peak can be separated from the continuum diphoton background. If both photons have $p_T > 40\,\text{GeV}$, are detected in the endcap calorimeter, and neither converts to an electron-positron pair in the tracker, the mass resolution is 1.4% of the Higgs mass, or 1.8 GeV. For comparison, the mass resolution for a pair of unconverted photons in the barrel calorimeter with an average of 200 pileup events is expected to be 1.9 GeV without radiation damage and 2.8 GeV after 3000 fb^{-1} [59].

Energy from particles emerging from all the interactions is deposited in the calorimeters and adds to the reconstructed energies of particles from the primary interaction. The high granularity of the endcap calorimeter allows the reconstruction to correct for this additional energy and limit the increase in resolution to about 20%. The additional energy from pileup interactions can also be clustered into noise jets. The rate of such noise jets is estimated using simulations and increase the number of reconstructed jets with $p_T > 30$ GeV by about 14% in the endcap calorimeter and 13% in the barrel calorimeter.

As explained in Section 3.5, signal arrival time information represents a novel and powerful means to suppress signals from pileup interactions. The CMS endcap calorimeter will exploit the fast response of the silicon sensors to provide a time stamp for signals with a resolution of about 30 ps as a completely new piece of information compared to the current CMS calorimeter. Figure 30 demonstrates the reduction in occupancy that is possible by filtering out the signals that are consistent with the primary interaction within a 90 ps window.

4.2. Physics Object Performance

The goal of the upgrade is to be able to reconstruct all the standard physics analysis objects with high efficiency, low fake rate (false positives mimicking the signal signature), and high resolution under the much harsher pileup conditions than at

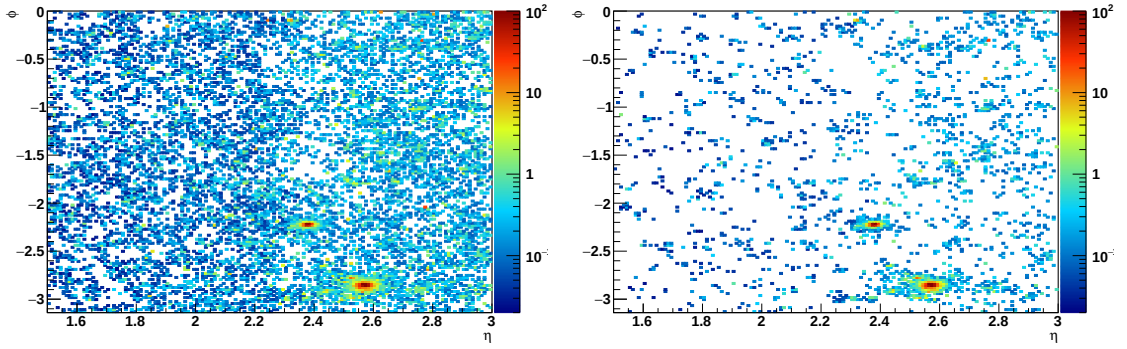

Figure 30. CMS endcap calorimeter cells with more than 12 fC of signal projected to the front face of the endcap calorimeter for a simulated Higgs decay to two photons [59] accompanied by a VBF jet. The color encodes the amount of energy in each cell. The left plot shows all cells and the right plot shows cells with timing consistent with the primary interaction to within 90 ps. A photon shower and VBF jet are visible over the pileup interactions.

the LHC. For precision measurements and observations of very rare processes, the minimum requirement is to maintain current performance for all physics objects. This goal requires excellence in every corner of the detectors and corner of the kinematic phase space.

4.2.1. Leptons and Photons In order to identify an electron (or a positron), the reconstruction algorithm searches for a compact cluster of energy almost entirely contained in the calorimeter with a matching track in the tracker. The electron reconstruction efficiency of the ATLAS detector is presented as a function of electron momentum in Fig. 31 (left) in the forward region showing the extended electron reconstruction and identification capabilities of the ITk.

A photon is identified as a compact cluster of energy almost entirely contained in the calorimeter without a matching track in the tracker or as an electron-positron pair in the tracker produced by a photon conversion. The photon reconstruction efficiency in the CMS detector is presented in Fig. 31 (right). It shows that the HL-LHC detector is expected to outperform the Run 2 detector.

High-energy muons are the only known charged particles which can penetrate the entire detector. This makes them easy to identify as tracks from high momentum charged particles in the tracking detectors of the muon systems, which are the outermost sub-systems of the detectors. Their reconstruction is of varying complexity, in the simplest case only involving the tracks in the muon system. For better identification and for association with a primary vertex these are matched to tracks in the trackers.

The momentum, p_{T}, of muons is measured from the radius of curvature of the track in the magnetic field in the detector. The resolution for muons as a function of their p_{T} is presented in Fig. 32 (left) for the ATLAS detector. The plot shows the fractional resolution of $1/p_{\mathrm{T}}$ because the distribution of the measurements of $1/p_{\mathrm{T}}$ for particles of a fixed momentum is approximately Gaussian and the resolution

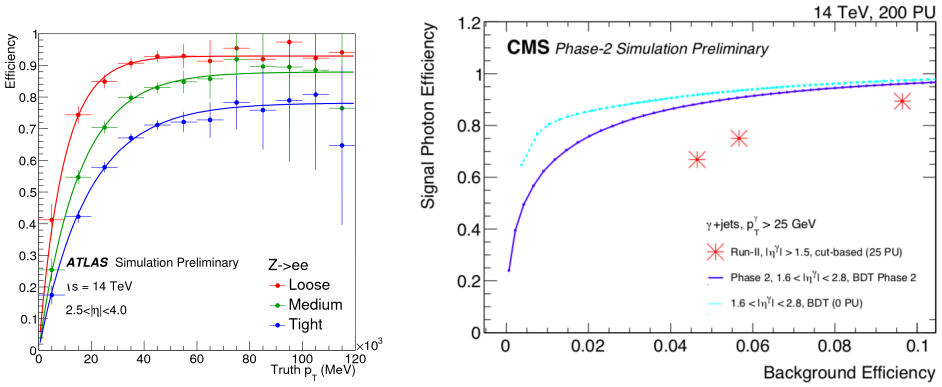

Figure 31. Left: electron reconstruction efficiency in the forward region of the ATLAS detector. The three differently colored lines represent the performance of algorithms that select electron samples with different purity [82]. Right: photon signal efficiency versus background efficiency for the CMS detector. The background efficiency measures the probability with which background signals are misidentified as photons. The Run 2 performance is shown as red stars, the expected performance at the HL-LHC is shown as a dark blue line, and in the ideal case of no pileup as a cyan line [83].

can easily be determined. The higher the momentum of the muon, the worse the resolution becomes because it is hard to measure the curvature of tracks that are almost straight. The expected performance of the new system for HL-LHC improves on the performance of the existing detector during Run 2.

Hadronic τ-decays leave a jet-like signature but with relatively few tracks, preferentially one or three, and a narrower cone than quark and gluon jets. These features can be exploited to identify the τ-decays. In order to reconstruct the τ-decays, tracks and energy deposits from pileup around the τ candidate have to be carefully removed. Figure 32 (right) presents the efficiency of this isolation procedure for CMS as a function of pileup density. It shows a dramatically improved performance when time of flight information is added to the algorithm, in particular for the nominal scenario with 30 ps time resolution.

4.2.2. Light Flavor Jets Quarks and gluons cannot exist as isolated free particles because the strong interaction between them grows as they separate from each other. A quark or a gluon that emerges from the primary interaction first undergoes a showering process in which secondary quarks and gluons are generated. This process is called fragmentation. The quarks then combine to form hadrons which are uncharged under the strong interaction. The latter process is called hadronisation.

The hadrons that originate from a given primary quark or gluon tend to all move in approximately the same direction and form a "jet" of particles which can be measured in the detectors. Charged hadrons deposit small amounts of energy through ionization along their path in the layers of the tracking detectors, and all hadrons deposit their energies in the calorimeters. These signals are combined into clusters or tracks of space-points to measure the energy and direction of the jet.

A powerful way of reconstructing jets is the particle flow algorithm used by

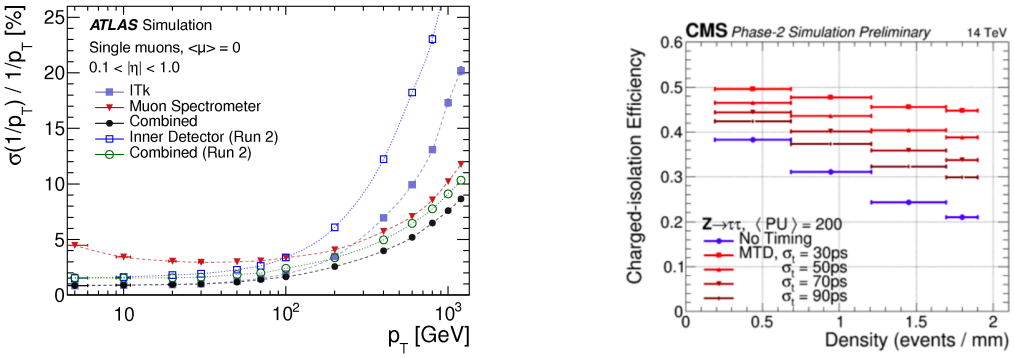

Figure 32. Left: muon momentum resolution for ATLAS as function of the transverse momentum, with the Run 2 tracker performance shown with open symbols and the expected ITk performance at HL-LHC with filled symbols [82]. Right: hadronically decaying τ isolation as a function of pileup density, without timing information in blue and with timing information used in red. The best performance is achieved for the nominal scenario with a time resolution of 30 ps [83].

both collaborations. It combines tracker and calorimeter information to reconstruct individual particles. These can then be used as inputs to jet clustering algorithms. In order to recover the energy of the original quark or gluon, a complicated multi-step calibration procedure is applied to mitigate the effects of the detector resolution and pileup.

The CMS Collaboration uses a procedure called PUPPI (PileUp Per Particle Identification) [84,85] for pileup mitigation. This technique corrects for pileup effects at the particle level, and is illustrated in Fig. 33 (left). Charged particles are assigned to the primary collision vertices from which their tracks in the tracking detector originate. It is therefore relatively straight forward to remove charged particles that do not belong to the collision of interest from the jet reconstruction. These techniques are called Charged Hadron Subtraction in CMS. Neutral particles do not leave such tracks and therefore cannot be uniquely associated with a primary collision vertex. However, the locations of neutral particles in the calorimeters tend to correlate with that of charged particles from the same collision. Therefore a score can be assigned to each neutral particle based on the charged particles in their vicinity that characterizes whether they are likely to originate from the collision of interest or not. Based on this score, neutral particles are removed from the jet reconstruction. The effectiveness of this procedure is demonstrated in Figure 33 (right). ATLAS uses the Jet-Vertex-Tagging algorithm which is a multivariate discriminant based on information from the tracker and calorimeter and per jet estimates the likelihood of each jet coming from the hard scatter interaction.

Pileup mitigation is an active field of research and increasingly involves more and more advanced machine learning techniques.

4.2.3. Heavy Flavor Jets Jets which contain heavy quarks (b, c) are very important for a wide range of measurements and travel a few millimeters before decaying.

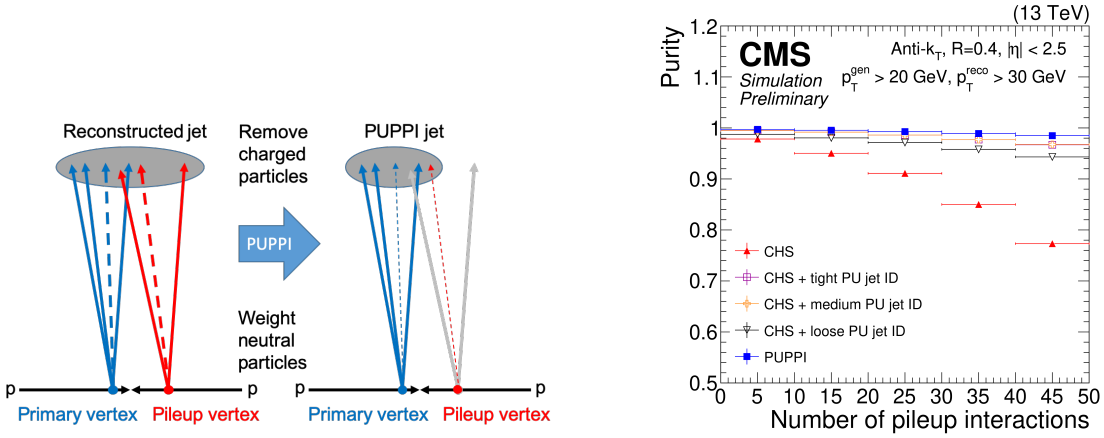

Figure 33. Left: principle of the PUPPI algorithm. Right: purity of jets as a function of the number of pileup interactions. The purity is defined as the fraction of jets that originates from the collision of interest. The PUPPI algorithm (blue squares) provides better pileup mitigation than charged hadron subtraction (CHS) which does not correct for neutral particles from pileup interactions [85].

Tracks from their decay products often do not exactly point back to the primary vertex of the collision and therefore it is possible to reconstruct a secondary decay vertex within the jet cone.

State-of-the-art heavy-flavor jet algorithms are based on information about these displaced tracks and secondary vertices used as input into machine learning algorithms which are trained to distinguish the heavy-flavor jets from light quark (u, d, s) jets and gluon jets. Figure 34 (left) shows the rejection factor for light quark jets versus the efficiency of reconstructing a b jet for ATLAS. The overall HL-LHC performance in the tracking volume before the ITk upgrade is represented by the orange dotted line and shows for the same b jet efficiency an improvement with respect to Run 2 (green crosses) in light jet rejection by a factor of 5, despite the harsher pileup conditions. Figure 34 (right) presents the b jet identification efficiency for CMS in two pseudorapidity regions (central and forward) as a function of the pileup density, demonstrating how the inclusion of the fast timing technology (MTD) dramatically improves the performance and pileup stability of heavy flavor tagging.

Different reconstruction algorithms are required to reconstruct jets produced by particles with significant transverse momentum. Such boosted algorithms are expected to become more widely used at the HL-LHC. Most of these so-called "sub-structure techniques" implement advanced machine learning and artificial intelligence algorithms.

4.2.4. Missing Transverse Momentum In order to reconstruct particles which do not interact with the detector, such as neutrinos or any potential undetectable new physics objects, an observable called missing transverse momentum is constructed. It is defined as the negative vector sum of the momenta of all reconstructed objects, projected into the transverse plane of the detector. This is the most complex

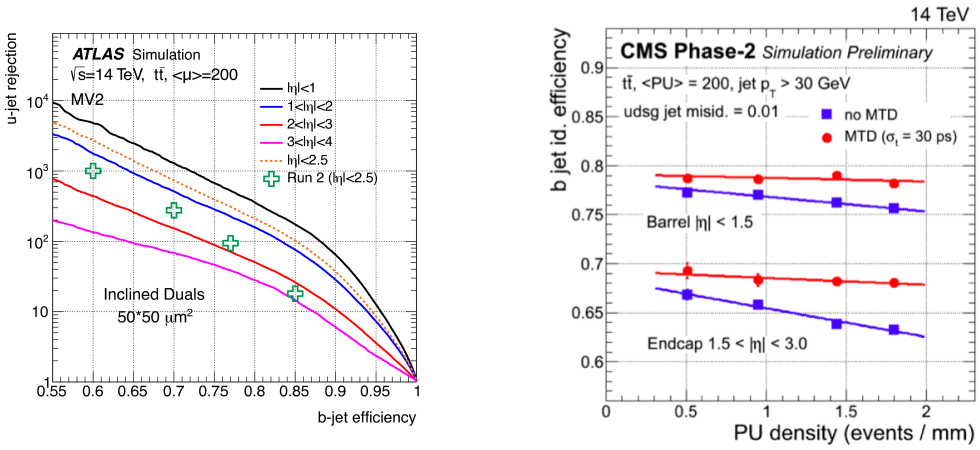

Figure 34. Left: rejection factor for light quark jets vs. b jet reconstruction efficiency for various parts of the ATLAS ITk (solid lines), compared to the Run 2 performance (green crosses). The overall HL-LHC performance in the same tracking volume is represented by the orange dotted line [82]. Right: CMS b jet reconstruction efficiency as a function of pileup density for central and forward b jets, with (red) and without (blue) the MTD timing detector, illustrating the gain through the timing measurement [65].

observable because it consists potentially of all physics objects described above. Therefore, any resolution effects and imperfections of the pileup mitigation will directly impact the missing transverse momentum resolution. After accounting for all the hard scatter objects in the event, an additional term is added called "the soft term". This accounts for all the particle activity with low momentum which may have happened at the hard scatter vertex, but was not associated with any object (especially jets). This soft term is usually calculated from tracks in the inner detector which can be uniquely associated with the hard scatter vertex. It is also very sensitive to pileup and therefore the missing transverse momentum performance is expected to worsen at the HL-LHC.

For SM processes without any neutrinos, the missing transverse momentum should be zero, which allows the above mentioned detector resolution effects to be estimated. For CMS, for example, the Run 2 resolution is about 10 GeV, whereas at the HL-LHC it is expected to increase to approximately 25 GeV [83].

4.3. Challenges in Reconstruction Software & Computing

In Run 2 of the LHC, the ATLAS and CMS experiments each collected approximately 150 fb^{-1} of physics data, which is only approximately 5% of the expected data from the HL-LHC. Processing and storing this data set already requires significant computational resources. The experiments also need to produce simulated samples, in which the physics and detector response are modeled by computer programs. As an example, we provide approximate numbers for the ATLAS experiment in regards to computing. The total Run 2 data set for ATLAS includes $\sim$ 50 billion data events and $\sim$ 20 billion simulated events. This requires

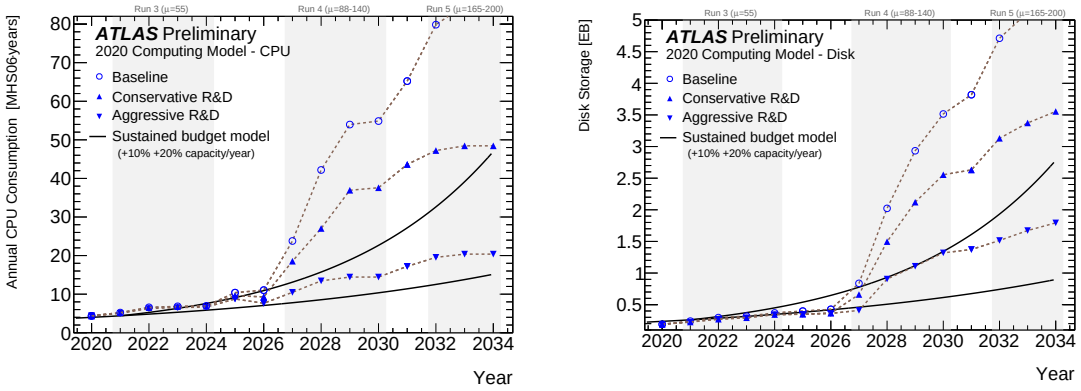

Figure 35. Projections from the ATLAS experiment for the amount of computational power, CPU, (left) and disk storage space (right) requirements in the years leading up to the HL-LHC. The projections (blue) are shown for a range of assumptions in the computing model in which certain key components have either been sped up or the amount of storage required has been reduced. The black curves indicate the expected available resources. From Ref [90].

200 PB of disk storage space and on average 4710 kHS06 (HS06 [86] is the HEPiX benchmark central processing unit (CPU) to allow comparisons between different architectures.) of CPU per year.

At the HL-LHC, computing will become significantly more challenging [87–89]. Due to the increase in luminosity, upgraded trigger systems, and the addition of new detectors with more channels, the total complexity (i.e. volume of information that needs to be processed) for each event is expected to increase by more than an order of magnitude and hence the computing resources required will increase significantly. The approximately 50 billion events expected from the HL-LHC each year for each experiment will require the generation of some 200 billion simulated events to fully exploit the physics potential. In addition, improvements to networking will be needed to ensure that the data is accessible worldwide. Figure 35 shows the computing resources which the ATLAS experiment estimates are needed each year. The most recent estimates for the required resources for different scenarios of computing models are shown in blue and can be compared to the expected available resources under current budgets. A large increase in the required resources in both CPU and disk space will be needed during the HL-LHC, which, depending on the scenario, exceed the expected resources by factors of up to three. In the baseline model, the largest fraction of CPU will be spent on the generation of the events for different physics process, the precise simulation using Geant4 and the preparation of the formats for physics analysis. In the baseline model, more than 70% of the disk space would be used to store the simulation samples.

Historically, the LHC experiments have profited from Moore's Law [91], which meant they were able to buy significantly more computing resources each year, while the budgets themselves remained flat. However, over the past decade the clock speed of processors has not increased, due to limits imposed by the power density [92]. This means that gains in processing capability have instead come from increasing

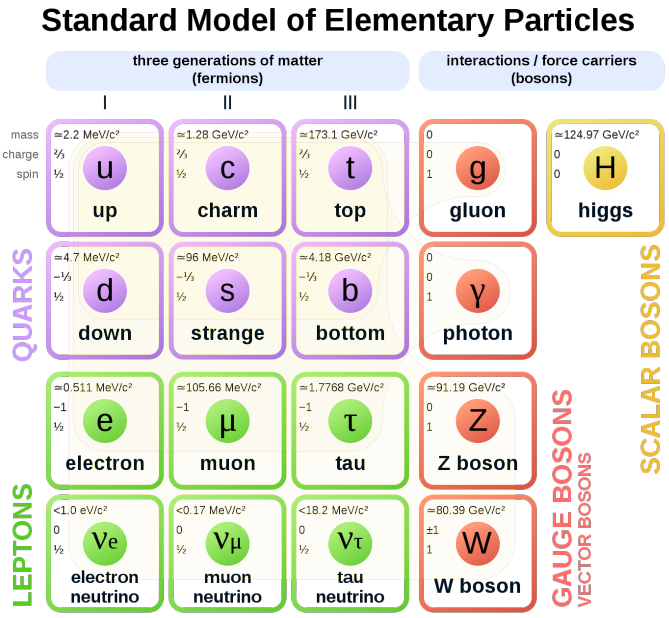

Figure 36. The elementary particles in the SM of particle physics. Image reproduced from Ref. [93]. The quarks are shown in purple, the leptons in green, the gauge bosons in orange and the Higgs boson in yellow. For the fermions, the generation increases by columns in the table.

the number of cores per CPU. In addition, a wide range of processing architectures have become available, ranging from many-core architectures to graphical processing units (GPUs) and field-programmable gate arrays (FPGAs). However, the original code used by ATLAS and CMS was developed more than a decade ago, which means that it was not designed with such computing architectures in mind. ATLAS [87] and CMS [89] are therefore both currently engaged in extensive R&D campaigns to re-engineer the code to support heterogeneous architectures. The success of these R&D programs is critical to fully exploit the physics potential of the HL-LHC.

5. Physics Prospects

5.1. The Standard Model of Particle Physics

The SM of particle physics is a theoretical model that describes all known elementary particles and their interactions except for gravity. It is similar to the periodic table which describes the chemical elements. It took more than a century to identify and discover all the SM particles. The first particle found was the electron, which was discovered by J.J. Thomson in 1897, and the final particle was the Higgs boson, which was discovered at CERN by the ATLAS and CMS Collaborations in 2012 [25, 26].

The particle content of the SM is summarized in Figure 36. Each charged particle has an antimatter partner with identical properties except for opposite charge. The particles of the SM fall into two main categories, depending on whether their intrinsic angular momentum, also called spin, is integer or half-integer.

Matter (and antimatter) consists of quarks and leptons, which are collectively referred to as fermions. Fermions have half-integer spin. There are six quarks: up, down, charm, strange, top, bottom. There are also six leptons: the electron, muon and tau (usually written as e, μ, and τ) and their respective neutrinos: the electron-neutrino, the muon-neutrino, and the tau-neutrino. The fermions are grouped into generations or families, which means that there are two more massive, but otherwise identical copies of each of the lightest fermions that make up almost all everyday matter (These are the up and down quarks as well as the electron and the electron neutrino.).

The particles with integer spin are called bosons and they mediate the interactions between particles. The photon is the carrier of the electromagnetic force, the gluon is the carrier of the strong force, and the W and Z bosons (or weak vector bosons) are the carriers of the weak force. At high energies, electroweak symmetry is restored and the electromagnetic and weak forces unify and become a single force.

The Higgs boson plays a special role. It breaks electroweak symmetry and provides a description of massive elementary particles in the theoretical framework of the SM. The masses of elementary particles are generated by their couplings to the Higgs boson. The higher the mass of the particle, the stronger the coupling between the particle and the Higgs boson. This means that the top quark has the strongest coupling to the Higgs boson. The Higgs boson also prevents the cross-section for vector boson scattering from violating unitarity (Sec. 5.2.4). Since the Higgs boson has to have very specific properties to achieve this, all of its properties are completely defined by the SM, except its mass, which has to be measured. The discovery of the Higgs boson in 2012 by the ATLAS and CMS Collaborations is a major achievement for the field [25, 26]. Projections for Higgs boson physics at the HL-LHC will be discussed in Section 5.2.

The SM provides an excellent description of most observed phenomena and has demonstrated itself to be very robust in predicting experimental results. However, there are certain phenomena that remain unexplained and the SM is not thought to be a complete theory of the fundamental interactions. Key questions which remain unanswered include the particle nature of dark matter, the matter-antimatter asymmetry in the universe and the origin of the three generations of fermions. These may require physics beyond the SM.

The measured mass of the Higgs boson of 125 GeV shines a new spot light on a theoretical challenge known as the hierarchy problem [94–97]. This problem originates from a hierarchy of energy scales. If we wanted to compute the mass of the Higgs boson in the SM framework we would have to add up the contributions from each interaction that the Higgs boson can participate in. These contributions can be positive and negative. If we require that the SM is valid at all energies up to the Planck scale of 10^{28} eV, the magnitude of each of these contributions become extremely large, similar to the Planck scale. It would be a tremendous coincidence if they all added up to a value as small as 125 GeV. It seems much more plausible that there is some physical reason for this cancellation that removes the need for

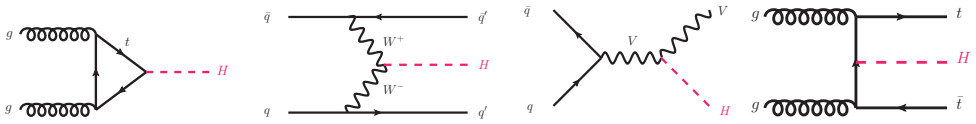

Figure 37. Selected Feynman diagrams for production modes of the Higgs boson production. From left to right: ggH, VBF, VH, and ttH production.

this coincidence, such as a new symmetry. New symmetries would likely give rise to new gauge bosons that appear as resonances in invariant mass spectra. Many of the solutions to the hierarchy problem propose the existence of colored "top-partners" to cancel the largest contributions to the Higgs mass, which originate from the heaviest known fundamental particle, the top quark. Possible "top-partners" are the top squarks in supersymmetric models [98–103] and heavy quarks, so-called vector-like quarks [104–108], that appear in models in which the Higgs boson is a composite particle [109–113]. If these new particles have masses around a TeV, they would effectively resolve the hierarchy problem, which provides a strong motivation that new physics could be within reach of the HL-LHC.

Over the past decade, the LHC has been a stunning success. Together ATLAS and CMS have published almost two thousand papers, on topics ranging from precise measurements of SM processes to searches that test an impressive array of hypothesized particles and interactions. However, no signs for physics beyond the SM have been observed. The HL-LHC will substantially increase the sensitivity to various scenarios of new physics. We will discuss searches for such physics beyond the SM at the HL-LHC in Section 5.3.

5.2. The Higgs Boson

5.2.1. Higgs Production and Decay In the proton-proton collisions at the LHC, there are four main production mechanisms for the Higgs boson, as illustrated in Fig. 37 via the Feynman diagrams (Feynman diagrams provide a visualisation of elementary particle interactions and a set of rules used to calculate the cross sections.). Other production processes are possible but, since they all involve the coupling of the Higgs boson to lighter fermions, their cross sections are significantly smaller. A recent overview of the Higgs boson production and decay modes is provided in Ref. [114].

The dominant production process for the Higgs boson is gluon fusion (ggH: $gg \to H$). The Higgs boson does not couple directly to the massless gluons. Instead the process proceeds via an intermediate loop of virtual top quarks. The cross section for this process is large at the LHC because there are many gluons inside the colliding protons, the top quark couples strongly to the Higgs boson, and the only particle produced is the Higgs boson. The second most frequent production process is vector boson fusion (VBF: $q\bar{q}' \to H + q\bar{q}'$). The cross section for this process is smaller than for ggH by about an order of magnitude because the antiquarks inside the proton carry much less momentum than the quarks. The cross section for

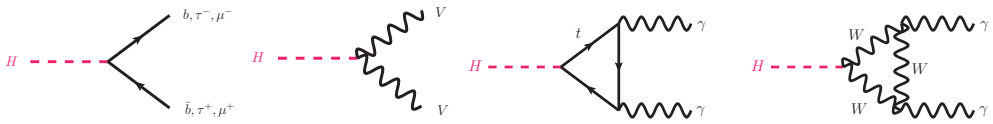

Figure 38. Example Feynman diagrams for Higgs boson decays to fermions ($H \to b\bar{b}$, $\tau^+\tau^-$ or $\mu^+\mu^-$ - first diagram), to vector bosons ($H \to VV$, where V = W or Z - second diagram), and to photons ($H \to \gamma\gamma$ - third and fourth diagrams).

the third most common process, associated production with a vector boson (VH: $q\bar{q}' \to H + V$, where V = W or Z) is further suppressed by the need for the initial particles to have enough energy to produce a massive gauge boson in the final state in addition to the Higgs boson. Finally, there is associated production with top quarks (ttH: $gg \to t\bar{t}H$). Its cross section is relatively small because of the need to produce two additional massive top quarks in the final state. Double Higgs production (HH) also occurs, but the rate is about thousand times smaller than single Higgs boson production.

The HL-LHC will be a Higgs boson factory, and will produce a total of about 170 million Higgs bosons. Of these, 13 million will be from VBF, 8 million from VH, 1.8 million from ttH production, and 120,000 from Higgs boson pair production. These Higgs bosons will decay through a range of different signatures. The most sensitive Higgs boson decay channels are $H \to \gamma\gamma$, ZZ^*, WW^*, $\tau^+\tau^-$, and $b\bar{b}$. The respective diagrams are shown in Fig. 38. Higgs production is still a relatively rare process at the LHC and as large as these numbers are, they pale in comparison to the number of W bosons that will be produced at the HL-LHC (60 billion), the number of Z bosons (6 billion), or the number of top quarks (3 billion). Thus the challenge is to find the Higgs bosons within a large background of other particles.

All detector subsystems play an important role in the detection of Higgs bosons. For example, detecting the decay of the Higgs to b quarks needs good jet energy resolution from the calorimeters as well as efficient identification of b jets from the pixel detector. For the $\tau\tau$ channel, the τ-leptons are reconstructed using both the tracking detectors and the calorimeters. As few tracks are produced in τ-lepton decays, the efficiency of the tracking detectors is particularly important. For the $\gamma\gamma$ channel, the energy resolution of the electromagnetic calorimeter is vital and the efficient identification of photons is important.

5.2.2. Higgs Couplings A key characteristic of the Higgs boson is that it interacts with other particles with a coupling strength proportional to their masses. Thus the Higgs boson couples most strongly to the top quark. The experimental verification of this characteristic was necessary to establishing that the observed boson actually is the predicted Higgs boson. Precision measurements of the couplings of the Higgs boson to the known SM particles will provide key information about the validity of the Higgs mechanism as formulated in the SM.

The Higgs couplings manifest themselves in the rates of the production modes and decays involving various SM particles. Given the large number of Higgs bosons

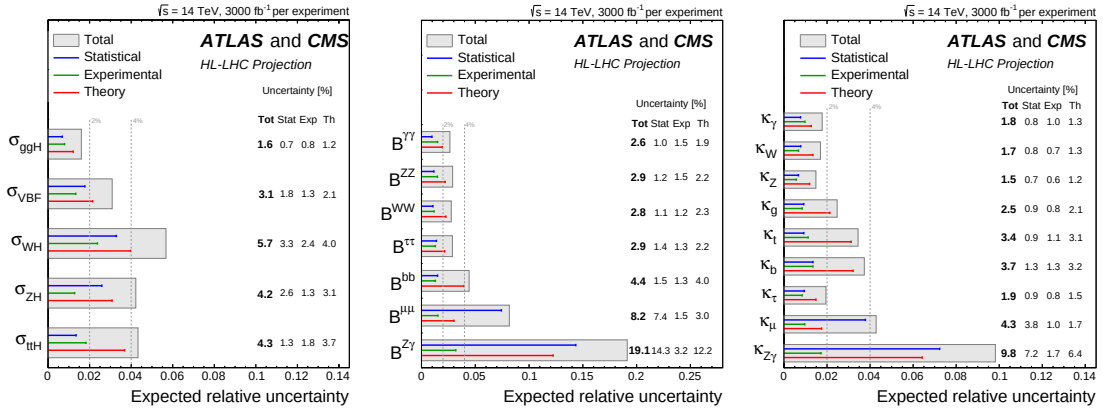

Figure 39. Expected uncertainties for measurements of the Higgs coupling parameters: (left) production cross sections (σ), (middle) branching fractions (B), and (right) coupling modifier parameters (κ). Most of the couplings will be measured at the HL-LHC with precisions below 5% of their expected values [115].

produced at the LHC, precise measurements of these rates in a variety of production and decay modes will be possible. Any deviation from SM expectations may be a sign of new physics. Models with new physics with a different structure in the underlying theory, e.g., those with additional Higgs bosons or composite Higgs bosons or with new states which are too heavy for direct detection, can alter the predicted couplings. Projections of the expected precision of the measurements, for the full HL-LHC data set, based on current results from LHC data, have been performed by both the ATLAS and CMS Collaborations [115]. The studies have been carried out for the main production modes (ggH, VBF, VH, and ttH). The Higgs decay modes considered are $H \to \gamma\gamma$, ZZ^*, WW^*, $\tau^+\tau^-$, bb, $\mu^+\mu^-$, and $Z\gamma$. The experiments measure the cross section σ (not to be confused with the standard deviation, also designated as σ) for each production process and the fraction of Higgs bosons, B, that decay to a particular final state. Since production and decay modes can involve the same particles, these are not independent measurements. This connection is implemented by introducing coupling modifier parameters κ_i which multiply the coupling of the Higgs boson to particle i. The κ's are normalized so that $\kappa_i = 1$ for all i corresponds to the SM predictions. Current measurements of the κ's are all consistent with the SM to a precision of approximately 8–20% [116, 117] (with the exception of $\kappa_\mu > 50\%$). Figure 39 shows the expected relative uncertainties achievable at the HL-LHC, split into three components (statistical, experimental, and theoretical) for these observables. At the HL-LHC, the κ's will be measured at the few percent level. Theoretical uncertainties dominate the final result. A measurement of the couplings with a precision of 5% (sub-1%) will probe the existence of new particles with mass of about 1 TeV (10 TeV). Precision measurements of the Higgs couplings are an important goal of the HL-LHC program and continue to play a pivotal role in probing the scale of new physics.

5.2.3. Higgs Self-coupling A key SM prediction for the Higgs boson is that it couples to itself and thereby is responsible for its own mass. This can be tested

Figure 40. Diagrams showing different production mechanisms for events containing two Higgs bosons (HH production). (Left) The diagram sensitive to the self-coupling of the Higgs boson, due to the vertex of three Higgs bosons. (Right) Production of two Higgs bosons from a top quark loop.

by measuring events containing not one, but two Higgs bosons, referred to as HH production, or through precise measurements of single Higgs production. The self-coupling of the Higgs boson has not yet been probed at the LHC because the cross section for HH production is tiny due to a phenomenon in quantum mechanics know as interference, which occurs when both the initial and final state particles of two different processes are identical. There is large destructive interference between HH production via self-coupling (Fig. 40, left) and another similar process in which two Higgs bosons are separately produced from a top quark loop (Fig. 40, right), which is a SM background. However, the large data set and improved detectors of the HL-LHC are expected to provide sufficient sensitivity such that evidence for, if not discovery of, HH production can be obtained.

There are many possible final states dictated by the combination of the decays of each individual Higgs boson in events containing two Higgs bosons. However, because the cross section for HH production is small and the branching ratio of the Higgs boson to b quarks is large, typically one of the two Higgs bosons is required to decay to b quarks. The two channels that are currently predicted to be the most sensitive have the second Higgs boson decaying to either a pair of photons ($b\bar{b}\gamma\gamma$) or to a pair of τ-leptons ($b\bar{b}\tau\tau$). Figure 41 illustrates how HH production using the $b\bar{b}\gamma\gamma$ channel might be observed by the CMS experiment. The low event rate will make this a very challenging channel to observe at the HL-LHC.

Current projections using all decay channels and combining the results from ATLAS and CMS would result in an expected significance of almost 3σ [115], which is very encouraging, but falls short of the 5σ threshold required for discovery (The significance is typically quoted as σ, or a number of standard deviations of the normal distribution around the expected number of background events. In high-energy particle physics a significance of 3σ is referred to as evidence, while 5σ is referred to as an observation, corresponding to the probability of a statistical fluctuation from the background of less than 1 in a million.). Results with little sensitivity are quoted instead in terms of an upper limit. This limit is the largest cross section of the process that the measurement could be sensitive to, i.e. if there was a contribution from new physics that increased the cross section that much, it would have been observed. The current upper limit on HH production from the ATLAS experiment [119] is 7 times larger than the SM prediction (An upper limit

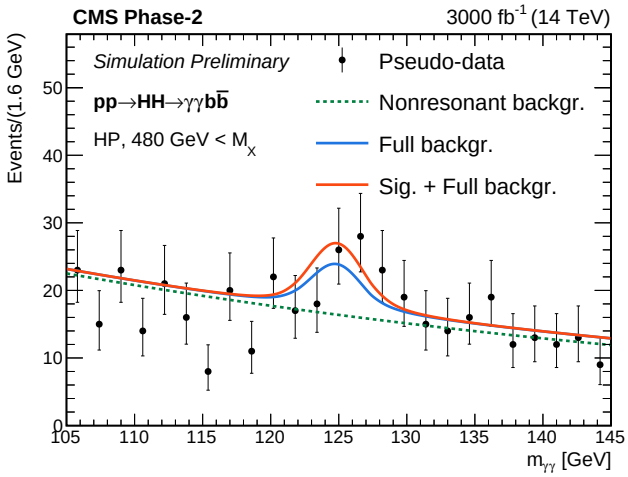

Figure 41. Illustration of the expected photon pair mass distribution from the CMS HH $\rightarrow$ $b\bar{b}\gamma\gamma$ analysis, which probes the self-coupling of the Higgs boson. The contribution from the decays of the Higgs boson is visible in the peak at 125 GeV. The background is shown in blue and includes contributions from single Higgs production. The combination of the signal and background is indicated in red. From Ref. [118].

reaching the SM prediction has a significance of close to 2σ.). The 3σ evidence for HH production expected from the HL-LHC can be translated into the following constraint on the parameter κ_λ: $0.4 \leq \kappa_\lambda \leq 1.7$ [115], which is a scale factor for the strength of the coupling of the Higgs boson to itself.

5.2.4. Vector Boson Scattering Interactions of the mediators of the weak force - the massive $W^{\pm}$ and Z bosons - with the Higgs boson lie at the heart of the SM. The unitarity principle requires that the probability of each observed process occurring cannot exceed 100%. Theoretical calculations show that the scattering of two longitudinally polarized vector bosons (VBS) would violate this principle at the LHC in the absence of the Higgs boson [120]. The addition of the Higgs boson introduces additional processes, which, via destructive interference, bring the cross section for vector boson scattering into compliance with unitarity. Therefore, despite the discovery of the Higgs boson, the observation and cross section measurement of VBS provides an important test that the Higgs boson is responsible for the mechanism of electroweak symmetry breaking. Observation of this rare but crucial process is hence one of the key goals of the HL-LHC program.

Figure 42 (left) provides some of the Feynman diagrams describing VBS [121]. Experimentally, the VBS topology is characterized by a large opening angle between the two highly energetic jets in the event. Therefore the central detector has to be completely empty except for the decay products of the vector bosons themselves. This requirement puts stringent criteria on the quality of pileup mitigation because any additional activity from pileup interactions would produce additional particles in the gap. Additionally, the highly energetic VBS jets typically point into the forward and backward regions of the detector, which requires superb pileup mitigation up to the highest pseudorapidities. Therefore, the ability to clearly reconstruct this process was one of the main motivations for extending the ATLAS and CMS trackers

to $|\eta| = 4.0$ to increase the acceptance of VBS signal jets and for implementing fast timing technology upgrades such as the HGTD and the MTD to reject pileup.

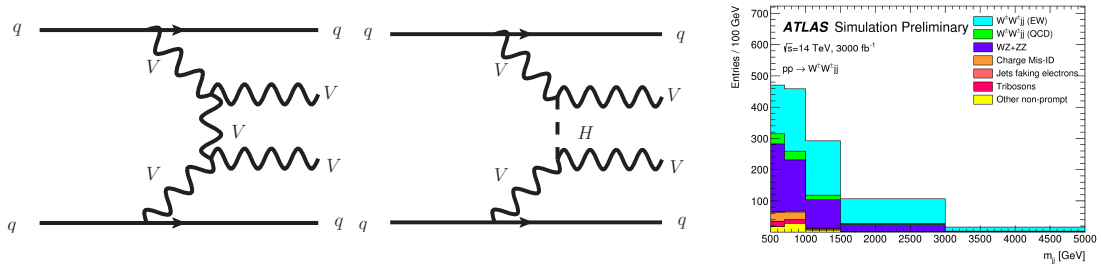

Figure 42. Left: example Feynman diagrams of vector boson scattering in the presence of two jets, involving vector boson and Higgs boson exchange [121]. Right: distribution of the invariant mass of the two most energetic jets in the event, demonstrating the high sensitivity of this analysis to the process of vector boson scattering (labeled as WWjj(EW)) [121].

The Run 2 analyses established a limit in the search for the scattering of two longitudinally polarized W bosons of four times the SM cross section [122]. At the HL-LHC, the significance for this process is expected to reach three sigma for a combined ATLAS and CMS analysis, establishing this crucial process and providing a strong constraint on the presence of new physics in processes with heavy vector bosons. The large HL-LHC data set will not only allow for the measurement of the probability of the VBS process but also its dependence on various observables (such as the invariant mass of the two most energetic jets in the interaction). This additional information will increase the sensitivity to effects of potential new physics phenomena [123]. Such dependence is illustrated in Figure 42 (right) [121].

5.3. Searching for New Particles beyond the Standard Model

5.3.1. Resonance Searches Direct searches for heavy new resonances predicted by various models will be carried out at the HL-LHC. The discovery of a new resonance would provide evidence for new physics and may open up exciting pathways for distinguishing between the new physics models, while a null result may indicate the need for new paradigms.

Resonances that decay into e^+e^- or $\mu^+\mu^-$ pairs arise in many models, including those with additional symmetries, such as grand unified theories (GUTs). Such particles are called Z′ bosons because of their similarity with the SM Z boson. They are efficiently triggered on and can be detected in the dilepton invariant mass spectrum with excellent resolution. A popular standard candle for experiments is a SM-like Z′ boson, which has similar properties as the SM Z boson, except for the mass. Such SM-like Z′ bosons can be discovered at the HL-LHC for masses up to about 6 TeV.

Massive particles that have properties similar to the SM W boson could also exist. They are called W′ bosons. Standard Model-like W′ bosons can be discovered up to masses of 7.5 TeV at the HL-LHC.

A class of models of new physics that address the hierarchy problem hypothesizes that there are additional spatial dimensions [124, 125]. In three-dimensional space, the strength of an interaction falls proportional to 1/distance squared. If gravity propagated in extra dimensions, it would fall off much faster with distance, which would explain why it appears so weak to us. Such extra dimensions have to be finite in size in order not to affect the long range behavior of gravity. Therefore, particles that propagate in the extra dimensions can only have discrete momentum values, similar to a particle constrained to a finite potential well. These excitations manifest themselves as resonances of different masses and are called Kaluza-Klein (KK) states. As an example of such models, Randall-Sundrum models contain an extra dimension with a warped metric in which some particles can propagate, giving rise to Kaluza-Klein excitations [125]. For example, a gluon propagating in the extra dimension could have massive Kaluza-Klein excitations that decay to top-antitop quark pairs. Sensitivity studies indicate that such KK gluons could be discovered at the HL-LHC up to masses of 5.7 TeV. This excellent sensitivity mostly arises from expected improvements in the identification of high-momentum top quarks using specialized tagging methods. The top-tagging techniques benefit from the new trackers with improved momentum resolution and better two-track separation as they translate into efficient charged particle reconstruction within the core of highly Lorentz-boosted jets.

5.3.2. Supersymmetry Searches Supersymmetry (SUSY) is a symmetry between fermions and bosons. If nature is supersymmetric, there exists a boson superpartner for each fermion and vice versa. The partners of fermions are named with an "s" for "scalar" in front of the name of the fermion. Partners of bosons add the ending "-ino" to the name of the boson. The symbols of SUSY particles are constructed by placing a tilde on top of the symbol for their SM partner. For example, the partner of the electron would be called the selectron ($\tilde{e}$) and the partner of the W boson would be the wino ($\tilde{W}$). SUSY requires an extended Higgs sector which contains at least five Higgs particles. Two of these are charged and three are neutral. In most SUSY models, one of the neutral Higgs bosons has properties very similar to the SM Higgs boson. Their superpartners are collectively called higgsinos.

SUSY might be realised in nature in various ways and superpartners could be produced at colliders leading to many different possible signatures. The phenomenology is determined by a large number of parameters. However, the lightest supersymmetric particle (LSP) has to be stable or, at least, very long-lived in order to avoid a rate of proton decay in violation of observed limits. One therefore usually hypothesizes a conserved quantum number called R-parity. All superpartners then decay to SM particles plus a neutral LSP that escapes undetected, which leads to the characteristic feature of missing transverse momentum in events with superpartner production and decay.

If the masses of the superpartners are low enough, SUSY has the potential to resolve the hierarchy problem by providing a partner to the top quark, the stop ($\tilde{t}$), to cancel the contributions of the top quark to the Higgs boson mass. This is called

natural SUSY. SUSY may also provide gauge coupling unification and a dark matter candidate with the LSP.

Colored superpartners such as squarks ($\tilde{q}$) and gluinos ($\tilde{g}$) are produced via the strong interaction and have the highest cross sections. The superpartners of the Higgs boson, photon, Z, and W bosons are the spin-1/2 higgsino, photino, zino, and wino, which mix to form four neutral particles called neutralinos ($\tilde{\chi}_1^0$, $\tilde{\chi}_2^0$, $\tilde{\chi}_3^0$, and $\tilde{\chi}_4^0$) and four charged particles called charginos ($\tilde{\chi}_1^+$, $\tilde{\chi}_1^-$, $\tilde{\chi}_2^+$, and $\tilde{\chi}_2^-$). They only couple through the electroweak interaction and their production rate is thus a few orders of magnitude lower than that of colored superpartners of the same mass value.

Many searches for superpartners have been carried out at the LHC and lower limits on the masses of these superpartners have been set, meaning that they should have been observed at the LHC if their masses were below these lower limits. The limits for strongly interacting superpartners, in particular, are on the order of 1 TeV or even higher. The large data sets expected from the HL-LHC will enable searches for electroweakly interacting superpartners and other SUSY signatures for which current limits are much weaker.

Search for Higgsinos: In scenarios of natural SUSY, the higgsinos may be the only low-mass superpartners (while the others have masses above the TeV scale). In this case, higgsinos are the dominant component of the lightest chargino and neutralino. The discovery of such higgsino-like charginos and neutralinos may be a crucial test of natural SUSY. The HL-LHC with its large luminosity will aid significantly in their search. The higgsino-like neutralinos are expected to be pair produced with each other (e.g., $\tilde{\chi}_2^0\tilde{\chi}_1^0$) or with charginos (e.g., $\tilde{\chi}_1^\pm\tilde{\chi}_2^0$). The $\tilde{\chi}_2^0$ decays promptly into $\tilde{\chi}_1^0$ through the weak interaction. The sensitivity reach for the signature with $\tilde{\chi}_2^0$ decaying to a low mass virtual Z boson in events with an additional jet from initial state radiation to enhance the sensitivity is shown in Fig. 43 and indicates a potential discovery of higgsino-like particles with masses up to 250 GeV, depending on the mass splitting between $\tilde{\chi}_2^0$ and $\tilde{\chi}_1^0$ [126]. The final state signature for this study contains two same-flavor, opposite-charge, low transverse momentum leptons (electrons or muons), one jet, and significant missing transverse momentum. It benefits from the excellent momentum resolutions of the new trackers and the upgraded calorimeters, including the timing detectors to reject the fake tracks from pileup.

Sleptons: The superpartners of the charged leptons, the sleptons ($\tilde{e}$, $\tilde{\mu}$, $\tilde{\tau}$), can also have sizeable production rates, in particular the $\tilde{\tau}$, the superpartner of the τ lepton. In SUSY scenarios in which the $\tilde{\tau}$ is more massive than the superpartners of electrons and muons, the challenge due to the small production cross section is alleviated by the large data set expected at the HL-LHC. With the current LHC data sets, the search sensitivity for $\tilde{\tau}$s is extremely limited (125 GeV) [127]. The HL-LHC provides an unprecedented opportunity to probe the direct production of $\tilde{\tau}$s, with the discovery contour for $\tilde{\tau}$ masses reaching up to 470 GeV, as shown in Fig. 44 [128].

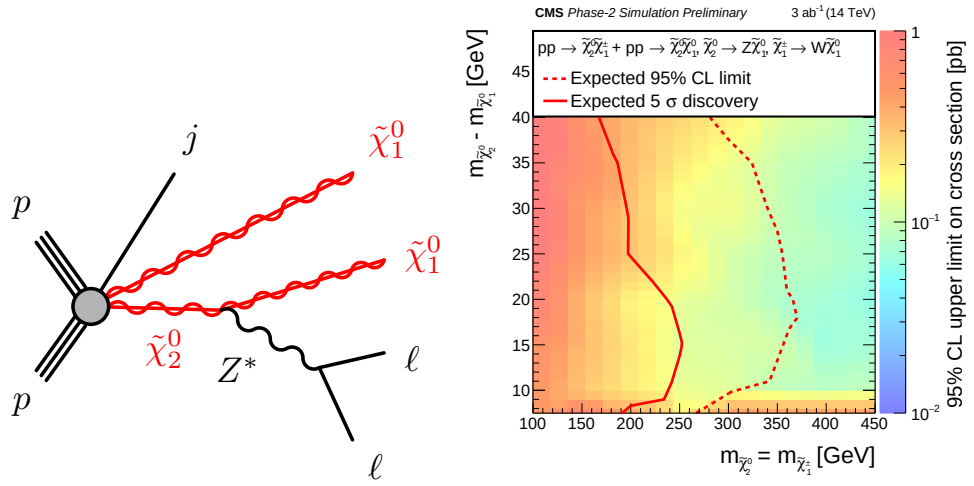

Figure 43. Higgsino-like neutralino pair production diagram (left); exclusion/discovery contours for combined $\tilde{\chi}_2^0\tilde{\chi}_1^0$ and $\tilde{\chi}_1^\pm\tilde{\chi}_2^0$ production (right). Results are presented for $\Delta M(\tilde{\chi}_2^0, \tilde{\chi}_1^0) > 7.5\,\text{GeV}$ [126].

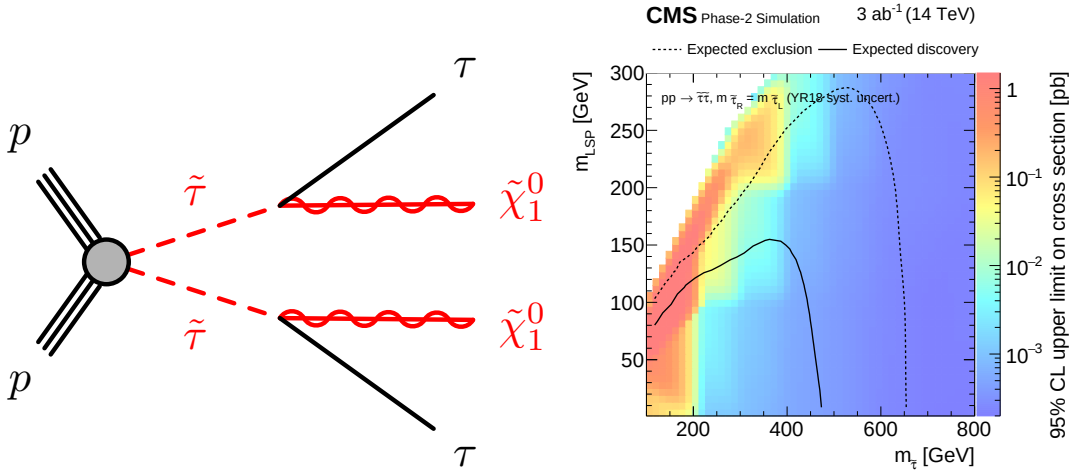

Figure 44. Pair production diagram for $\tilde{\tau}$ leptons (left); expected exclusion and discovery contours for $\tilde{\tau}$ pair production in the $m_{\tilde{\tau}}$, m_{LSP} mass plane (right) [128].

Long-lived Particles: Certain SUSY, as well as other models of new physics, can be probed by studying experimental signatures sensitive to new particles with long lifetimes (Here we focus on particles with lifetimes such that they are expected to decay within the detector.). See Ref. [129], for example, for a recent review. These new particles can either be charged or neutral. Searches for long-lived particles strongly rely on the detector and trigger performance and sophisticated reconstruction algorithms to identify them. These methods typically focus on two detector signatures: reconstructing the vertex to identify where the particle decayed, or identifying a well-reconstructed track which disappears at some point in the detector when the particle decays. The latter method is only applicable to searches for charged particles, while the former is only applicable to decays to charged particles. Such methods are sensitive to a wide-range of signatures of physics beyond the SM, including challenging scenarios in supersymmetry. One example

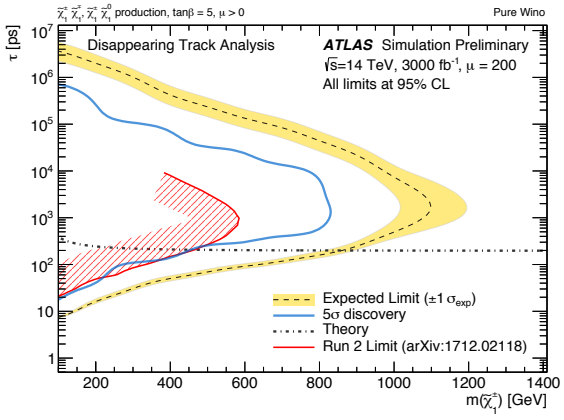

Figure 45. Current and expected results as a function of the particle mass and lifetime from the disappearing track analysis. The expected discovery range (blue solid curve) and the exclusion limit (black dashed curve) using the full HL-LHC data set are shown. The theory curve [132] is for a pure wino LSP scenario. The current limit from the ATLAS experiment is indicated in red. Shaded areas are used to indicate the uncertainty on the limits. From Refs. [133, 134].

would be anomaly-mediated SUSY scenarios [130, 131], in which the masses of the supersymmetric particles differ by only a small amount, resulting in a small amount of missing energy, and rendering traditional techniques challenging.

A disappearing track occurs when the long-lived charged particle is produced but its decay products are not detected. The decay products may not be detected either because they interact only very weakly, or because they have such low momenta that they cannot be reconstructed. These tracks are typically reconstructed with an additional pass of a track reconstruction algorithm, which takes as input those hits that have not already been used for tracks.

Figure 45 shows the expected sensitivity of the ATLAS experiment at the HL-LHC to such models. The results are shown as a function of the mass of the new particle (in this specific case the long-lived particle is the wino) and its lifetime. ATLAS would be sensitive to particles with masses and lifetimes to the left of the lines. The HL-LHC would extend the reach significantly beyond the current results from the ATLAS experiment based on the Run 2 data set at the LHC, which are shown in red, to the black dashed line with a yellow band.

The sensitivity of the disappearing track analysis is very sensitive to the performance of the pixel detector and the details of the track reconstruction algorithms. For example, additional pixel layers particularly at smaller radii can extend the sensitivity of the search, allowing shorter tracks to be probed. Another method to detect long-lived particles would be searches for displaced jets. The addition of timing detectors for the HL-LHC can be expected to open up new avenues with which to search for long-lived particles.

Dark Photons: In several models of new physics, a "dark" sector of fermions and gauge fields is introduced, which does not interact with SM particles. Here we describe the case of a SUSY Model that includes a dark sector. The gauge boson

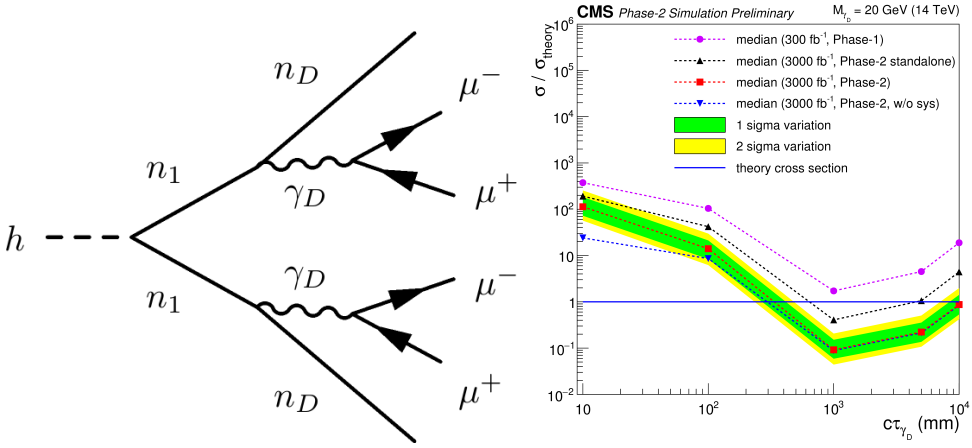

Figure 46. Left: Feynman diagram of the decay of the SM Higgs boson to a final state containing exactly four muons illustrating possible dark SUSY models. [135] Right: 95% CL upper limits on the production cross section divided by the theoretical cross section, $\sigma/\sigma_{\text{theory}}$, for a fixed mass of $M_{\gamma_D} = 20\,\text{GeV}$ as a function of the dark photon decay length. The expected limits set by the LHC data set of $300\,\text{fb}^{-1}$ are shown by the violet line, the expected limits from the HL-LHC are shown in red (nominal expected result with the ±1 (green) and ±2 (yellow) standard deviation bands) and in black (result with degraded muon reconstruction efficiency). The theoretical dark SUSY cross section for 14 TeV is shown as a solid line. Whenever the projected limit is below the theoretical cross section calculation (i.e. $\sigma/\sigma_{\text{theory}} \leq 1$), the analysis has the potential to exclude that model or to establish an observation or discovery (i.e. in the $c\tau$ range of $\approx$300-10,000 mm for the nominal scenario) [136].

corresponding to the additional $\text{U}_D(1)$ symmetry is called the dark photon (γ_D), which can mix with the SM photon [135]. In such models, the dark photon couples to SM charged particles in the same way as the photon, except that the couplings are scaled by a parameter ϵ that depends inversely on the dark photon life time (τ). Dark photons can be detected in cascade decays of the SM Higgs boson that would first decay to a pair of the lightest neutralino (n_1). These neutralinos can, but are not required to be, the neutralinos within SUSY models. Each neutralino can decay further to a dark sector neutralino (n_D) and the dark photon, as illustrated in Fig. 46 (left). The dark photon subsequently decays into fermion-anti fermion pairs, in particular into muons and anti-muons in the scenario presented here.

The acceptance of the ATLAS and CMS detectors covers a range of 10 to 10,000 mm in the decay length ($c\tau$) of dark photons. The muon pairs can be reconstructed at a vertex which is highly displaced with respect to the primary interaction. For long decay lengths, only the upgraded outer muon systems of the ATLAS and CMS detectors will be able to detect and reconstruct such muons. Due to the event topology where muons originate from highly displaced vertices outside of the inner tracker, events with reconstructed muons from cosmic rays or the LHC beam halo have to be accounted for in addition to collision-related background processes.

Figure 46 (right) presents 95% confidence level (CL) upper limits on $\sigma/\sigma_{\text{theory}}$

as a function of decay length of the dark photons with an assumed mass of $M_{\gamma_D} = 20\,\text{GeV}$ over three orders of magnitude in $c\tau$ [136]. The expected limits of the HL-LHC analysis improve by an order of magnitude over the LHC data set [137] results and, for the first time, allow for a potential exclusion of the dark photon model if the decay length is longer than 30 cm.

5.3.3. Dark Matter Possibly the clearest experimental evidence that we currently have for physics beyond the Standard Model are the cosmological observations which indicate that approximately 85% of the matter in the universe is dark matter [27,28]. If this dark matter is made of particles, and depending on their mass and the nature of their interaction, dark matter could be discovered at the HL-LHC. Currently the origin and nature of dark matter are unsolved problems.

A wide range of models for dark matter, including SUSY, have been explored at the LHC and will be further probed at the HL-LHC. For example, if we assume that the dark matter was produced through low energy or thermal interactions with other SM particles in the early universe, dark matter particles would typically have masses in the range from a few keV to hundreds of TeV. Examples include the Weakly Interacting Massive Particles (WIMPs) [138], which have dominated dark matter searches for many years, and particles in a hidden dark sector, which only interact with the particles of the SM through very weak and indirect interactions [139]. In other models, dark matter is produced through more energetic collisions, resulting in ultra-light particles with masses well below an eV. This includes a hypothetical particle, known as the axion [140], which is a potential solution to a problem with the theory of quantum chromodynamics: the strong charge parity (CP) problem [141].

Colliders play a role complementary to experiments designed to search for dark matter. At the HL-LHC, searches for dark matter rely on direct production in proton-proton collisions, production in association with other SM particles, and production through the decays of SM particles, or other BSM states. In general, dark matter particles are, by their very nature, effectively invisible to traditional detection techniques, because they do not interact via the electromagnetic interaction. Instead, their presence is inferred from the other particles detected in the event and applying the conservation of energy to determine the missing transverse energy carried away by the dark matter particle.

Searches for dark matter at colliders are typically classified according to the SM particles detected alongside the dark matter. Searches for dark matter produced in association with a single high-momentum jet probe models in which the dark matter is produced through the exchange of a neutral mediating particle, mediator, that couples to the SM particles. Such monojet searches will be able to probe dark matter masses up to 800 GeV and mediator masses up to 2.5 TeV [142, 143].

Dark matter can also be searched for if it is produced with heavy-flavor quarks. In this case, the HL-LHC is expected to improve the sensitivity to masses of the mediator between the SM and the dark matter by a factor ranging from three to eight relative to current results. For example, a search focusing on a final state including four top quarks will be able to probe particles with masses between 200 GeV and

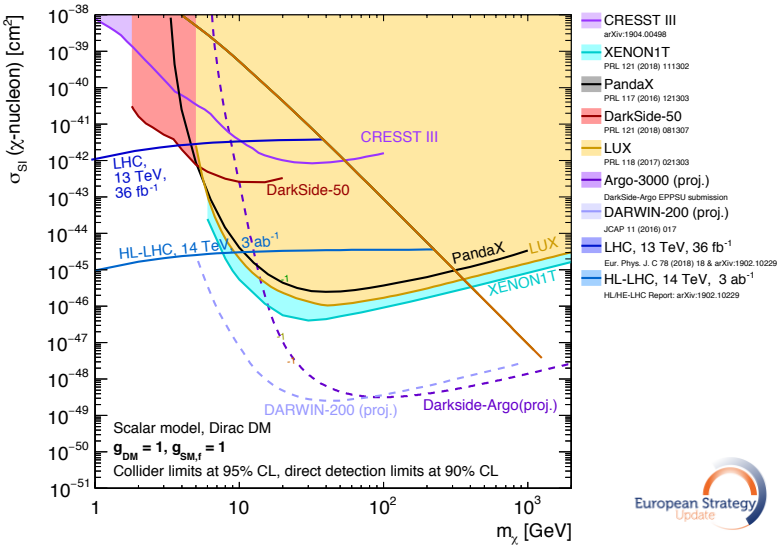

Figure 47. Summary of the projected limits on dark matter particles from HL-LHC. The expected limit and constraints from current and future direct detection experiments on a specific model for dark matter-nucleon scattering are shown. The areas above the curves are excluded. Based on Refs. [144, 145].

1 TeV [142, 143].

Finally, dark matter can be searched via its interactions with electroweak gauge bosons. Signatures include events containing only a single photon or Z boson, when the dark matter is produced in events via a process called vector boson fusion. For example, in mono-Z searches, masses up to a factor of 3 larger than current limits could be probed [142, 143].

Figure 47 illustrates the sensitivity of HL-LHC searches for dark matter by showing the sensitivity that can be obtained as a function of the dark matter particle mass and cross section for a specific model of dark matter. The HL-LHC has better sensitivity to particles with masses below 10 GeV, while the direct detection experiments have better sensitivity at higher masses. This demonstrates the complementarity of the two different search techniques [142, 143].

6. Organizing Science

Before moving to the conclusions, we provide a brief overview of CERN, the HL-LHC's hostlab, and a discussion of the organization of the large LHC collaborations.

6.1. CERN: Science for Peace and Society

CERN [146] was officially founded in 1954. The CERN convention was signed in 1953 by twelve founding countries, Belgium, Denmark, France, the Federal Republic of Germany, Greece, Italy, the Netherlands, Norway, Sweden, Switzerland, the United Kingdom, and Yugoslavia. Since then, CERN has grown continuously, and today has 23 member states. The latest addition to the CERN family was Serbia, joining

in 2019. In order to become a member state the countries must follow a three-step procedure, with growing rights and duties. Six countries are presently associate member states (first step), and three countries are in the pre-stage to membership (second stage). Six countries or entities have observer status (Japan, the Russian Federation, the United States of America, as well as the European Union, the Joint Institute for Nuclear Research, and UNESCO). Co-operation agreements are in place with a further 38 countries. CERN welcomes users from about 900 different institutions in more than 70 countries. At CERN, scientists from all over the world work together peacefully.

The highest authority or "Parliament" of CERN is the Council, which is formed by delegates from each of the 23 member states. Each member state has two delegates, one representing the scientific community and one representing the government. The Director General, assisted by four directors, manages the CERN laboratory and is appointed by the Council. The mandate of the Director General is 5 years and renewable once. Scientific and financial matters are dealt with in two dedicated committees, the Scientific Policy Committee and the Financial Committee. CERN is further subdivided into 10 departments, including scientific ones such as the Experimental Physics and Theoretical Physics Departments, as well as more administrative ones, such as Human Resources or Site Management and Buildings. Today, CERN has a staff of about 2500 persons, and a campus with hundreds of buildings with offices and laboratories, including three restaurants and several hostels. The total number of CERN users amounts to more than 12,000.

CERN is funded by its member states. The contribution of each country is proportional to its gross domestic product. This funding is used to operate the laboratory and to employ the CERN staff for the development, construction and operation of the accelerators, as well as to support the infrastructure of the experiments.

CERN's main mission is to enable world-class fundamental science by operating particle accelerators. CERN is not involved in military research. CERN works together with industry on the fore-front of technological developments, but is not funded by industry. The developments by CERN or scientific results that were achieved in the framework of CERN are openly shared with society, e.g. publications are openly accessible. Today, almost everybody is using an invention made at CERN: the World Wide Web was invented in 1989 at CERN, to aid scientific communication via the "internet". CERN contributes to the dissemination of knowledge about particle physics by offering free visits to the laboratory and the experiments. The "Open Days" in 2019 attracted 75,000 visitors.

CERN has an equal opportunity policy, and a code of conduct [147] was put in place in 2010.

6.2. The Biggest Experimental Collaborations Worldwide

The ATLAS [42] and CMS [43] Collaborations are the largest experimental science collaborations in the world, with more than 5000 members each.

The ATLAS and CMS Collaborations involve each more than 200 institutes, including CERN, from about 50 countries, mainly from Europe, Asia, and the Americas. The number of institutes, and even countries, is still growing for both collaborations. A total of about 3000 physicists, including more than 1000 doctoral students, are presently listed per experiment. Approximately, one quarter of the physicists are female. The collaborations each also include about 1000 engineers, and hundreds of undergraduate students and technicians. Most people work mainly in their home countries. Collaboration meetings are scheduled at CERN several times per year. In addition, remote access to meetings is possible from all over the world.

Each collaboration is managed by a spokesperson, together with his/her deputies and aided by a management team including, for example, a physics coordinator and an upgrade coordinator. The spokesperson is elected by a subset of the collaboration members for a 2-year term (renewable once for ATLAS), while the deputies are appointed by the spokesperson. The highest decision making body though is the Collaboration Board, in which the member institutes are represented. Further important bodies deal with the overall management and with financial matters. Both collaborations are subdivided into several projects, mainly representing the detector systems, with their own management structures and respective Institution Boards. A further subdivision into Working Groups is in place. Institutes or individuals are associated to a certain project. The experiment is funded by its member institutes. Each institute pays a certain amount per author signing the physics papers to support the general infrastructure and the operation of the experiment, plus an additional contribution for the projects it is subscribed to.

A prerequisite to become an author is the execution of a certain amount of service work. The collaborations have systems in place to engage the members in key duties such as detector operation and development or maintenance of central software and other tools. Every author must on average contribute about 4 months per year to such selected topics, and each institute must take over a certain number of detector shifts in the control room.

Both collaborations run a diversity office to foster a working environment where all members of the collaboration can thrive and bring in their talents, irrespective of age, career status, employment situation, institutional affiliation, geographical location, nationality, gender, ethnicity, family situation, sexual orientation, or disabilities.

Typically, institutes contribute both to data analysis and service work (operation, including computing infrastructure, and/or upgrade activities). The detector upgrades are common efforts and the construction work is shared between hundreds of people from many institutes. Also the physics analyses are typically shared efforts. Depending on the complexity of the analysis, the involvement can range from one institute, with a few persons, up to several institutes with in total of the order of 50 physicists. However, any publication involving collision data is signed by the whole collaboration, to value the fact that the scientific output would not

have been possible without the effort of the full collaboration. A rigorous quality control system is in place regarding the publications, including a specific review committee for each publication, as well as a step in which the draft is circulated in the whole collaboration and every member of the collaboration is invited to send comments. All publications are open access. The collaborations also publish subsets of their data and provide the tools needed to analyze them [148].

7. Conclusion

The world's highest energy accelerator, the LHC, has been exploring the fundamental building blocks of matter and their interactions through high-energy proton-proton and heavy-ion collisions since 2010. Its extensive physics results include discovering the final piece of the SM of particle physics: the Higgs boson. The HL-LHC, the focus of this article, is the upgrade to the LHC, and is currently under construction at CERN. The aim is for the HL-LHC to begin data-taking in 2027. The HL-LHC will be capable of achieving significantly higher instantaneous luminosity than the LHC to increase the total delivered luminosity by an order of magnitude over a period of 12 years and enable an extensive and exciting physics program.

We have provided an overview of the essential components of the LHC machine that are being upgraded to achieve the high luminosities needed for the HL-LHC. These include an upgrade to the LHC injector complex, the installation of new wide aperture inner triplet magnets, and novel crab cavities. We discussed the extensive upgrade programs planned for the ATLAS and CMS detectors to allow them to deliver high-quality physics results despite the large number of simultaneous interactions and the harsh radiation environment expected from the HL-LHC. Key features include complete replacements of the silicon tracking detectors, a new high-granularity endcap calorimeter for CMS, new timing detectors, and new readout and trigger electronics. The upgraded detectors are shown to be capable of achieving excellent performance in reconstructing physics objects. Finally, key elements of the physics program for HL-LHC were discussed, highlighting exciting opportunities in precision Higgs measurements, observation of the Higgs self-coupling, probes of electroweak symmetry breaking, and searches for physics beyond the SM.

Given that the timescales to design and construct such gigantic colliders are typically many decades, the field of particle physics is currently undergoing extensive discussions within the context of several regional and international planning processes to determine the collider or colliders to follow the HL-LHC. For the energy frontier, options currently considered include electron-positron colliders, also known as Higgs factories, proton-proton colliders, and even muon-muon colliders. A future proton-proton collider would be circular, but both circular and linear designs are under discussion for electron-positron machines. More mature project proposals include the Future Circular Collider (FCC) [149,150] and the Compact Linear Collier (CLIC) [151–153], which would be located at CERN, the Circular Electron-Positron Collider (CEPC) [154] and the Super Proton-Proton Collider (SppC) [154], which

would be located in China, and the International Linear Collider (ILC [155, 156]), which would be located in Japan. There are significant differences in the physics foci and capabilities between the different colliders. However, all proposed future colliders have exciting physics programs and realising any one of these future colliders would determine the direction of the field of particle physics for many decades.

Acknowledgements

Heather Gray was partially supported by the Office of Science, Office of High Energy Physics, of the U.S. Department of Energy, and partially supported by the Laboratory Directed Research and Development Program of Lawrence Berkeley National Laboratory under contract no. DE-AC02-05CH11231. Katja Klein was supported by the BMBF, Germany. Meenakshi Narain acknowledges the support of U.S. Department of Energy grant number DE-SC0010010. Richard Polifka was partly supported by two projects of the Ministry of Education, Youth and Sports of the Czech Republic: the research infrastructure CERN-CZ (project LM2018104) acting as gateway to CERN and its experiments as well as the Inter-Excellence/Inter-Transfer project LTT17018 supporting the physics analyses at CERN experiments.

[1] O. S. Bruening, P. Collier, P. Lebrun, S. Myers, R. Ostojic, J. Poole, and P. Proudlock, "LHC Design Report", Technical Report CERN-2004-003-V-1, CERN Yellow Reports: Monographs, Geneva, 2004. doi:10.5170/CERN-2004-003-V-1.

[2] ATLAS Collaboration, "The ATLAS Experiment at the CERN Large Hadron Collider", 2008 *JINST* **3** S08003, doi:10.1088/1748-0221/3/08/S08003.

[3] CMS Collaboration, "The CMS experiment at the CERN LHC", 2008 *JINST* **3** S08004, doi:10.1088/1748-0221/3/08/S08004.

[4] LHCb Collaboration, "The LHCb Detector at the LHC", 2008 *JINST* **3** S08005, doi:10.1088/1748-0221/3/08/s08005.

[5] ALICE Collaboration, "The ALICE experiment at the CERN LHC", 2008 *JINST* **3** S08002, doi:10.1088/1748-0221/3/08/s08002.

[6] S. Glashow, "Partial Symmetries of Weak Interactions", *Nucl. Phys.* **22** (1961) 579–588, doi:10.1016/0029-5582(61)90469-2.

[7] S. Weinberg, "A Model of Leptons", *Phys. Rev. Lett.* **19** (1967) 1264–1266, doi:10.1103/PhysRevLett.19.1264.

[8] A. Salam, "Weak and Electromagnetic Interactions", *Conf. Proc. C* **680519** (1968) 367–377, doi:10.1142/9789812795915_0034.

[9] S. Glashow et al., "Weak Interactions with Lepton-Hadron Symmetry", *Phys. Rev. D* **2** (1970) 1285–1292, doi:10.1103/PhysRevD.2.1285.

[10] H. Fritzsch et al., "Advantages of the Color Octet Gluon Picture", *Phys. Lett. B* **47** (1973) 365–368, doi:10.1016/0370-2693(73)90625-4.

[11] D. Gross and F. Wilczek, "Asymptotically Free Gauge Theories - I", *Phys. Rev. D* **8** (1973) 3633–3652, doi:10.1103/PhysRevD.8.3633.

[12] H. Politzer, "Reliable Perturbative Results for Strong Interactions?", *Phys. Rev. Lett.* **30** (1973) 1346–1349, doi:10.1103/PhysRevLett.30.1346.

[13] D. Gross and F. Wilczek, "Asymptotically Free Gauge Theories - II", *Phys. Rev. D* **9** (1974) 980–993, doi:10.1103/PhysRevD.9.980.

[14] F. Englert and R. Brout, "Broken Symmetry and the Mass of Gauge Vector Mesons", *Phys. Rev. Lett.* **13** (1964) 321–323, doi:10.1103/PhysRevLett.13.321.

[15] P. W. Higgs, "Broken symmetries, massless particles and gauge fields", *Phys. Lett.* **12** (1964) 132–133, doi:10.1016/0031-9163(64)91136-9.

[16] P. W. Higgs, "Broken Symmetries and the Masses of Gauge Bosons", *Phys. Rev. Lett.* **13** (1964) 508–509, doi:10.1103/PhysRevLett.13.508.

[17] G. S. Guralnik et al., "Global Conservation Laws and Massless Particles", *Phys. Rev. Lett.* **13** (1964) 585–587, doi:10.1103/PhysRevLett.13.585.

[18] UA1 Collaboration, "Experimental observation of lepton pairs of invariant mass around 95 GeV/c^2 at the CERN SPS Collider", *Phys. Lett. B* **126** (1983) 398–410, doi:10.1016/0370-2693(83)90188-0.

[19] UA1 Collaboration, "Experimental observation of isolated large transverse energy electrons with associated missing energy at $\sqrt{s} = 540$ GeV", *Phys. Lett. B* **122** (1983) 103–116, doi:10.1016/0370-2693(83)91177-2.

[20] UA2 Collaboration, "Evidence for $Z^0 \to e^+e^-$ at the CERN pp collider", *Phys. Lett. B* **129** (1983) 130–140, doi:https://doi.org/10.1016/0370-2693(83)90744-X.

[21] UA2 Collaboration, "Observation of single isolated electrons of high transverse momentum in events with missing transverse energy at the CERN pp collider", *Phys. Lett. B* **122** (1983) 476–485, doi:https://doi.org/10.1016/0370-2693(83)91605-2.

[22] CDF Collaboration, "Observation of Top Quark Production in $\bar{p}p$ Collisions with the Collider Detector at Fermilab", *Phys. Rev. Lett.* **74** (1995) 2626–2631, doi:10.1103/physrevlett.74.2626.

[23] D0 Collaboration, "Observation of the Top Quark", *Phys. Rev. Lett.* **74** (1995) 2632–2637, doi:10.1103/physrevlett.74.2632.

[24] DONUT Collaboration, "Observation of tau neutrino interactions", *Phys. Lett. B* **504** (2001) 218–224, doi:10.1016/s0370-2693(01)00307-0.

[25] ATLAS Collaboration, "Observation of a new particle in the search for the Standard Model Higgs boson with the ATLAS detector at the LHC", *Phys. Lett. B* **716** (2012) 1–29, doi:10.1016/j.physletb.2012.08.020, arXiv:1207.7214.

[26] CMS Collaboration, "Observation of a new boson at a mass of 125 GeV with the CMS experiment at the LHC", *Phys. Lett. B* **716** (2012) 30–61, doi:10.1016/j.physletb.2012.08.021, arXiv:1207.7235.

[27] F. Zwicky, "Die Rotverschiebung von extragalaktischen Nebeln", *Helv. Phys. Acta* **6** (1933) 110–127, doi:10.1007/s10714-008-0707-4. [Gen. Rel. Grav.41,207(2009)].

[28] G. Bertone, D. Hooper, and J. Silk, "Particle dark matter: Evidence, candidates and constraints", *Phys. Rept.* **405** (2005) 279–390, doi:10.1016/j.physrep.2004.08.031, arXiv:hep-ph/0404175.

[29] CERN, 2020. https://project-hl-lhc-industry.web.cern.ch/content/project-schedule.

[30] ALICE Collaboration, "Upgrade of the ALICE Experiment: Letter of Intent", Technical Report CERN-LHCC-2012-012, 2012. doi:10.1088/0954-3899/41/8/087001.

[31] LHCb Collaboration, "Expression of Interest for a Phase-II LHCb Upgrade: Opportunities in flavour physics, and beyond, in the HL-LHC era", Technical Report CERN-LHCC-2017-003, 2017.

[32] "LEP design report", technical report, Geneva, 1984. Copies shelved as reports in LEP, PS and SPS libraries.

[33] J.-L. Caron, "LHC layout. Schema general du LHC", (Sep, 1997). AC Collection. Legacy of AC. Pictures from 1992 to 2002.

[34] P. Schmueser, "Superconducting magnets for particle accelerators", *Rept. Prog. Phys.* **54** (1991) 683–730, doi:10.1088/0034-4885/54/5/001.

[35] A. Mereghetti, R. Bruce, N. Fuster-Martínez, D. Mirarchi, and S. Redaelli, "Collimation System Upgrades for the High Luminosity Large Hadron Collider and Expected Cleaning Performance in Run 3", in *Proceedings of the 10th International Particle Accelerator Conference (IPAC'19), Melbourne, Australia, 19-24 May 2019*, pp. 681–684, JACoW Publishing (2019). doi:10.18429/JACoW-IPAC2019-MOPRB051.

[36] L. Medina, R. Tomás, G. Arduini, and M. Napsuciale, "Assessment of the performance of High-Luminosity LHC operational scenarios: integrated luminosity and effective pile-up density", *Canadian Journal of Physics* **97** (2019), no. 5, 498–508,

doi:10.1139/cjp-2018-0291.

[37] M. Meddahi et al., "LHC Injectors Upgrade project: Towards new territory beam parameters", in *Proceedings of the 10th International Particle Accelerator Conference (IPAC'19), Melbourne, Australia, 19-24 May 2019*, pp. 3385–3390, JACoW Publishing (2019). doi:10.18429/JACoW-IPAC2019-THXPLM1.

[38] S. Fartoukh, R. Bruce, F. Carlier, J. Coello de Portugal, A. Garcia-Tabares, E. Maclean, L. Malina, A. Mereghetti, D. Mirarchi, T. Persson, M. Pojer, L. Ponce, S. Redaelli, B. Salvachua, P. Sk, M. Solfaroli, R. Tomas, D. Valuch, A. Wegscheider, and J. Wenninger, "Experimental validation of the Achromatic Telescopic Squeezing (ATS) scheme at the LHC", *Journal of Physics: Conference Series* **874** (2017) 012010, doi:10.1088/1742-6596/874/1/012010.

[39] R. Calaga, "Crab Cavities for the High-luminosity LHC", in *Proceedings of the 18th International Conference on RF Superconductivity, Lanzhou, China, 17-21 July 2017*, pp. 695–699, JACoW Publishing (2018). doi:10.18429/JACoW-SRF2017-THXA03.

[40] A. Ballarino, "Development of superconducting links for the Large Hadron Collider machine", *Superconductor Science and Technology* **27** (2014) 044024, doi:10.1088/0953-2048/27/4/044024.

[41] G. Apollinari, I. Béjar Alonso, O. Brüning, P. Fessia, M. Lamont, L. Rossi, and L. Tavian, "High-Luminosity Large Hadron Collider (HL-LHC): Technical Design Report V. 0.1", Technical Report CERN Yellow Reports: Monographs, Geneva, 2017. doi:10.23731/CYRM-2017-004.

[42] ATLAS Collaboration. https://atlas.cern/.

[43] CMS Collaboration. https://cms.cern/.

[44] ATLAS Collaboration, "ATLAS: Letter of intent for a general purpose p p experiment at the large hadron collider at CERN", Technical Report CERN-LHCC-92-04, CERN-LHCC-I-2, 1992.

[45] CMS Collaboration, "CMS: The Compact Muon Solenoid: Letter of intent for a general purpose detector at the LHC", Technical Report CERN-LHCC-92-03, CERN-LHCC-I-1, 1992.

[46] ATLAS Collaboration, "ATLAS Insertable B-Layer Technical Design Report", Technical Report CERN-LHCC-2010-013, ATLAS-TDR-19, 2010.

[47] CMS Collaboration, "CMS Technical Design Report for the Pixel Detector Upgrade", CMS Technical Design Report CERN-LHCC-2012-016, CMS-TDR-11, 2012.

[48] CMS Collaboration, "CMS Technical Design Report for the Phase 1 Upgrade of the Hadron Calorimeter", Technical Report CERN-LHCC-2012-015, CMS-TDR-10, 2012.

[49] ATLAS Collaboration, "New Small Wheel Technical Design Report", Technical Report CERN-LHCC-2013-006, ATLAS-TDR-020, 2013.

[50] ATLAS Collaboration, "Interactive web pages for radiation environment exploration of ATLAS", Technical Report ATL-SOFT-PUB-2020-003, 2020.

[51] GEANT4 Collaboration, "Geant4—a simulation toolkit", *Nucl. Instrum. Meth. A* **506** (2003) 250–303, doi:https://doi.org/10.1016/S0168-9002(03)01368-8.

[52] CMS Collaboration, "The Phase-2 Upgrade of the CMS L1 Trigger Interim Technical Design Report", Technical Report CERN-LHCC-2017-013, CMS-TDR-017, 2017.

[53] CMS Collaboration, "The Phase-2 Upgrade of the CMS DAQ Interim Technical Design Report", Technical Report CERN-LHCC-2017-014, CMS-TDR-018, 2017.

[54] ATLAS Collaboration, "Technical Design Report for the Phase-II Upgrade of the ATLAS TDAQ System", Technical Report CERN-LHCC-2017-020, ATLAS-TDR-029, 2017.

[55] CMS Collaboration, "The Phase-2 Upgrade of the CMS Tracker", Technical Report CERN-LHCC-2017-009, CMS-TDR-014, 2017.

[56] ATLAS Collaboration, "Technical Design Report for the ATLAS Inner Tracker Strip Detector", Technical Report CERN-LHCC-2017-005, ATLAS-TDR-025, 2017.

[57] ATLAS Collaboration, "Technical Design Report for the ATLAS Inner Tracker Pixel Detector", Technical Report CERN-LHCC-2017-021, ATLAS-TDR-030, 2017.

[58] CMS Collaboration, "The Phase-2 Upgrade of the CMS Barrel Calorimeters", Technical

Report CERN-LHCC-2017-011, CMS-TDR-015, 2017.
[59] CMS Collaboration, "The Phase-2 Upgrade of the CMS Endcap Calorimeter", Technical Report CERN-LHCC-2017-023, CMS-TDR-019, 2017.
[60] ATLAS Collaboration, "ATLAS Calorimeter Performance: Technical Design Report", Technical Report CERN-LHCC-96-040, ATLAS-TDR-1, 1996.
[61] ATLAS Collaboration, "Technical Design Report for the Phase-II Upgrade of the ATLAS Tile Calorimeter", Technical Report CERN-LHCC-2017-019, ATLAS-TDR-028, 2017.
[62] CMS Collaboration, "The Phase-2 Upgrade of the CMS Muon Detectors", Technical Report CERN-LHCC-2017-012, CMS-TDR-016, 2017.
[63] CMS Collaboration, "CMS Technical Design Report for the Muon Endcap GEM Upgrade", Technical Report CERN-LHCC-2015-012, CMS-TDR-013, 2015.
[64] ATLAS Collaboration, "Technical Design Report for the Phase-II Upgrade of the ATLAS Muon Spectrometer", Technical Report CERN-LHCC-2017-017, ATLAS-TDR-026, 2017.
[65] CMS Collaboration, "A MIP Timing Detector for the CMS Phase-2 Upgrade", Technical Report CERN-LHCC-2019-003, CMS-TDR-020, 2019.
[66] ATLAS Collaboration, "Technical Design Report: A High-Granularity Timing Detector for the ATLAS Phase-II Upgrade", Technical Report CERN-LHCC-2020-007, ATLAS-TDR-031, 2020.
[67] H. Spieler, "Semiconductor Detector Systems", Oxford University Press, ISBN 978-0-19-852784-8.
[68] ATLAS Collaboration, Event Displays from Upgrade Physics Simulated Data - Public Results, 2020. https://twiki.cern.ch/twiki/bin/view/AtlasPublic/UpgradeEventDisplays.
[69] F. Antinori et al., "Experience with a 30 cm^2 silicon pixel plane in CERN experiment WA97", *Nucl. Instrum. Meth. A* **360** (1995) 91–97, doi:10.1016/0168-9002(94)01224-5.
[70] K. H. Becks et al., "The DELPHI pixels", *Nucl. Instrum. Meth. A* **386** (1997) 11–17, doi:10.1016/S0168-9002(96)01089-3.
[71] ATLAS Collaboration, "Expected Tracking Performance of the ATLAS Inner Tracker at the HL-LHC", Technical Report ATL-PHYS-PUB-2019-014, 2019.
[72] RD53 Collaboration. https://rd53.web.cern.ch/rd53/.
[73] RD53 Collaboration, "RD53B Manual", Technical Report CERN-RD53-PUB-19-002, 2019.
[74] Tracker group of the CMS Collaboration, "Beam test performance of prototype silicon detectors for the Outer Tracker for the Phase-2 Upgrade of CMS", 2020 *JINST* **15** P03014, doi:10.1088/1748-0221/15/03/p03014.
[75] CALICE Collaboration, "Design and Electronics Commissioning of the Physics Prototype of a Si-W Electromagnetic Calorimeter for the International Linear Collider", *JINST* **3** (2008) P08001, doi:10.1088/1748-0221/3/08/P08001, arXiv:0805.4833.
[76] ATLAS Collaboration, "Technical Proposal: A High-Granularity Timing Detector for the ATLAS Phase-II Upgrade", Technical Report CERN-LHCC-2018-023, LHCC-P-012, 2018.
[77] G. Pellegrini, P. Fernández-Martínez, M. Baselga, C. Fleta, D. Flores, V. Greco, S. Hidalgo, I. Mandić, G. Kramberger, D. Quirion, and M. Ullan, "Technology developments and first measurements of Low Gain Avalanche Detectors (LGAD) for high energy physics applications", *Nucl. Instrum. Meth. A* **765** (2014) 12–16, doi:https://doi.org/10.1016/j.nima.2014.06.008.
[78] A. Benaglia, S. Gundacker, P. Lecoq, M. Lucchini, A. Para, K. Pauwels, and E. Auffray, "Detection of high energy muons with sub-20 ps timing resolution using L(Y)SO crystals and SiPM readout", *Nucl. Instrum. Meth. A* **830** (2016) 30–35, doi:https://doi.org/10.1016/j.nima.2016.05.030.
[79] CMS Collaboration, "The MIP Timing Detector", Technical Report CMS-DP-2019-037, 2019.
[80] CERN Computing Centre. https://home.cern/science/computing.
[81] K. Bos et al., "LHC computing Grid. Technical Design Report.", Technical Report

CERN-LHCC-2005-024, LCG-TDR-001, 2005.
[82] ATLAS Collaboration, "Expected performance of the ATLAS detector at the High-Luminosity LHC", Technical Report ATL-PHYS-PUB-2019-005, 2019.
[83] CMS Collaboration, "Expected performance of the physics objects with the upgraded CMS detector at the HL-LHC", Technical Report CMS-NOTE-2018-006, 2018.
[84] D. Bertolini, P. Harris, M. Low, and N. Tran, "Pileup per particle identification", *JHEP* **10** (2014) 059, doi:10.1007/jhep10(2014)059.
[85] CMS Collaboration, "Pileup mitigation at CMS in 13 TeV data", Technical Report CMS-PAS-JME-18-001, 2019.
[86] HEPiX Benchmarking Group. http://w3.hepix.org/benchmarking.html.
[87] P. Calafiura, J. Catmore, D. Costanzo, and A. Di Girolamo, "ATLAS HL-LHC Computing Conceptual Design Report", Technical Report CERN-LHCC-2020-015, LHCC-G-178, 2020.
[88] HEP Software Foundation Collaboration, "HL-LHC Computing Review: Common Tools and Community Software", doi:10.5281/zenodo.4009114, arXiv:2008.13636.
[89] CMS Offline Software and Computing, "Evolution of the CMS Computing Model towards Phase-2", Technical Report CMS-NOTE-2021-001, 2021.
[90] ATLAS Collaboration, Computing and Software - Public Results, 2020. https://twiki.cern.ch/twiki/bin/view/AtlasPublic/ComputingandSoftwarePublicResults.
[91] G. E. Moore, "Cramming More Components onto Integrated Circuits", *Electronics 38* **8** (1965) 114–117, doi:10.1109/JPROC.1998.658762.
[92] J. L. Hennessy and D. A. Patterson, "A New Golden Age for Computer Architecture", *Commun. ACM* **62** (2019) 48–60, doi:10.1145/3282307.
[93] Elementary particles of the Standard Model. Image source:. https://en.wikipedia.org/wiki/Standard_Model.
[94] E. Witten, "Dynamical Breaking of Supersymmetry", *Nucl. Phys. B* **188** (1981) 513, doi:10.1016/0550-3213(81)90006-7.
[95] S. Dimopoulos and H. Georgi, "Softly Broken Supersymmetry and SU(5)", *Nucl. Phys. B* **193** (1981) 150–162, doi:10.1016/0550-3213(81)90522-8.
[96] N. Sakai, "Naturalness in Supersymmetric GUTS", *Z. Phys. C* **11** (1981) 153, doi:10.1007/BF01573998.
[97] L. Susskind, "The Gauge Hierarchy Problem, Technicolor, Supersymmetry, and all that.", *Phys. Rept.* **104** (1984) 181–193, doi:10.1016/0370-1573(84)90208-4.
[98] Y. A. Golfand and E. P. Likhtman, "Extension of the Algebra of Poincare Group Generators and Violation of p Invariance", *JETP Lett.* **13** (1971) 323–326.
[99] D. Volkov and V. Akulov, "Is the Neutrino a Goldstone Particle?", *Phys. Lett. B* **46** (1973) 109–110, doi:10.1016/0370-2693(73)90490-5.
[100] J. Wess and B. Zumino, "Supergauge Transformations in Four-Dimensions", *Nucl. Phys. B* **70** (1974) 39–50, doi:10.1016/0550-3213(74)90355-1.
[101] J. Wess and B. Zumino, "Supergauge Invariant Extension of Quantum Electrodynamics", *Nucl. Phys. B* **78** (1974) 1, doi:10.1016/0550-3213(74)90112-6.
[102] P. Fayet, "Supersymmetry and Weak, Electromagnetic and Strong Interactions", *Phys. Lett.* **B64** (1976) 159, doi:10.1016/0370-2693(76)90319-1.
[103] P. Fayet, "Spontaneously Broken Supersymmetric Theories of Weak, Electromagnetic and Strong Interactions", *Phys. Lett.* **B69** (1977) 489, doi:10.1016/0370-2693(77)90852-8.
[104] K. Agashe, R. Contino, and A. Pomarol, "The Minimal composite Higgs model", *Nucl. Phys. B* **719** (2005) 165–187, doi:10.1016/j.nuclphysb.2005.04.035, arXiv:hep-ph/0412089.
[105] D. B. Kaplan, H. Georgi, and S. Dimopoulos, "Composite Higgs Scalars", *Phys. Lett. B* **136** (1984) 187–190, doi:10.1016/0370-2693(84)91178-X.
[106] M. Schmaltz and D. Tucker-Smith, "Little Higgs review", *Ann. Rev. Nucl. Part. Sci.* **55** (2005) 229–270, doi:10.1146/annurev.nucl.55.090704.151502, arXiv:hep-ph/0502182.

[107] N. Arkani-Hamed, A. Cohen, E. Katz, and A. Nelson, "The Littlest Higgs", *JHEP* **07** (2002) 034, doi:10.1088/1126-6708/2002/07/034, arXiv:hep-ph/0206021.

[108] C. T. Hill and E. H. Simmons, "Strong Dynamics and Electroweak Symmetry Breaking", *Phys. Rept.* **381** (2003) 235–402, doi:10.1016/S0370-1573(03)00140-6, arXiv:hep-ph/0203079. [Erratum: Phys.Rept. 390, 553–554 (2004)].

[109] D. B. Kaplan and H. Georgi, "SU(2) x U(1) Breaking by Vacuum Misalignment", *Phys. Lett. B* **136** (1984) 183–186, doi:10.1016/0370-2693(84)91177-8.

[110] M. J. Dugan et al., "Anatomy of a Composite Higgs Model", *Nucl. Phys. B* **254** (1985) 299–326, doi:10.1016/0550-3213(85)90221-4.

[111] R. Contino, "The Higgs as a Composite Nambu-Goldstone Boson", Theoretical Advanced Study Institute in Elementary Particle Physics: Physics of the Large and the Small, 235–306, 2011. doi:10.1142/9789814327183_0005.

[112] G. Panico and A. Wulzer, "The Composite Nambu-Goldstone Higgs", Lecture Notes in Physics book series (LNP, volume 913), Springer, 2016. doi:10.1007/978-3-319-22617-0.

[113] C. Csáki and P. Tanedo, "Beyond the Standard Model", in *Proceedings of the 2013 European School of High-Energy Physics, Paradfurdo, Hungary, 5-18 June 2013*, pp. 169–268, CERN–2015–004 (2015). arXiv:1602.04228. doi:10.5170/CERN-2015-004.169.

[114] LHC Higgs Cross Section Working Group, "Handbook of LHC Higgs Cross Sections: 4. Deciphering the Nature of the Higgs Sector", Technical Report CERN-2017-002-M, CERN Yellow Reports: Monographs, Geneva, 2016. doi:10.23731/CYRM-2017-002.

[115] HL/HE Working Group 2, "Higgs Physics at the HL-LHC and HE-LHC", Technical Report CERN-LPCC-2018-04, 2019. arXiv:1902.00134.

[116] CMS Collaboration, "Combined Higgs boson production and decay measurements with up to 137 fb^{-1} of proton-proton collision data at $\sqrt{s} = 13$ TeV", Technical Report CMS-PAS-HIG-19-005, 2020.

[117] ATLAS Collaboration, "Combined measurements of Higgs boson production and decay using up to 80 fb^{-1} of proton-proton collision data at $\sqrt{s} = 13$ TeV collected with the ATLAS experiment", *Phys. Rev. D* **101** (2020) 012002, doi:10.1103/PhysRevD.101.012002, arXiv:1909.02845.

[118] CMS Collaboration, "Prospects for HH measurements at the HL-LHC", Technical Report CMS-PAS-FTR-18-019, 2018.

[119] ATLAS Collaboration, "Combination of searches for Higgs boson pairs in pp collisions at $\sqrt{s} = 13$ TeV with the ATLAS detector", *Phys. Lett. B* **800** (2020) 135103, doi:https://doi.org/10.1016/j.physletb.2019.135103.

[120] B. W. Lee, C. Quigg, and H. B. Thacker, "Strength of Weak Interactions at Very High Energies and the Higgs Boson Mass", *Phys. Rev. Lett.* **38** (1977) 883–885, doi:10.1103/PhysRevLett.38.883.

[121] ATLAS Collaboration, "Prospects for the measurement of the $W^{\pm}W^{\pm}$ scattering cross section and extraction of the longitudinal scattering component in pp collisions at the High-Luminosity LHC with the ATLAS experiment", Technical Report ATL-PHYS-PUB-2018-052, 2018.

[122] CMS Collaboration, "Measurements of production cross sections of polarized same-sign W boson pairs in association with two jets in proton-proton collisions at $\sqrt{s} = 13$ TeV", *Phys. Lett. B* **812** (2021) 136018, doi:10.1016/j.physletb.2020.136018, arXiv:2009.09429.

[123] J. Chang, K. Cheung, C.-T. Lu, and T.-C. Yuan, "WW scattering in the era of post-Higgs-boson discovery", *Phys. Rev. D* **87** (2013) 093005, doi:10.1103/physrevd.87.093005.

[124] N. Arkani-Hamed, S. Dimopoulos, and G. Dvali, "The hierarchy problem and new dimensions at a millimeter", *Phys. Lett. B* **429** (1998) 263, doi:10.1016/S0370-2693(98)00466-3, arXiv:hep-ph/9803315.

[125] L. Randall and R. Sundrum, "A large mass hierarchy from a small extra dimension", *Phys.*

Rev. Lett. **83** (1999) 3370, doi:10.1103/PhysRevLett.83.3370, arXiv:hep-ph/9905221.

[126] CMS Collaboration, "Searches for light higgsino-like charginos and neutralinos at the HL-LHC with the Phase-2 CMS detector", Technical Report CMS-PAS-FTR-18-001, 2018.

[127] CMS Collaboration, "Search for direct pair production of supersymmetric partners to the τ lepton in proton–proton collisions at $\sqrt{s} = 13\,\text{TeV}$", *Eur. Phys. J. C* **80** (2020) 189, doi:10.1140/epjc/s10052-020-7739-7.

[128] CMS Collaboration, "Search for supersymmetry with direct stau production at the HL-LHC with the CMS Phase-2 detector", Technical Report CMS-PAS-FTR-18-010, 2019.

[129] D. Curtin et al., "Long-Lived Particles at the Energy Frontier: The MATHUSLA Physics Case", *Rep. Prog. Phys.* **82** (2019) 116201, doi:10.1088/1361-6633/ab28d6, arXiv:1806.07396.

[130] G. F. Giudice, M. A. Luty, H. Murayama, and R. Rattazzi, "Gaugino mass without singlets", *JHEP* **12** (1998) 027, doi:10.1088/1126-6708/1998/12/027, arXiv:hep-ph/9810442.

[131] L. Randall and R. Sundrum, "Out of this world supersymmetry breaking", *Nucl. Phys. B* **557** (1999) 79–118, doi:10.1016/S0550-3213(99)00359-4, arXiv:hep-th/9810155.

[132] M. Ibe, S. Matsumoto, and T. T. Yanagida, "Pure gravity mediation with $m_{3/2} = 10$–$100\,\text{TeV}$", *Phys. Rev. D* **85** (2012) 095011, doi:10.1103/physrevd.85.095011.

[133] ATLAS Collaboration, "ATLAS sensitivity to winos and higgsinos with a highly compressed mass spectrum at the HL-LHC", Technical Report ATL-PHYS-PUB-2018-031, 2018.

[134] HL/HE Working Group 3, "Beyond the Standard Model Physics at the HL-LHC and HE-LHC", Technical Report CERN-LPCC-2018-05, 2018. arXiv:1812.07831.

[135] A. Falkowski, J. T. Ruderman, T. Volansky, and J. Zupan, "Hidden Higgs Decaying to Lepton Jets", *JHEP* **05** (2010) 077, doi:10.1007/JHEP05(2010)077, arXiv:1002.2952.

[136] CMS Collaboration, "Search sensitivity for dark photons decaying to displaced muons with CMS at the high-luminosity LHC", Technical Report CMS-PAS-FTR-18-002, 2018.

[137] CMS Collaboration, "A Search for Beyond Standard Model Light Bosons Decaying into Muon Pairs", Technical Report CMS-PAS-HIG-16-035, 2016.

[138] G. Steigman and M. S. Turner, "Cosmological Constraints on the Properties of Weakly Interacting Massive Particles", *Nucl. Phys.* **B253** (1985) 375–386, doi:10.1016/0550-3213(85)90537-1.

[139] M. J. Strassler and K. M. Zurek, "Echoes of a hidden valley at hadron colliders", *Phys. Lett. B* **651** (2007) 374–379, doi:10.1016/j.physletb.2007.06.055, arXiv:hep-ph/0604261.

[140] S. Weinberg, "A New Light Boson?", *Phys. Rev. Lett.* **40** (1978) 223–226, doi:10.1103/PhysRevLett.40.223.

[141] R. D. Peccei and H. R. Quinn, "Constraints imposed by CP conservation in the presence of pseudoparticles", *Phys. Rev. D* **16** (1977) 1791–1797, doi:10.1103/PhysRevD.16.1791.

[142] A. Dainese, M. Mangano, A. B. Meyer, A. Nisati, G. Salam, and M. A. Vesterinen, eds., "Report on the Physics at the HL-LHC, and Perspectives for the HE-LHC", volume 7/2019 of *CERN Yellow Reports: Monographs*. CERN, Geneva, Switzerland, 2019. doi:10.23731/CYRM-2019-007, ISBN 978-92-9083-549-3.

[143] ATLAS and CMS Collaborations, "Report on the Physics at the HL-LHC and Perspectives for the HE-LHC", Technical Report CERN-LPCC-2019-01, 2019.

[144] D. Abercrombie et al., "Dark Matter Benchmark Models for Early LHC Run-2 Searches: Report of the ATLAS/CMS Dark Matter Forum", *Phys. Dark Univ.* **26** (2019) 100371, doi:10.1016/j.dark.2019.100371, arXiv:1507.00966.

[145] G. Busoni et al., "Recommendations on presenting LHC searches for missing transverse energy signals using simplified s-channel models of dark matter", *Phys. Dark Univ.* **27** (2019) 100365, doi:10.1016/j.dark.2019.100365, arXiv:1603.04156.

[146] CERN. https://home.cern/.
[147] CERN, "Code of Conduct". https://hr-dep.web.cern.ch/content/code-of-conduct.
[148] CERN Open Data Portal. http://opendata.cern.ch/.
[149] FCC Collaboration, "FCC-ee: The Lepton Collider - Future Circular Collider Conceptual Design Report Volume 2", *Eur. Phys. J. Special Topics* **228** (2019) 261–623, doi:10.1140/epjst/e2019-900045-4.
[150] FCC Collaboration, "FCC-hh: The Hadron Collider - Future Circular Collider Conceptual Design Report Volume 3", *Eur. Phys. J. Special Topics* **228** (2019) 755–1107, doi:10.1140/epjst/e2019-900087-0.
[151] P. Lebrun et al., "The CLIC Programme: Towards a Staged e^+e^- Linear Collider Exploring the Terascale: CLIC Conceptual Design Report", Technical Report CERN-2012-005, ANL-HEP-TR-12-51, KEK-REPORT-2012-2, MPP-2012-115, 2012. doi:10.5170/CERN-2012-005, arXiv:1209.2543.
[152] M. Aicheler et al., "A Multi-TeV Linear Collider Based on CLIC Technology: CLIC Conceptual Design Report", Technical Report CERN-2012-007, SLAC-R-985, KEK-Report-2012-1, PSI-12-01, JAI-2012-001, 2012. doi:10.5170/CERN-2012-007.
[153] The CLIC and CLICdp collaborations, "Updated baseline for a staged Compact Linear Collider", Technical Report CERN-2016-004, 2016. doi:10.5170/CERN-2016-004, arXiv:1608.07537.
[154] CEPC Study Group, "CEPC Conceptual Design Report: Volume 1 - Accelerator", Technical Report IHEP-CEPC-DR-2018-01, IHEP-AC-2018-01, 2018. arXiv:1809.00285.
[155] T. Behnke et al., "The International Linear Collider Technical Design Report - Volume 1: Executive Summary", Technical Report ILC-REPORT-2013-040, 2013. arXiv:1306.6327.
[156] C. Adolphsen et al., "The International Linear Collider Technical Design Report - Volume 3.II: Accelerator Baseline Design", Technical Report ILC-REPORT-2013-040, 2013. arXiv:1306.6328.